CAPITAL UNIVERSITY OF SCIENCE AND TECHNOLOGY, ISLAMABAD


# Design and Analysis of Biomimetic Lumbar Vertebral Body of Human Spine

by

Muhammad Usman Shahid

A thesis submitted in partial fulfillment for the degree of Master of Science

in the

Faculty of Engineering
Department of Mechanical Engineering

2025

*I dedicate this thesis to my beloved family, especially my parents, whose unwavering love, prayers, and support have been the foundation of all my achievements. This work is a reflection of their sacrifices and endless encouragement.*


# CERTIFICATE OF APPROVAL

## Design and Analysis of Biomimetic Lumbar Vertebral Body of Human Spine

by

Muhammad Usman Shahid

(MME233005)

### THESIS EXAMINING COMMITTEE

| S. No. | Examiner | Name | Organization |
|---|---|---|---|
| (a) | External Examiner | Dr. Muhammad Anwar | IST, Islamabad |
| (b) | Internal Examiner | Dr. Muhammad Irfan | CUST, Islamabad |
| (c) | Supervisor | Dr. Shummaila Rasheed | CUST, Islamabad |

Dr. Shummaila Rasheed
Thesis Supervisor
September, 2025

Dr. M. Mahabat Khan
Head
Dept. of Mechanical Engineering
September, 2025

Dr. Imtiaz Ahmad Taj
Dean
Faculty of Engineering
September, 2025

# *Author's Declaration*

I, **Muhammad Usman Shahid** hereby state that my MS thesis titled "**Design and Analysis of Biomimetic Lumbar Vertebral Body of Human Spine**" is my own work and has not been submitted previously by me for taking any degree from Capital University of Science and Technology, Islamabad or anywhere else in the country/abroad.

At any time if my statement is found to be incorrect even after my graduation, the University has the right to withdraw my MS Degree.

**(Muhammad Usman Shahid)**

Registration No: MME233005

# *Plagiarism Undertaking*

I solemnly declare that research work presented in this thesis titled "**Design and Analysis of Biomimetic Lumbar Vertebral Body of Human Spine**" is solely my research work with no significant contribution from any other person. Small contribution/help wherever taken has been duly acknowledged and that complete thesis has been written by me.

I understand the zero tolerance policy of the HEC and Capital University of Science and Technology towards plagiarism. Therefore, I as an author of the above titled thesis declare that no portion of my thesis has been plagiarized and any material used as reference is properly referred/cited.

I undertake that if I am found guilty of any formal plagiarism in the above titled thesis even after award of MS Degree, the University reserves the right to withdraw/revoke my MS degree and that HEC and the University have the right to publish my name on the HEC/University website on which names of students are placed who submitted plagiarized work.

**(Muhammad Usman Shahid)**

Registration No: MME233005

# *Acknowledgement*

All praise and gratitude are for **Allah Almighty**, whose countless blessings, mercy, and guidance gave me the strength, patience, and courage to complete this thesis. Without His will, nothing is possible. I also send heartfelt salutations and peace upon the beloved **Prophet Muhammad (PBUH)**, whose life and teachings are a source of light and inspiration for me.

I owe my deepest gratitude to my **family**, whose prayers, love, and encouragement have always been my greatest strength. In particular, I want to thank my uncle (**Abid Bashir**) and my brother (**Muhammad Noman Shahid**) for their unwavering support, constant motivation, and belief in me throughout this journey. Their care and sacrifices have truly been a foundation for my success.

I am profoundly thankful to my respected supervisor, **Dr. Shummaila Rasheed**, for her exceptional mentorship, continuous support, and insightful guidance throughout this study. Her encouragement and constructive feedback have played a vital role in shaping this work and enabling me to complete it with confidence.

I would also like to extend my sincere appreciation to the Head of the Department of Mechanical Engineering, **Dr. Muhammad Mahabat Khan**, for providing access to the High Performance Computing Laboratory and other essential departmental resources. The availability of advanced computational facilities was of great value in carrying out the numerical work and simulations for this research.

Lastly, I would like to acknowledge my friends and colleagues for their encouragement, meaningful discussions, and companionship during the course of this work.

To all of you, I remain forever grateful.

**(Muhammad Usman Shahid)**

# *Abstract*

Vertebral compression fractures (VCFs) are a common complication of osteoporosis, trauma, and malignancy, often requiring surgical intervention. Current treatments, such as vertebroplasty and kyphoplasty, have limitations in restoring the complex biomechanical properties of the native vertebral bone. This work introduces a biomimetic design approach for the L4 vertebra using Triply Periodic Minimal Surface (TPMS) structures. Six candidate structures (Gyroid, Diamond, Schwarz, Lidinoid, Neovius, and SplitP) were analyzed via Asymptotic Homogenization, from which Neovius and SplitP were selected at an optimal relative density of 0.2 (80% porosity) due to their ability to match the elastic modulus of cancellous bone while preserving high porosity for osseointegration.

Finite Element Analysis (FEA) confirmed that both structures achieved physiological stress distribution and maintained vertebral height restoration under loading. To evaluate mass transport, Computational Fluid Dynamics (CFD) was conducted across physiologically relevant inlet velocities of 0.5–0.8 mm/s. Under Newtonian flow, SplitP and Neovius exhibited permeability values of $3.28865 \times 10^{-6}$ to $3.19063 \times 10^{-6}$ m$^2$ and $3.28712 \times 10^{-6}$ to $3.18908 \times 10^{-6}$ m$^2$, respectively, with corresponding Wall Shear Stress (WSS) ranges of 0.00022–0.00036 Pa and 0.00013–0.00045 Pa. Under non-Newtonian conditions, permeability decreased to $1.54995 \times 10^{-6}$ to $1.53616 \times 10^{-6}$ m$^2$ for SplitP and $1.54954 \times 10^{-6}$ to $1.53579 \times 10^{-6}$ m$^2$ for Neovius, while WSS increased to 0.0013–0.0018 Pa and 0.0015–0.0022 Pa, respectively. These values confirm stable permeability and WSS conducive to nutrient transport and osteogenic stimulation. The results suggest that TPMS-based implants, particularly the SplitP-based L4 vertebral body, offer a promising solution for biomimetic lumbar vertebral implants to treat VCFs and improve clinical outcomes.

# Contents

# List of Figures

# List of Tables

# Abbreviations

| | |
|---|---|
| **3D** | Three Dimensional |
| **AM** | Additive Manufacturing |
| **ASTM** | American Society for Testing and Materials |
| **BCC** | Body-Centered Cubic |
| **CAD** | Computer Aided Design |
| **CFD** | Computational Fluid Dynamics |
| **CT** | Computed Tomography |
| **FEA** | Finite Element Analysis |
| **FGM** | Functionally Graded Material |
| **ISO** | International Organization for Standardization |
| **MPa** | Megapascal |
| **STL** | Stereolithography |
| **TPMS** | Triply Periodic Minimal Surface |
| **VCF** | Vertebral Compression Fracture |
| **WSS** | Wall Shear Stress |

# Symbols

| | | |
|---|---|---|
| $\mu$ | Dynamic viscosity | kg/(m·s) |
| $\mu_a$ | Apparent viscosity | kg/(m·s) |
| $\mu_{\min}$, $\mu_{\max}$ | Minimum and maximum viscosity cutoffs | kg/(m·s) |
| $\gamma$ | Shear rate | $s^{-1}$ |
| $\rho$ | Fluid density | $kg/m^3$ |
| $u$ | Fluid velocity | m/s |
| $L$ | Characteristic length / model length | m |
| $K$ | Consistency index (power-law fluid) | mPa·$s^n$ |
| $n$ | Power-law exponent | – |
| $\Delta p$ | Pressure drop | Pa |
| $k_0$ | Permeability (Newtonian) | $m^2$ |
| $k_n$ | Permeability (non-Newtonian) | $m^2$ |
| $Re$ | Reynolds number | – |
| $E$ | Young's modulus | MPa |
| $\sigma$ | Stress (generic) | MPa |
| $\sigma_{vm}$ | von Mises stress | MPa |
| $u_{\max}$ | Maximum deformation | mm |
| $WSS$ | Wall shear stress | Pa |

# Chapter 1

# Introduction

## 1.1 Background

The human spine, a complex and dynamic structural system, plays a crucial role in providing mechanical support, facilitating movement, and protecting the spinal cord. Among its five distinct regions, the lumbar spine bears particular significance due to its substantial load-bearing responsibilities and contribution to lower back mobility. The lumbar vertebrae, numbered L1 through L5, exhibit distinctive anatomical and biomechanical characteristics that reflect their specialized functions in maintaining posture, supporting body weight, and enabling a range of movements essential for daily activities. Within this region, the fourth lumbar vertebra (L4) occupies a critical position between the upper and lower segments of the lumbar spine, experiencing unique biomechanical stresses that make it susceptible to specific pathologies and consequently an important focus for biomimetic design and analysis [1].

Pathologies affecting the lumbar vertebrae, particularly L4, constitute a significant clinical burden worldwide. Conditions such as degenerative disc disease, vertebral fractures, spondylolysis, and various neoplastic processes frequently necessitate surgical intervention, including vertebral body replacement or stabilization. Traditional approaches to these conditions have typically employed artificial implants that, while functional, often fail to replicate the complex biomechanical properties

of native vertebral structures. The consequences of this biomechanical mismatch can include implant subsidence, adjacent segment disease, and mechanical failure. For instance, acquired spondylolysis of lumbar vertebrae has been documented as a potential complication following long spinal fusion surgeries, highlighting the importance of understanding and preserving natural biomechanical relationships when designing spinal interventions [2].

Conventional bone scaffold manufacturing techniques face several limitations that hinder their effectiveness. Firstly, they offer limited control over scaffold structure, often resulting in irregular designs that compromise mechanical properties and cause uneven nutrient and growth factor distribution. Secondly, these methods struggle to replicate the complex architecture of natural bone tissue, leading to scaffolds with poor biological activity and host tissue compatibility. Additionally, reliance on manual processes introduces human error, reducing reproducibility and quality control. Scalability is another challenge, as conventional techniques are labor-intensive and time-consuming, making large-scale production difficult. High costs due to expensive equipment and materials further restrict accessibility. Collectively, these limitations impair mechanical strength and nutrient transport, ultimately affecting structural support and tissue regeneration efficiency.

Recent advancements in additive manufacturing (AM) and Triply Periodic Minimal Surface (TPMS) structures have further expanded the possibilities for the creation of patient-specific, biomimetic lumbar vertebral bodies. AM facilitates the fabrication of complex geometries with tailored mechanical properties, while TPMS structures offer high strength-to-weight ratios and adjustable porosity, closely resembling the trabecular bone found in vertebral bodies [3].

## 1.2 Lower Back Pain and Associated Statistics

Lower back pain (LBP) is a leading cause of disability worldwide, affecting 619 million people in 2020 (nearly 10% of the world's population), with projections reaching 843 million by 2050. It imposes a significant economic burden, costing the

UK's NHS £5 billion annually and the USA US$134 billion in 2016. Productivity losses are severe, with Brazil reporting 100 workdays lost per person per year. Despite its high prevalence, funding remains inadequate, with the US National Institute of Health (NIH) reducing its LBP research budget from US$170 million in 2019 to US$69 million in 2023. The COVID-19 pandemic further exacerbated LBP cases due to inactivity, poor ergonomics, and limited healthcare access [4]. The global market for chronic LBP treatment was valued at USD 2.70 billion in 2024, with projections indicating significant growth to approximately USD 6.12 billion by 2033. This expansion reflects a compound annual growth rate (CAGR) of 9.52% throughout the forecast period (2024-2033) as shown in Figure 1.1, demonstrating the increasing clinical and economic importance of effective therapeutic solutions for this prevalent condition [5].

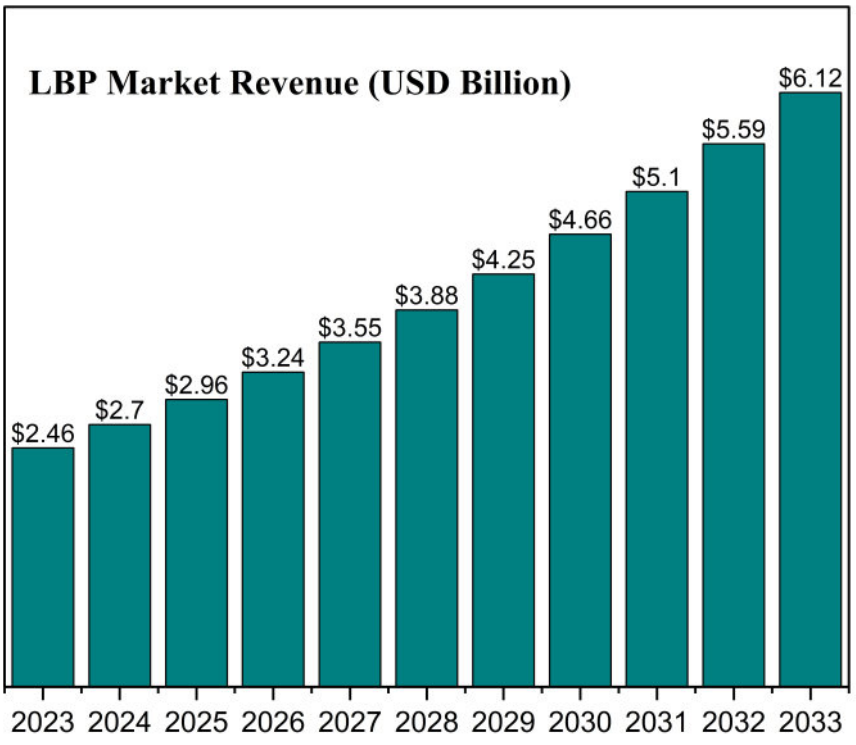


FIGURE 1.1: LBP market size from 2023 to 2033 (USD Billion) [5]

Approximately 85% of individuals will encounter LBP at some point in their lives, with around 45% experiencing it each year. Among those who suffer from LBP, 5-10% endure significant health issues as a result, leading to high healthcare expenses, reduced physical activity, and a lower quality of life [6]. LBP remains the leading cause of years lived with disability (YLD), with prevalence highest in older

adults and females. Disability related to LBP rose across all age groups from 1990 to 2019, peaking in the 50-54 age group in 2019. Notably, around 70% of years lost due to disability occurred among working-age individuals (20-65 years) [7]. The global age-standardized prevalence rate was 7,460 per 100,000 in 2020, with Central and Eastern Europe showing the highest rates. Key risk factors include poor occupational ergonomics (22% of YLDs), smoking (12.5%), and high BMI (11.5%) [8]. LBP statistics from Shifa International Hospital, Pakistan, reveal key insights into its prevalence and risk factors. The study involved 375 patients, with a slight majority being men (51.7%). The most affected age group was 21–40 years (48%), followed by 41–60 years (30.9%). LBP among different age groups is shown in Figure 1.2.

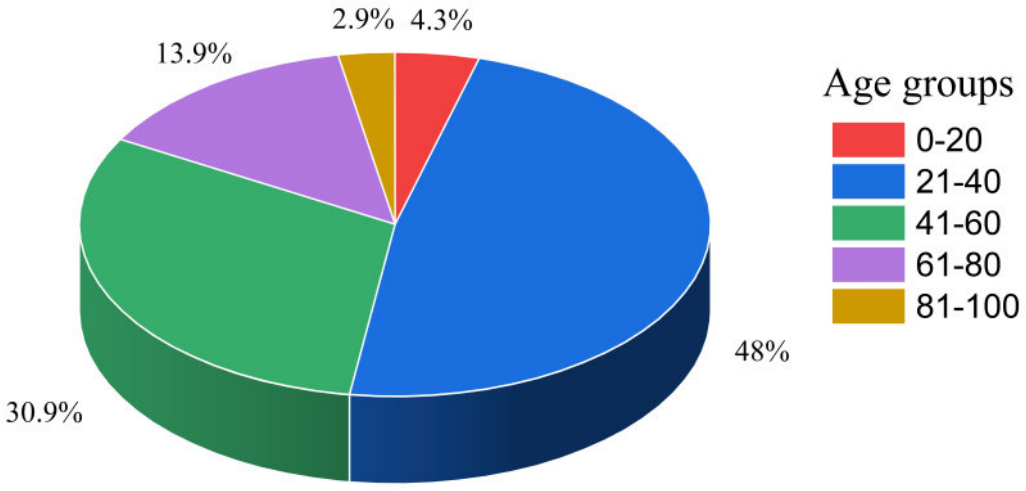


FIGURE 1.2: LBP among different age groups [9]

Chronic back pain was predominant (78.4%). Housewives (30.1%), office workers (18.1%), and private job holders (14.7%) were the most affected professions. Major risk factors included lack of exercise (76.3%), prolonged sitting (50.4%), heavy weight lifting (48.5%), and use of soft foam mattresses (52.0%). Psychological factors such as sleep disorders (41.6%), anxiety (39.5%), and depression (28.8%) were also significant [9]. As LBP cases continue to rise, innovative spinal treatments, including biomimetic vertebral body designs, are essential to addressing this growing health challenge.

## 1.3 Overview of Lumbar Spine Anatomy

The lumbar spine, located between the thoracic and sacral regions, consists of five large vertebrae (L1-L5) that provide structural support and mobility to the lower back as shown in Figure 1.3. These vertebrae are larger than those in other

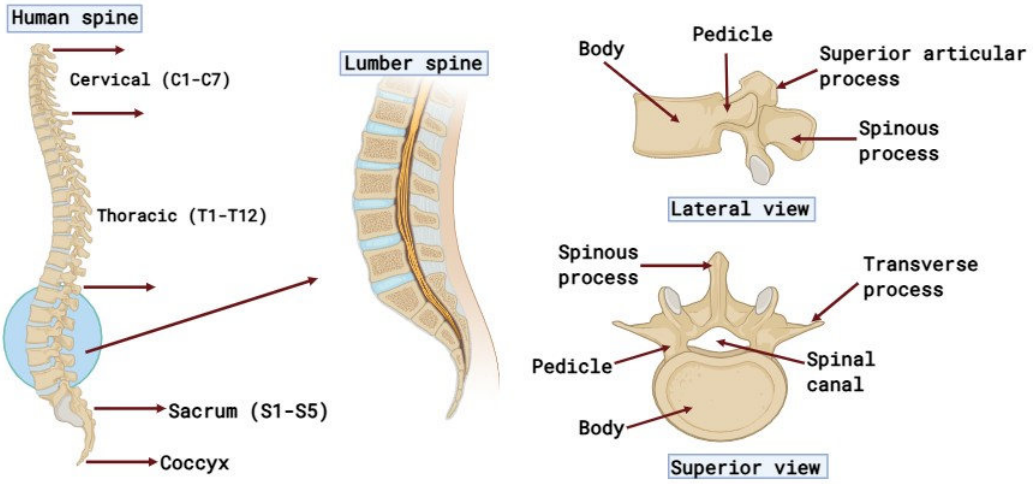


FIGURE 1.3: Lumber spine anatomy

spinal regions, allowing them to bear substantial loads and absorb axial forces from the upper body. The lumbar spine exhibits a natural inward curvature, known as lordosis, which aids in weight distribution and movement. Intervertebral discs between the vertebrae act as shock absorbers, while facet joints facilitate motion. Ligaments and muscles further enhance stability, and the lumbar spine also houses the cauda equina, a bundle of nerve roots responsible for lower limb function. Functionally, the lumbar spine supports the upper body, protects the spinal cord, and enables diverse movements, including flexion, extension, rotation, and lateral bending. Its complex anatomy includes vertebral bodies, pedicles, laminae, spinous and transverse processes, and zygapophyseal (facet) joints. The lumbar intervertebral discs, composed of a nucleus pulposus and annulus fibrosus, provide cushioning and flexibility. Ligaments such as the anterior and posterior longitudinal ligaments, ligamentum flavum, and interspinous ligaments contribute to spinal stability. Understanding this complex structure is crucial for diagnosing lower back disorders and advancing biomimetic vertebral implants to improve spinal treatment for compression failures and other pathologies [10, 11].

## 1.4 Diseases of the Lumbar Spine

The lumbar spine is susceptible to various pathological conditions that significantly impact patient quality of life and spinal biomechanics. Among these, compression failures represent a critical area of focus for the development of biomimetic vertebral replacements, particularly for the L4 vertebra, which bears substantial physiological loads within the lumbar region.

### 1.4.1 Vertebral Compression Fractures: Mechanisms and Classification

Vertebral compression fractures (VCFs) constitute a significant portion of lumbar pathology, characterized by the mechanical failure of the vertebral body under compressive loading. These fractures primarily occur through a flexion-compression mechanism that affects the anterior column, including the anterior longitudinal ligament and the anterior half of the vertebral body. In younger individuals, 50% of VCFs result from car accidents, while another 25% are caused by falls [12]. The occurrence of VCFs is directly related to age, as bone density gradually declines, leading to a loss of nearly 50% of normal axial bone mass by the age of 80 [13]. The biomechanical failure typically manifests in three distinct patterns: wedge fractures (anterior collapse with preserved posterior elements), crush fractures (uniform compression throughout the vertebral body), and burst fractures (catastrophic vertebral body failure with potential for canal compromise) [14, 15].

Osteoporosis remains the predominant cause of vertebral compression fractures, particularly in postmenopausal women and elderly populations. The pathological reduction in bone mineral density compromises the structural integrity of the vertebral bodies, making them susceptible to failure even under normal physiological loads. Other etiologies include traumatic injury, metastatic disease, and primary bone tumors, each presenting unique challenges for treatment and reconstruction [14]. The VCF in lumber spine is shown in Figure 1.4.

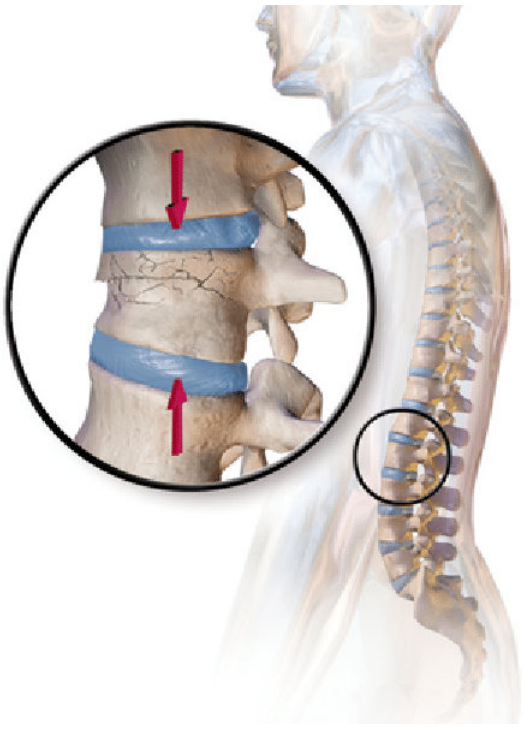

FIGURE 1.4: VCF in lumber spine [16]

### 1.4.2 Clinical Presentation and Functional Impact

The hallmark symptom of lumbar compression fractures is axial, non-radiating back pain that corresponds to the fracture site. Pain may be severe and disabling, presenting as aching or stabbing in quality. However, in elderly patients with severe osteoporosis, fractures may occasionally occur spontaneously without significant pain. The functional impact of these fractures extends beyond acute symptoms, with disability potentially persisting for five or more years and pain lasting approximately 2-4 years. Progressive compression fractures produce characteristic changes in spinal alignment. Multiple fractures, particularly at the thoracolumbar junction, can lead to the development of excessive kyphosis (commonly referred to as a "dowager's hump"), progressive loss of stature, and altered biomechanics throughout the spine.These structural changes further contribute to fatigue of the paraspinal musculature as the body attempts to maintain posture, creating a cycle of chronic pain and functional limitation even after the original fractures have healed [14].

## 1.5 Treatments of the Lumbar Spine

### 1.5.1 Conservative Management for VCFs

Conservative treatment remains the initial approach for most stable vertebral compression fractures. This typically involves pain management with analgesics (NSAIDs, muscle relaxants, and occasionally opioids), activity modification, and bracing [17]. Many patients with VCFs seek both pain alleviation and functional recovery, though conservative treatments offer only moderate improvement. For individuals with mild symptoms, medication and lifestyle adjustments may aid recovery, while these methods can also complement procedural interventions when necessary. Although opioids are commonly prescribed for pain management, their potential for dependency and overuse, particularly in prolonged treatment, raises concerns that may outweigh their benefits [18, 19]. These limitations demonstrate the need for alternative interventions. Nevertheless, conservative treatments remain valuable for symptom relief, particularly in resource-limited settings where access to advanced medical procedures may be restricted.

Conservative management is often the first-line treatment for stable osteoporotic VCFs. However, its effectiveness can be limited, and some patients may not respond adequately, necessitating more invasive procedures like vertebroplasty or kyphoplasty [20, 21]. The lack of standardized guidelines for conservative management further complicates treatment, highlighting the need for more research to establish best practices [22].

### 1.5.2 Vertebral Augmentation Procedures

Kyphoplasty and vertebroplasty, the primary methods of vertebral augmentation, have been utilized for many years to address VCFs. Both procedures involve percutaneous injection of bone cement (typically polymethylmethacrylate, PMMA) into the fractured vertebral body [23]. Vertebroplasty is a procedure where bone cement is injected directly into the fractured vertebra under fluoroscopic guidance.

This approach provides immediate structural support and pain relief by stabilizing the fracture fragments. However, it may not restore vertebral height and has been associated with cement leakage, a significant complication that can lead to neurological symptoms or further instability. Kyphoplasty is a variation of vertebroplasty that involves the use of an inflatable balloon to create a void within the fractured vertebral body before cement injection. This balloon inflation helps restore some of the lost vertebral height and reduces kyphosis, potentially improving spinal alignment and reducing the risk of adjacent segment fractures. Kyphoplasty has been shown to provide better height restoration and kyphosis correction compared to vertebroplasty, although both procedures offer similar pain relief [24]. Vertebral augmentation procedures offer a valuable treatment option for patients with painful VCFs, particularly those who have failed conservative management. Vertebral augmentation techniques have been compared to conservative management in several studies. These procedures can offer quicker pain relief and improved mobility in the short term compared to conservative treatment, but their long-term benefits and safety remain uncertain. Despite these advantages, they are not substitutes for managing the underlying osteoporosis to prevent future fractures [25].

The limitations of traditional treatments for lumbar spine pathologies, such as vertebral augmentation and fusion surgeries, have driven the development of biomimetic approaches. These novel methods aim to replicate the natural structure and biomechanical properties of the spine, addressing challenges like stress shielding, adjacent segment degeneration, and implant subsidence associated with conventional techniques.

## 1.6 Synthetic Implants

Synthetic implants are artificial devices made from various biocompatible materials designed to replace or support damaged tissues, particularly in orthopedic and reconstructive applications. These implants are engineered to restore function,

provide mechanical stability, and integrate with the host tissue while minimizing adverse reactions.

### 1.6.1 Types of Synthetic Implants

#### 1.6.1.1 Metallic Implants

Metals such as titanium and its alloys are the most commonly used materials for orthopedic implants due to their excellent strength, corrosion resistance, and biocompatibility. Titanium alloys, in particular, are favored for femoral stems in total hip arthroplasty because of their favorable mechanical properties and ability to promote osseointegration. Cobalt-chromium alloys are also widely used for their superior fatigue resistance and wear properties, making them suitable for load-bearing implants and surgical instruments. Recent advances include biodegradable metal alloys that provide temporary support while interacting positively with the biological environment, and surface modifications with biomolecules to accelerate bone integration and reduce inflammation and infection risks [26].

#### 1.6.1.2 Ceramic Implants

Ceramics such as alumina and zirconia have been used in orthopedic implants for their excellent hardness, wear resistance, and biocompatibility. Oxidized zirconium combines ceramic surface properties with a metal substrate to improve wear resistance. Bioceramics like hydroxyapatite (HA) and beta-tricalcium phosphate ($\beta$-TCP) are osteoconductive and osteoinductive, supporting bone regeneration and gradually degrading to be replaced by natural bone. These ceramics are increasingly used in bone defect repair and as coatings to enhance implant integration [27].

#### 1.6.1.3 Polymeric Implants

Synthetic polymers like polymethylmethacrylate (PMMA) are extensively used as bone cements to fix implants and fill bone defects. PMMA is valued for its biocompatibility, ease of handling, and affordability; however, it is bioinert and does not chemically bond with bone, which can lead to micromotion and potential aseptic loosening. Efforts to improve PMMA include surface modifications and incorporation of bioactive agents to enhance osteoconductivity. Biodegradable polymers are also being developed to serve as temporary scaffolds that degrade as new bone forms, reducing the need for secondary surgeries [28].

## 1.7 Lattice Structures

In recent years, lattice structures have attracted significant interest in biomedical engineering due to their adaptable mechanical behavior, making them highly suitable for medical implants. These structures offer exceptional design flexibility—their strength, stiffness, and energy absorption can be precisely adjusted by modifying their relative density without altering their overall geometry. This tunability, combined with the ability to select different cell types, allows for customized implant properties that minimize stress shielding while promoting fluid flow through their porous architecture. Furthermore, their relative density can be varied locally, enabling the development of functionally graded lattice structures optimized for specific biomechanical demands [29].

### 1.7.1 Strut or Beam Based Lattice Structures

A prominent category within lattice structures is the strut or beam-based lattice structure as shown in Figure 1.5. These are formed by the periodic arrangement of straight or curved beams (struts) that intersect at nodes, creating a network of interconnected elements. The design of strut-based lattices can be homogeneous,

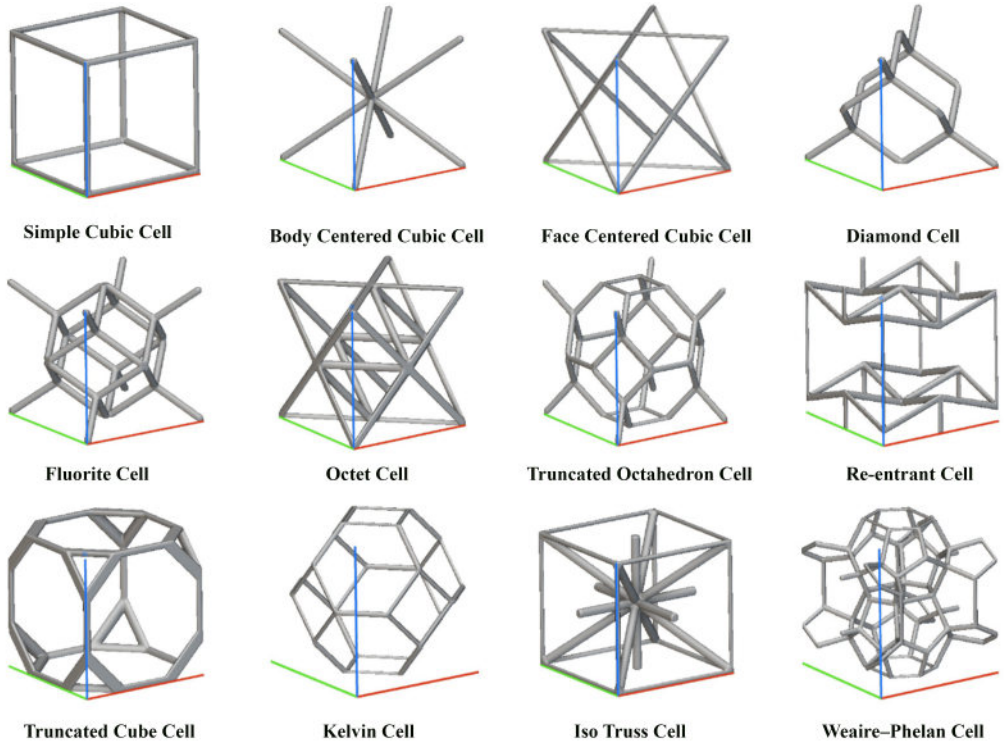


FIGURE 1.5: Strut based lattice structures [30]

with uniform strut thickness throughout, or heterogeneous, where strut dimensions vary spatially to achieve graded mechanical properties tailored to specific anatomical or load-bearing requirements. Strut-based lattices are particularly valued in spinal and orthopedic applications for their ability to provide structural support while maintaining sufficient porosity for tissue integration. By adjusting parameters such as strut diameter and unit cell configuration, engineers can fine-tune the elastic modulus and strength of the implant, achieving a balance between mechanical performance and biological functionality. The use of biocompatible metals like titanium alloys in these lattice structures further enhances their suitability for load-bearing implants, as they combine high strength with favorable surface characteristics for bone attachment [31, 32].

### 1.7.2 Triply Periodic Minimal Surface (TPMS) Structures

In the evolution of structural designs for biomedical implants and engineering applications, beam-based structures were once the predominant choice due to their

simplicity, ease of fabrication, and well-understood mechanical behavior. These structures, typically composed of interconnected beams or struts, provided sufficient strength and stiffness for many applications, including spinal implants. However, their inherent limitations including, biomechanical mismatch, stress concentration, and limited porosity and connectivity, have prompted a shift toward more advanced designs, such as TPMS, which offer superior performance in critical areas [33].

To address these challenges, researchers have turned to TPMS structures as a superior alternative as shown in Figure 1.6. TPMS are mathematically defined

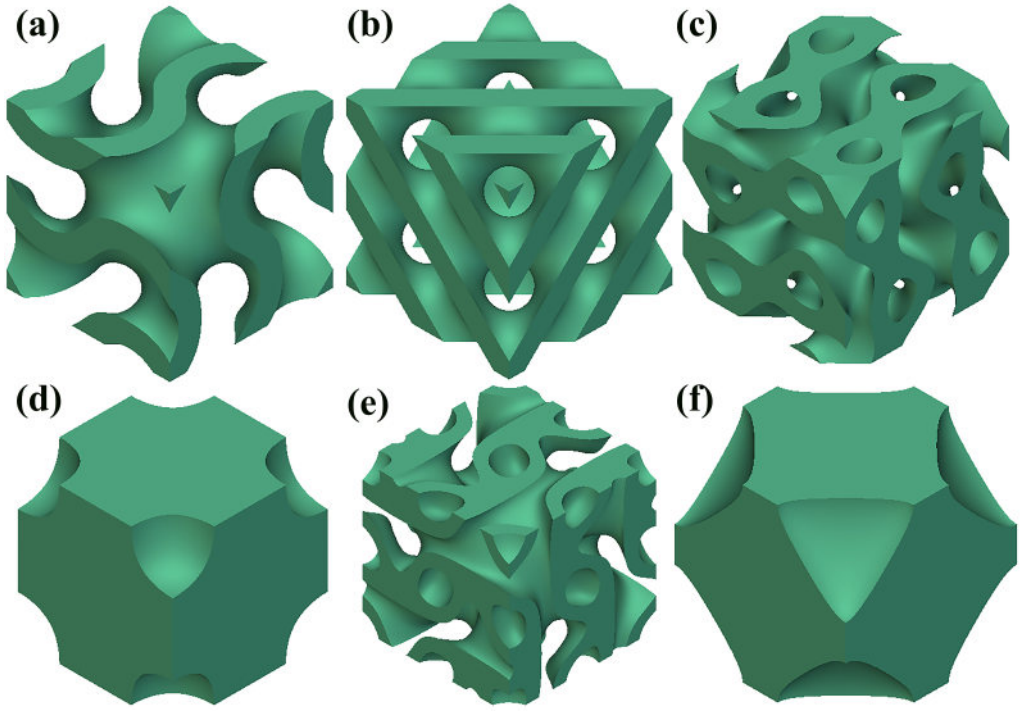


FIGURE 1.6: TPMS structures (a) Gyroid (b) Diamond (c) SplitP (d) Neovius (e) Lidinoid (f) Schwarz

surfaces characterized by continuous, smooth geometries that minimize stress concentrations and optimize mechanical performance. Unlike beam-based lattices, TPMS structures distribute loads evenly across their surface and exhibit isotropic mechanical properties, making them ideal for applications requiring both strength and flexibility. TPMS structures mimic the trabecular architecture of natural bone more effectively than beam-based designs. The highly interconnected porous networks of TPMS structures facilitate bone ingrowth and vascularization [34].

The elastic modulus of TPMS structures can be precisely controlled by adjusting parameters such as pore size and surface thickness. This allows for better matching with the mechanical properties of native bone, reducing stress-shielding effects [35].

## 1.8 Additive Manufacturing (AM)

Additive manufacturing (AM) has emerged as a pivotal technology for fabricating complex structures, particularly those based on TPMS. The integration of AM with TPMS enables the precise creation of these complex designs, which closely mimic the architecture of natural bone. Techniques such as selective laser melting (SLM) and electron beam melting (EBM) allow for the fabrication of TPMS-based implants with tailored mechanical properties, including elastic moduli that can be adjusted to match those of cancellous bone [35, 36]. This capability is crucial for reducing stress shielding and enhancing osseointegration, key factors in the long-term success of implants. The use of AM to produce TPMS structures also facilitates the creation of functionally graded materials, where properties such as porosity and stiffness can be varied across the implant to better replicate the natural gradients found in bone. This level of customization and precision has positioned AM as a critical tool for developing next-generation biomimetic implants that can effectively restore both the anatomical and biomechanical functions of native tissues [37].

## 1.9 Research Problem Statement

Current lumbar vertebral implants face significant limitations in replicating the complex biomechanical properties of natural bone, often resulting in stress shielding and implant subsidence. Conventional designs such as solid metals or simple porous structures fail to match the anisotropic stiffness, strength, and permeability of trabecular bone, leading to long-term complications such as adjacent

segment degeneration. While AM enables complex geometries, optimal scaffold architectures that simultaneously satisfy mechanical, biological, and manufacturing constraints remain underexplored. This research addresses these challenges by developing a TPMS-based biomimetic implant that precisely emulates the L4 vertebra's mechanical behavior while enhancing permeability for bone ingrowth. By utilizing computational design, this work aims to overcome the limitations of current implants and provide a solution for vertebral body reconstruction.

## 1.10 Research Objectives

The main objective of this research is to develop a biomimetic L4 vertebral implant that replicates natural bone's mechanical properties and enhances permeability for optimal osseointegration. The objectives include:

1. To design a TPMS-based implant mimicking natural human L4 vertebral body architecture.
2. To design and identify optimal lattice structures and porosity levels through homogenization analysis for matching bone-like mechanical properties.
3. To perform finite element analysis to evaluate stress distribution and deformation under physiological loading.
4. To assess permeability of the porous L4 vertebrae using computational fluid dynamics for evaluating bone ingrowth potential.

## 1.11 Report Structure

This thesis is structured into five chapters to systematically explore the development of biomimetic lumbar vertebral implants using TPMS structures. Chapter 1 introduces the lumbar spine's biomechanics, common pathologies like VCFs, and the limitations of current treatments, while highlighting the potential of TPMS

and AM technologies. Chapter 2 reviews existing literature on spine degeneration, treatment options, and the advantages of biomimetic designs, emphasizing TPMS structures' mechanical and biological benefits. Chapter 3 outlines the research methodology, including geometric modeling, methodology for Finite Element Analysis (FEA), and Computational Fluid Dynamics (CFD) to assess implant performance. Chapter 4 presents and discusses simulation results, comparing TPMS architectures for strength, permeability, and osseointegration potential. Finally, Chapter 5 summarizes key findings and suggests future research directions.

# Chapter 2

# Literature Review

## 2.1 Introduction to Lumbar Spine Degeneration

Vertebral compression fractures (VCFs) occur when spinal bones collapse, often due to osteoporosis, trauma, or diseases that weaken bone structure. Traumatic causes include high-impact injuries, such as falls from heights or car accidents, where force is transmitted through the spine. Medical conditions like osteoporosis, multiple myeloma, metastatic cancer, and Paget's disease increase fracture risk by compromising bone strength [38]. Osteoporosis is one of the most common bone diseases in the elderly population today. It is a prevalent metabolic bone disorder that significantly increases the risk of fractures, particularly VCFs, which are common in the lumbar region of the spine. Vertebral fracture may result in pain about the fracture site, loss of height caused by vertebral collapse, spinal instability, and, in many cases, kyphotic deformity. Although some patients respond to the conservative treatment of medications, bracing, and bed rest, many do not. Chronic pain and kyphotic deformity may lead to depression, decreased appetite (leading to poor nutrition), decreased pulmonary function, impaired mobility, and a reduction in the quality of life, the ultimate result being a significant increase in morbidity. To relieve chronic pain, bed rest is often the only solution. However, this solution can result in a vicious cycle of increased bone loss caused by inactivity and, correspondingly, increased vertebral fracture risk [39].

Globally, osteoporosis affects millions, with vertebral fractures being a predominant concern due to their impact on mobility and quality of life [40]. Annually, there are approximately 1.4 million new cases of VCFs in Europe alone, highlighting the widespread nature of this issue [41]. In the United States, VCFs are the most common complication of osteoporosis, with around 700,000 cases reported each year. These fractures often occur without significant trauma and can lead to severe pain, loss of vertebral height, and spinal deformity, particularly in the thoraco-lumbar region [39]. The prevalence of these fractures is notably high among postmenopausal women, with studies indicating that up to 84% of women with suspected osteoporosis have vertebral fractures [42] . Several risk factors contribute to the development of osteoporotic VCFs, including advanced age, low bone mineral density (BMD), and certain medical treatments such as epidural steroid injections, which have been shown to increase fracture risk [43]. Additionally, socioeconomic factors and comorbidities like diabetes and hypertension can exacerbate the risk. The consequences of these fractures extend beyond immediate pain, as they can lead to long-term complications such as spinal deformity and reduced mobility [44].

## 2.2 Treatment Modalities for VCFs

VCFs are a prevalent complication of osteoporosis and can also result from trauma or malignancy. The management of VCFs includes both conservative and surgical interventions, with the choice of treatment often depending on the severity of symptoms and the underlying cause of the fracture. Conservative management remains the first-line treatment for VCFs, particularly in cases where the fractures are stable and not causing significant neurological deficits. This approach typically includes pain management with medications such as nonsteroidal anti-inflammatory drugs (NSAIDs), calcitonin, and bisphosphonates, as well as physical therapy and bracing [45]. A systematic review highlighted the effectiveness of NSAIDs and teriparatide in managing pain associated with acute VCFs, suggesting these as valuable options in conservative treatment strategies. For patients

with moderate to severe pain, stronger analgesics such as opioids may be necessary to achieve adequate pain relief [46].

Common conservative treatments include bed rest, bracing, and physical therapy, each contributing uniquely to the patient's recovery. Bed rest can help reduce stress on the fractured vertebra and alleviate pain, while bracing provides external support and stabilization to the spine. Physical therapy aims to improve muscle strength, flexibility, and range of motion, enabling patients to regain functional independence [47]. However, contemporary data suggest that a significant proportion of patients undergoing conservative treatment for VCFs may fail to achieve substantial pain relief within a reasonable timeframe. Studies have shown that more than 40% of patients may not experience significant pain reduction within 12 months of symptom onset, highlighting the limitations of conservative management alone. This demonstrates the need for a more proactive and comprehensive approach that includes early mobilization, physical therapy, and activity modification [48].

Vertebroplasty (VP) and kyphoplasty (KP) are minimally invasive procedures used to treat VCFs, particularly when conservative treatments fail to provide adequate pain relief. These procedures involve the injection of bone cement into the fractured vertebra to stabilize it and alleviate pain [49]. Evidence suggests that VP provides superior pain control within the first two weeks compared to optimal medical management for osteoporotic VCFs. Similarly, KP has been shown to improve daily activity, physical function, and pain relief compared to conservative management by six months post-intervention [50]. A meta-analysis comparing VP and conservative treatment found that VP was associated with greater pain relief in the early postoperative period, with significant effects lasting up to one year [51]. However, the long-term benefits of VP over conservative treatment remain debated, with some studies indicating similar outcomes in pain control and physical function after two years [50]. Similarly, studies suggest that KP can lead to better pain relief and kyphosis correction compared to VP, making it a preferred option in cases where restoration of vertebral height and alignment is desired.

The use of balloons to create a cavity within the vertebra allows for a more controlled and precise restoration of vertebral height, which can result in improved biomechanics and reduced pain. Furthermore, the cavity created by the balloons provides a space for the bone cement to fill, reducing the risk of cement leakage [52]. A prospective randomized trial compared vertebroplasty with bracing in patients with acute VCFs. The study found that vertebroplasty provided greater immediate pain relief and improved functional outcomes compared to bracing. However, the superiority of vertebroplasty diminished over time, except for the maintenance of sagittal balance [53].

Vertebral augmentation techniques have evolved beyond traditional vertebroplasty and kyphoplasty, with the introduction of various implant systems designed to enhance vertebral stability, restore height, and minimize complications. Vertebral body stenting (VBS) is one such technique, aiming to increase the effectiveness in restoring segmental alignment by providing additional support to the fractured vertebra. VBS involves the insertion of a stent-like device into the vertebral body, which is then expanded to restore height and provide a framework for cement injection. The KIVA system represents another advancement in vertebral augmentation, designed to prevent cement leakage, a common complication associated with vertebroplasty and kyphoplasty. The KIVA system utilizes a flexible PEEK (polyetheretherketone) polymer cord that is implanted within the vertebral body to create a channel for cement injection, reducing the risk of extravasation. The KIVA system is thought to provide better cement containment and distribution, leading to improved outcomes [54]. Furthermore, SpineJack is an FDA-approved treatment modality for VCFs, offering a different approach to vertebral augmentation with reported clinical efficacy comparable to the gold-standard balloon kyphoplasty. The SpineJack system consists of expandable titanium implants that are inserted into the vertebral body to restore height and provide support. The implants are designed to be minimally invasive and can be adjusted to achieve the desired height and alignment [55].

## 2.3 Limitations of Conventional Implants

Conventional implants often face significant challenges, primarily due to poor integration with bone and a mismatch in stiffness, leading to stress shielding. This mismatch can result in the implant absorbing more stress than the surrounding bone, causing bone resorption and weakening over time. Additionally, conventional implants are prone to risks such as implant loosening, subsidence, and mechanical failure, which can compromise their long-term stability and effectiveness [56, 57]. Achieving effective osseointegration is crucial for the long-term success of implants, but conventional materials sometimes fall short. Osseointegration involves the direct structural and functional connection between bone and the implant surface. Without adequate osseointegration, the implant may become unstable and fail [58].

Factors such as implant surface properties and biocompatibility play significant roles in osseointegration. The surface characteristics of the implant influence cell adhesion, proliferation, and differentiation, all of which are essential for bone formation. Biocompatibility refers to the ability of the implant material to be accepted by the body without eliciting an adverse immune response [59]. Insufficient bone regeneration and integration can result from mismatched biomechanics and poor bioactivities. If the implant does not provide adequate mechanical stimulation to the surrounding bone or if it lacks the necessary bioactive cues, bone regeneration may be compromised. This can lead to a weakened bone-implant interface and eventual implant failure [58]. The use of dense materials like titanium (Ti), while providing high strength and durability, can inadvertently lead to stress shielding due to their significantly higher elastic modulus compared to bone. This means that the implant bears a disproportionate amount of the load, while the surrounding bone is shielded from the normal stresses it requires to maintain its density and strength. Over time, this can result in bone loss around the implant, creating a vicious cycle of further stress shielding and bone resorption [60]. Research comparing Ti and stainless steel (SS) implants revealed distinct patterns of gene expression, matrix deposition, and mineralization in response to the different materials. In particular, Ti implants demonstrated stronger integration strength

compared to SS alternatives, a finding consistent across preclinical and clinical studies [61].

## 2.4 Role of Biomimetic Design: Finite Element Studies

Biomimetic implants are designed to mimic the natural structure and function of biological tissues, offering solutions to the limitations of conventional implants [62]. Achieving the right balance of porosity, stiffness, and load distribution is critical for successful bone scaffold design. These parameters influence cell behavior, bone ingrowth, and the overall mechanical performance of the implant. The porosity of the scaffold affects cell adhesion, migration, proliferation, and differentiation. The porosity levels can be adjusted to match the natural bone, with a study showing that structures with porosities ranging from 70% to 95% can effectively mimic the mechanical properties of trabecular bone [63]. The stiffness of the scaffold influences cell morphology, gene expression, and the production of extracellular matrix. The load distribution within the scaffold affects cell alignment, bone remodeling, and the overall mechanical strength of the implant. Optimizing these factors can lead to better integration with the host bone and improved clinical outcomes [64, 65].

Biomimetic implants replicate this structural intelligence through lattice geometries based on Triply Periodic Minimal Surfaces (TPMS), which provide surface curvature distributions matching those found in natural trabecular networks. TPMS structures, such as the diamond-type, are designed to match the elastic modulus and compressive strength of human bone, reducing stress shielding and promoting better integration with the host tissue [66]. Beyond their curvature compatibility, TPMS-based structures offer several additional benefits. For instance, their intricate internal architecture enhances cellular interconnectivity, promoting more active cell differentiation [67]. Moreover, unlike conventional lattice structures, TPMS designs reduce stress concentration due to their smooth

transitions and graded porosity [68]. These unique properties make TPMS-based structures highly suitable for constructing bone scaffolds or optimizing the surface morphology of implants. A study showed that the Diamond and Split-P TPMS configurations demonstrate particular promise, showing 18–25% higher yield strength under compressive loads compared to conventional foam structures while maintaining comparable porosity levels (65–80%) [69]. The gyroid structure, in particular, has shown superior material transportation ability, which is crucial for nutrient flow and waste removal, further supporting tissue growth [70]. A study showed that the shape optimization of additively manufactured TPMS-based bone substitutes can increase stiffness and strength by up to 80% while maintaining their biomimetic morphology for future implant applications [71]. Kang et al. [72] developed a multi-objective optimization method to design a lightweight, high-strength artificial vertebral implant (AVI) based on spinal biomechanics as shown in Figure 2.1. They compared two AVI designs using finite element analysis and compression tests. The optimized implant showed 41.5% lower stress than the trussed design, remained within safe fatigue limits, and exhibited twice the compression load and stiffness per unit mass. Successful short-term clinical outcomes were also reported.

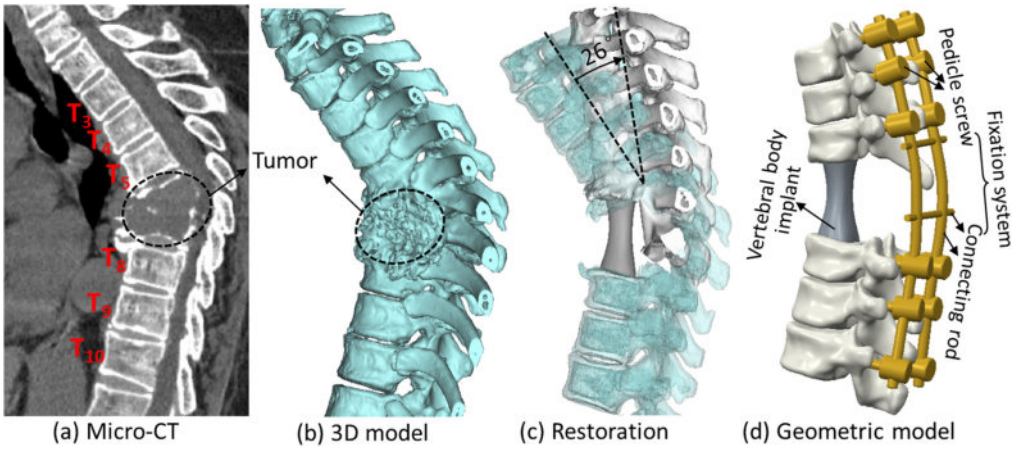


FIGURE 2.1: (a) Micro-CT (b) 3D model (c) Restoration (d) Geometric model (Reprinted with permission [72], Copyright 2021, Elsevier)

Li et al. [73] investigated the early osteointegration of Ti6Al4V-based TPMS scaffolds, demonstrating their ability to promote bone ingrowth. Notably, a stable interface between the implants and surrounding bone tissue was observed after

five weeks of implantation. In another study, Paré et al. [74] applied TPMS implants to repair craniofacial bone defects. Their findings suggested that integrating 3D-printed calcium phosphate TPMS scaffolds with cells could help overcome challenges in craniofacial bone reconstruction. The study compared bone regeneration within the defect to a standard treatment, revealing significantly enhanced new bone formation in the TPMS group after seven weeks compared to the control. A recent investigation evaluated six distinct TPMS scaffold architectures for tissue engineering applications, while developing a systematic geometric optimization approach. This methodology specifically addresses pore size requirements to facilitate capillary-mediated oxygen and nutrient transport. Comparative analysis revealed that Lidinoid and Split P cell configurations demonstrated superior cell proliferation rates, identifying them as optimal choices for bone tissue scaffolds [75].

Among the essential properties of TPMS structures for tissue regeneration or replacement, mechanical performance is undoubtedly the most critical. Guo et al. [76] conducted a comparative study between Skeletal-TPMS and strut-TPMS lattices, evaluating four TPMS architectures: Gyroid (G), Schwarz Diamond (D), Schwarz Primitive (P), and IWP. Their computational and experimental analyses revealed that at relative densities below 0.5, the P-structure demonstrated superior mechanical properties, exhibiting the highest Young's modulus and yield strength among the tested configurations. This suggests the P-structure offers optimal stiffness and strength in low-density applications. In contrast, the IWP architecture showed the lowest mechanical performance despite possessing the greatest connectivity, demonstrating that higher nodal density does not necessarily enhance structural rigidity.

Al-Ketan et al. [77] investigated the correlation between topology and mechanical properties in strut-based structure, skeletal-TPMS, and sheet-TPMS structures through quasi-static compression tests. Among all tested architectures, sheet-TPMS structures outperformed others in mechanical performance, with the Diamond TPMS variant standing out due to its exceptional properties, which remained nearly unaffected by changes in relative density. Additionally, the study

revealed that geometric effects on mechanical behavior become more significant at lower volume fractions. In another study, researchers fabricated four TPMS ceramic lattices (p-cell, gyroid, IWP, s14) using DLP 3D printing and tested their mechanical performance. The study revealed two key findings: First, compressive strength scaled directly with relative density across all architectures. Second, while IWP and s14 demonstrated comparable stress responses, strength rankings showed s14 outperforming IWP, followed by gyroid and p-cell. Notably, every structure maintained structural integrity beyond 2% strain. The s14 configuration achieved 105 MPa strength at 30.5% density, whereas gyroid exhibited 5.6 MPa strength at just 6.7% density, demonstrating exceptional performance at minimal material usage [78].

Araya et al. [79] investigated LPBF-fabricated titanium lattice structures, comparing TPMS Gyroid and Stochastic Voronoi designs. Two stress calculation methods revealed significant differences: Method A (bulk material approximation) underestimated Elastic Modulus and Yield Stress versus Method B (porosity-adjusted measurements), demonstrating the critical role of geometric accuracy in mechanical characterization. Both lattice types exhibited bone-matching properties (0.1–0.5 relative density range), suggesting excellent potential for orthopedic implants to reduce stress shielding and improve longevity. The TPMS Gyroid and Stochastic Voronoi structures achieved mechanical performance comparable to human cortical bone, confirming their suitability for load-bearing biomedical applications.

## 2.5 Permeability

Permeability quantitatively characterizes a porous medium's fluid conduction capacity, governed by porosity, pore size, orientation, tortuosity, and interconnectivity. In tissue engineering, this parameter critically influences cell infiltration and nutrient diffusion. For bone regeneration specifically, optimal permeability enhances osseointegration, while insufficient values may promote cartilaginous rather than osseous tissue formation. TPMS architectures offer distinct advantages due

to their inherent interconnectivity and tunable pore geometries, enabling precise permeability control [80]. Shahid et al. [81] computationally analyzed fluid dynamics in Diamond and SplitP TPMS scaffolds with 55–75% porosity for bone tissue engineering. They utilized nTop software for designing the TPMS structures and applied power law modeling for non-Newtonian blood flow to analyze permeability, pressure drop, and wall shear stress (WSS). Results showed that increased porosity enhanced permeability while reducing pressure drop and WSS. The study demonstrated these optimized scaffolds promote favorable cellular activities (adhesion, migration, proliferation, differentiation), establishing Diamond and SplitP architectures as promising candidates for bone regeneration applications.

Dias et al. [82] demonstrated that permeability in porous scaffolds can be precisely controlled through two key geometric parameters: porosity and unit cell size. Their systematic investigation examined nine structural variants featuring identical geometries but varying in unit cell dimensions (1, 1.4, and 1.7 mm) and porosity levels (30%, 50%, and 70%). The results revealed a direct correlation between permeability and both parameters—increasing proportionally with both higher porosity and larger unit cell size. This relationship stems from the structural consequence that larger unit cells require bigger pore dimensions to maintain equivalent porosity percentages, thereby creating less restrictive fluid pathways.

Melchels et al. [83] conducted a comparative study of scaffold architectures, evaluating a stereolithography-fabricated gyroid TPMS structure against salt-leached random pore scaffolds. While both types exhibited similar porosity and pore size characteristics, the gyroid architecture demonstrated superior performance with: 10-fold greater permeability due to unimpeded pore interconnectivity, enhanced wetting of hydrophobic surfaces, and accelerated mesenchymal stem cell sedimentation during static seeding. These advantages were attributed to the gyroid's optimized fluid pathways lacking size-restrictive interconnections present in stochastic scaffolds.

In another study, Shahid et al. [84] analyzed the fluid dynamics of diamond and

gyroid structures across 50–80% porosity ranges. Results revealed an inverse relationship between porosity and pressure drop, with diamond structures showing a decrease from 2.079 to 0.984 Pa and gyroid from 1.669 to 0.943 Pa as porosity increased. Concurrently, both architectures demonstrated increasing permeability with higher porosity: diamond ($2.424\times10^{-9}$ to $5.122\times10^{-9}$ $m^2$) and gyroid ($2.966\times10^{-9}$ to $5.344\times10^{-9}$ $m^2$). The velocity distribution showed accelerated flow in central regions, confirming the structures' enhanced fluid transport capabilities at elevated porosities.

Despite being mathematically conceptualized over a century ago, TPMS structures faced fabrication challenges until recent additive manufacturing (AM) breakthroughs. Modern AM technologies have overcome previous fabrication constraints, enabling precise production of TPMS structures with controlled architectures. These advanced techniques support the fabrication of TPMS-based scaffolds across multiple length scales using diverse materials such as metals, polymers, ceramics, and composites [85]. The choice of fabrication technique for porous biomaterials depends on the base material (polymer, ceramic, or metal). Metal-based bone substitutes can be produced using methods such as selective laser melting (SLM), selective laser sintering (SLS), conventional sintering, or titanium sheet perforation. Among biocompatible metals for bone implants, titanium and its alloys, particularly Ti6Al4V, are the preferred choice for additive manufacturing due to their superior corrosion resistance. These materials are especially compatible with powder-bed fusion techniques including SLS, SLM, and electron beam melting (EBM), making them ideal for fabricating high-performance orthopedic implants. These techniques vary significantly in their precision and ability to control critical scaffold architectural parameters [86–88].

Several studies demonstrate the clinical potential of AM-fabricated metallic scaffolds for bone regeneration. Lv et al. [89] confirmed the biocompatibility of EBM-produced Ti6Al4V hexagonal scaffolds through successful *in vitro* osteogenesis and cytocompatibility tests. Complementing these findings, Shah et al. [90] conducted long-term implantation studies comparing Ti6Al4V and CrCo alloys,

revealing similar osteoblast distribution patterns in both materials-further validating their suitability for orthopedic applications. Yavari et al. [91] developed gyroid-structured titanium implants using SLM of CP-Ti powder to enhance orthopedic bone regeneration. Through optimized laser path planning that avoided contour overlap, they achieved dense material properties (relative density ¿28%) with 71±6.2% measured porosity via micro-CT, slightly lower than the theoretical 76±0.2% target due to inherent manufacturing limitations. This work demonstrates the potential of precisely engineered gyroid implants for clinical bone repair applications while highlighting current AM process constraints.

Furthermore, Qi et al. [92] developed a Ti6Al4V spinal fusion cage featuring TPMS architectures to simultaneously promote osseointegration and maintain load-bearing capacity. Their comprehensive study compared gyroid and primitive structures through modeling, simulation, fabrication, and mechanical testing. SEM analysis revealed process-induced microcracks attributed to localized energy distribution, thermal gradients, and residual stresses during printing. While all designs met fundamental requirements, gradient-pore TPMS structures demonstrated superior performance compared to uniform-pore and non-TPMS scaffolds, highlighting the importance of optimized pore architecture in implant design.

## 2.6 Novelty of Work

To the authors' best knowledge, the application of TPMS-based biomimetic structures for lumbar vertebral implants has not been explored previously. This research introduces a novel biomimetic approach to lumbar vertebral implants by leveraging TPMS architectures that precisely replicate the mechanical properties and trabecular morphology of natural L4 vertebrae. Unlike conventional implants with uniform porosity or strut-based designs, our TPMS-based scaffold offers graded stiffness and optimized permeability to simultaneously prevent stress shielding.

# Chapter 3

# Research Methodology

## 3.1 Methodology Flowchart

The study employed an integrated computational workflow to develop and evaluate a biomimetic L4 vertebral body implant, as shown in Figure 3.1. The process began with Asymptotic Homogenization (AH) of TPMS unit cells to determine their effective mechanical properties through periodic boundary conditions, providing efficient estimation of macroscopic material properties. For the cortical bone region, a perforated architecture was created by converting CAD geometry into an implicit body, defining regions, and generating controlled porosity through cylindrical perforations. In the trabecular region, thickness-mapped TPMS lattices, specifically the SplitP and Neovius structures, were designed with varying pore size distributions, validated through ImageJ analysis for biological relevance.

The final biomimetic implant model was verified via Finite Element Analysis (FEA) in ANSYS, with mesh optimization performed using MeshLab and fTetWild to ensure computational efficiency and accuracy. FEA results validated the implant's mechanical performance under physiological loading. Additionally, Computational Fluid Dynamics (CFD) analysis assessed the implant's permeability under physiological flow conditions, essential for evaluating bone ingrowth potential and vascularization. The CFD model included multiple inlet velocities to reflect physiological blood flow ranges, enhancing permeability assessment.

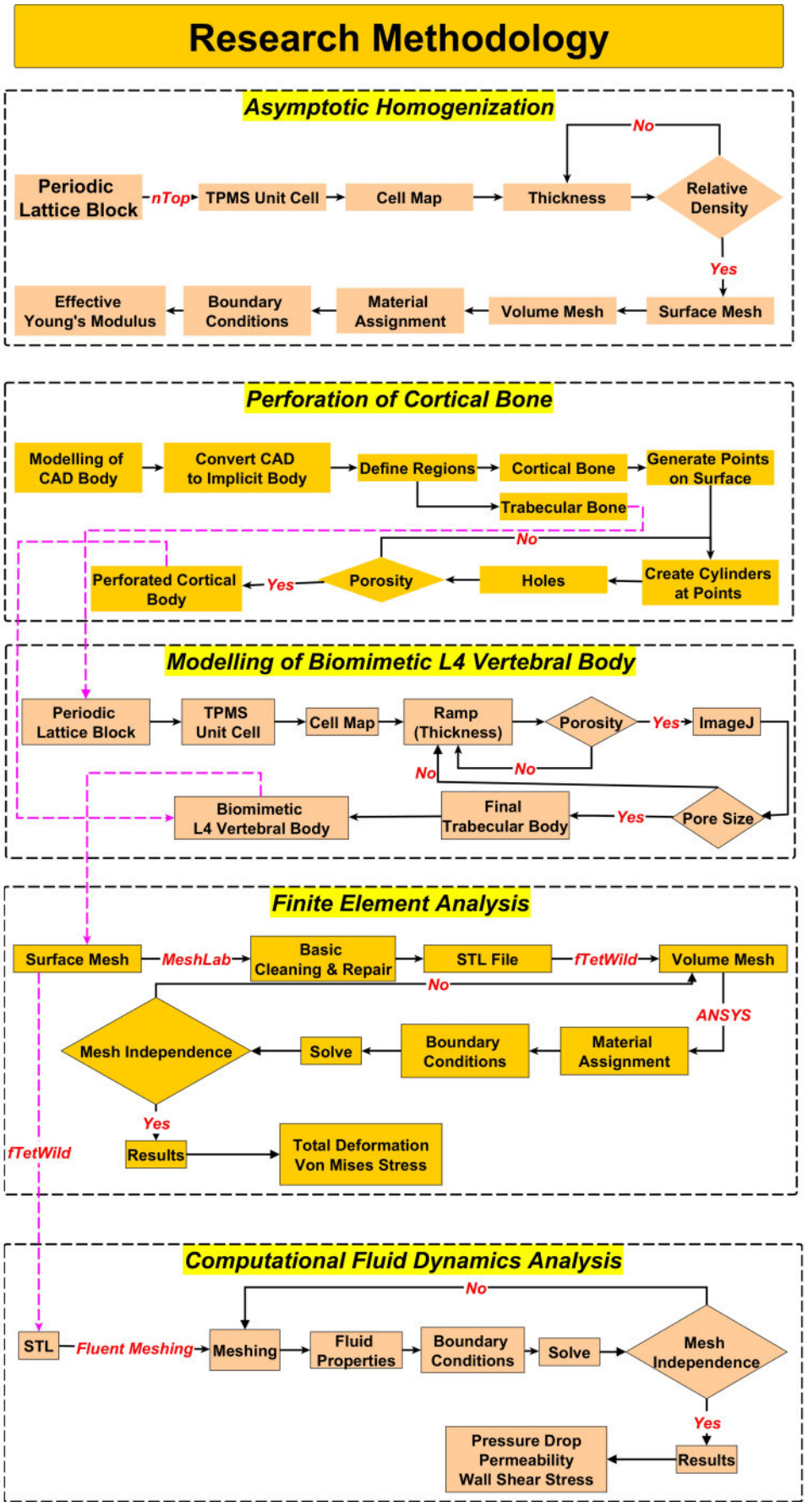


FIGURE 3.1: Comprehensive methodology flowchart for the design, modeling, and analysis of biomimetic L4 vertebral body implants

## 3.2 Asymptotic Homogenization (AH) Method

Simulating heterogeneous materials at full scale while explicitly accounting for microstructural details can be computationally intensive and time-consuming. To address this challenge, mechanical analysis methods often focus on determining the material's effective properties by examining a representative portion of the microstructure, known as the Representative Volume Element (RVE). Once these properties are derived, the heterogeneous material can be approximated as an equivalent homogeneous medium. This homogenized representation allows for efficient computation of field quantities, such as stress and strain, through the analysis of a simplified, uniform structure [93, 94]. A schematic illustration of this approach is provided in Figure 3.2.

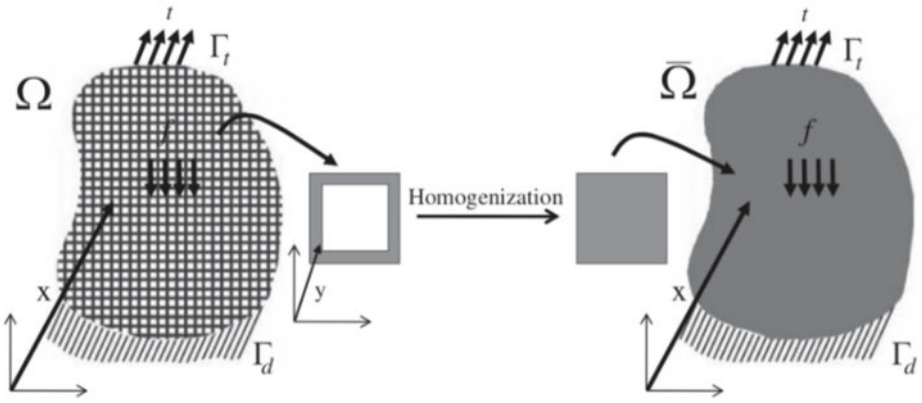


FIGURE 3.2: Homogenization concept of a cellular structure (Reprinted with permission [93], Copyright 2013, Elsevier)

While analytical solutions have proven useful in many cases, they exhibit certain limitations when applied to more complex scenarios. Among the various homogenization approaches, AH stands out as a rigorously developed theoretical framework with a strong mathematical foundation, particularly for estimating the mechanical properties of porous materials [95]. Validation against experimental data has further established AH as a reliable and precise method for such analyses. Notably, Arabnejad and Pasini have contributed significantly to this field, employing AH to determine the mechanical parameters of lattice-based materials and structures [93]. The AH method operates on the fundamental assumption that field quantities are influenced by two distinct scales: a macroscopic scale $x$

and a microscale $y = \frac{x}{\varepsilon}$, where $\varepsilon$ represents a scaling factor relating the unit cell dimensions to the macroscale material dimensions. This approach presumes that field variables, including displacement, stress, and strain, exhibit smooth variation at the macroscale while maintaining periodicity at the microscale [95, 96]. Within the AH framework, physical fields (e.g., the displacement field $\mathbf{v}$ in a porous elastic medium) can be expressed as an asymptotic expansion in powers of $\varepsilon$:

$$\mathbf{v}^{\varepsilon}(x) = \mathbf{v}_0(x, y) + \varepsilon \mathbf{v}_1(x, y) + \varepsilon^2 \mathbf{v}_2(x, y) + \cdots \tag{3.1}$$

The displacement field expansion terms $\mathbf{v}_0, \mathbf{v}_1, \mathbf{v}_2, \ldots$ exhibit $Y$-periodicity with respect to the microscopic coordinate $y$, implying that these functions assume identical values on opposite boundaries of the unit cell. Here, $\mathbf{v}_1$ and $\mathbf{v}_2$ represent microscale perturbations in the displacement field induced by the material's heterogeneous microstructure [95]. Significantly, $\mathbf{v}_0$ can be demonstrated to be independent of microscopic variations, depending solely on the macroscale coordinate $x$, and corresponds to the mean displacement field of the homogenized medium. The small deformation strain tensor can be expressed by differentiating the displacement field's asymptotic expansion relative to $x$ while applying the chain rule:

$$\boldsymbol{\varepsilon}(\mathbf{v}) = \frac{1}{2}\left[\left(\nabla \mathbf{v}_0^T + \nabla \mathbf{v}_0\right)_x + \left(\nabla \mathbf{v}_1^T + \nabla \mathbf{v}_1\right)_y\right] + O(\varepsilon) \tag{3.2}$$

where $\left(\nabla \mathbf{v}_0^T + \nabla \mathbf{v}_0\right)_x$ and $\left(\nabla \mathbf{v}_1^T + \nabla \mathbf{v}_1\right)_y$ represent the field quantity gradients in the global and local coordinate systems, respectively. By omitting terms of order $\varepsilon$ and above, the following strain tensors can be established:

$$\{\varepsilon(v)\} = \{\bar{\varepsilon}(v)\} + \{\varepsilon^*(v)\} \tag{3.3}$$

$$\{\bar{\varepsilon}(v)\} = \frac{1}{2}(\nabla v_0^T + \nabla v_0)_x, \quad \{\varepsilon^*(v)\} = \frac{1}{2}(\nabla v_1^T + \nabla v_1)_y \tag{3.4}$$

Here, $\boldsymbol{\varepsilon}^{\overline{(\mathbf{v})}}$ denotes the macroscopic (average) strain, while $\boldsymbol{\varepsilon}^*(\mathbf{v})$ represents the periodic microscale fluctuation in strain. When this strain tensor formulation is incorporated into the weak form of the equilibrium equations for a cellular domain

$\Omega_e$ - accounting for void geometries and cell wall characteristics - it leads to the following governing equation [96]:

$$\int_{\Omega^\varepsilon} \left(\boldsymbol{\varepsilon}^0(\mathbf{v}) + \boldsymbol{\varepsilon}^1(\mathbf{v})\right)^T [\mathbf{E}] \left(\boldsymbol{\varepsilon}^{\overline{(\mathbf{v})}} + \boldsymbol{\varepsilon}^*(\mathbf{v})\right) \, d\Omega^\varepsilon = \int_{\Gamma_t} \mathbf{t}^T \mathbf{v} \, d\Gamma \tag{3.5}$$

where $[\mathbf{E}]$ represents the position-dependent local elasticity tensor within the RVE, $\boldsymbol{\varepsilon}^0(\mathbf{v})$ and $\boldsymbol{\varepsilon}^1(\mathbf{v})$ correspond to the virtual macroscopic and microscopic strains respectively, and $\mathbf{t}$ denotes the traction forces acting on boundary $\Gamma_t$. As a virtual displacement field, $\mathbf{v}$ can be selected to vary exclusively at the microscale while remaining constant macroscopically. This assumption leads to the microscopic equilibrium equation:

$$\int_{\Omega^\varepsilon} \left\{\varepsilon^1(v)\right\}^T [E] \left\{\bar{\varepsilon}(v)\right\} + \varepsilon^*(v) \, d\Omega^\varepsilon = 0 \tag{3.6}$$

$$\int_{V_{RVE}} \left\{\varepsilon^1(v)\right\}^T [E] \varepsilon^*(v) \, dV_{RVE} = - \int_{V_{RVE}} \left\{\varepsilon^1(v)\right\}^T [E] \bar{\varepsilon}(v) \, dV_{RVE} \tag{3.7}$$

### 3.2.1 Geometric Modelling of a Unit Cell

The unit cells in this study are based on six different TPMS structures: Gyroid, Diamond, Schwarz, Lidinoid, Neovius, and SplitP. The design space for the unit cell is defined as a cubic domain with dimensions $2 \times 2 \times 2\,\text{mm}$, ensuring a consistent reference length throughout all the structures. Each TPMS structure is modeled to occupy the entire unit cell volume, and the relative density is systematically controlled by adjusting the wall thickness while maintaining the unit cell dimensions. The geometric models were generated in `nTop` software using implicit surface equations specific to each TPMS type.

$$\textbf{Gyroid} \quad f(X,Y,Z) = \sin(X)\cos(Y) + \sin(Y)\cos(Z) + \sin(Z)\cos(X) \tag{3.8}$$

$$\textbf{Schwarz} \quad f(X,Y,Z) = \cos(X) + \cos(Y) + \cos(Z) \tag{3.9}$$

$$\textbf{Diamond} \quad f(X,Y,Z) = \cos(X)\cos(Y)\cos(Z) \tag{3.10}$$

**Neovius** $$f(X,Y,Z) = 3\left(\cos(X)+\cos(Y)+\cos(Z)\right) + 4\cos(X)\cos(Y)\cos(Z) \tag{3.11}$$

**SplitP** $$\begin{aligned} f(X,Y,Z) = 1.1\Big(&\sin(2X)\cos(Y)\sin(Z) + \sin(2Y)\cos(Z)\sin(X) \\ &+ \sin(2X)\cos(X)\sin(Y)\Big) \\ - 0.2\Big(&\cos(2X)\cos(2Y)\cos(2Z) + \cos(2Z)\cos(2X)\Big) \\ - 0.4&\left(\cos(2Y)+\cos(2Z)+\cos(2X)\right) \end{aligned} \tag{3.12}$$

**Lidinoid** $$\begin{aligned} f(X,Y,Z) = 0.5\Big(&\sin(2X)\cos(Y)\sin(Z) + \sin(2Y)\cos(Z)\sin(X) \\ &+ \sin(2Z)\cos(X)\sin(Y)\Big) \\ - 0.5\Big(&\cos(2X)\cos(2Y) + \cos(2Y)\cos(2Z) \\ &+ \cos(2Z)\cos(2X)\Big) \\ - &\cos(2X) + 0.15 \end{aligned} \tag{3.13}$$

Here, the coordinates $X$, $Y$, and $Z$ are defined as $\frac{2\pi n_i}{L_i}$, where $n_i$ represents the number of unit cells and $L_i$ denotes the cell size along the $i$-th dimension [34].

The relative density of a lattice structure is defined as the ratio of the volume occupied by the solid material to the total volume of the unit cell. To investigate the mechanical properties under varying porosity, five different relative densities are considered: 0.1, 0.2, 0.3, 0.4, and 0.5%. For each TPMS architecture, the relative density is modulated by altering the wall thickness, which directly influences the effective stiffness and strength of the structure. The relationship between thickness and relative density is highly dependent on the TPMS topology, as each structure exhibits distinct geometric characteristics. The material was Ti6Al4V, which is a widely used biocompatible material for biomedical implants. The mechanical properties are presented in Table 3.1.

The wall thickness required to achieve a specific relative density varies across different TPMS types due to their inherent geometric differences. An iterative process was performed to determine the precise thickness values corresponding to

each relative density. The results are summarized in Table 3.2, which lists the optimized thickness values for all six TPMS structures at the five relative density levels.

TABLE 3.1: Mechanical Properties of Ti6Al4V [97]

| **Properties** | **Units** | **Values** |
|---|---|---|
| Density | g/cc | 4.43 |
| Elastic modulus | GPa | 113.8 |
| Poisson's ratio | - | 0.342 |
| Conductivity | W/m/K | 6.7 |
| Specific heat | J/g/C | 0.5263 |

TABLE 3.2: Wall thickness (mm) corresponding to relative density (%) for each TPMS unit cell

| | **Relative Density (%)** | | | | |
|---|---|---|---|---|---|
| **Structure** | **0.1** | **0.2** | **0.3** | **0.4** | **0.5** |
| Gyroid | 0.11 | 0.21 | 0.31 | 0.42 | 0.52 |
| Diamond | 0.09 | 0.18 | 0.26 | 0.35 | 0.43 |
| SplitP | 0.08 | 0.155 | 0.23 | 0.31 | 0.385 |
| Neovius | 0.018 | 0.036 | 0.053 | 0.075 | 0.12 |
| Schwarz | 0.06 | 0.12 | 0.18 | 0.235 | 0.295 |
| Lidinoid | 0.055 | 0.105 | 0.16 | 0.235 | 0.32 |

### 3.2.2 Mesh Independence Study

A mesh independence study was performed on the Lidinoid TPMS structure to determine the optimal mesh density that ensures numerical accuracy while maintaining computational efficiency. The analysis was conducted using tetrahedral quadratic elements in `nTop` software, with the effective Young's modulus serving as the convergence criterion. The mesh was systematically refined, and results showed that increasing the element count from 698,272 to 876,673 cells produced only a 0.38% difference in the calculated Young's modulus as shown in Figure 3.3. Given this negligible improvement in accuracy, the mesh with 698,272 elements was selected for all subsequent simulations. This choice effectively balances computational cost with result precision, as further mesh refinement would impose

significantly longer solve times without providing meaningful gains in solution accuracy.

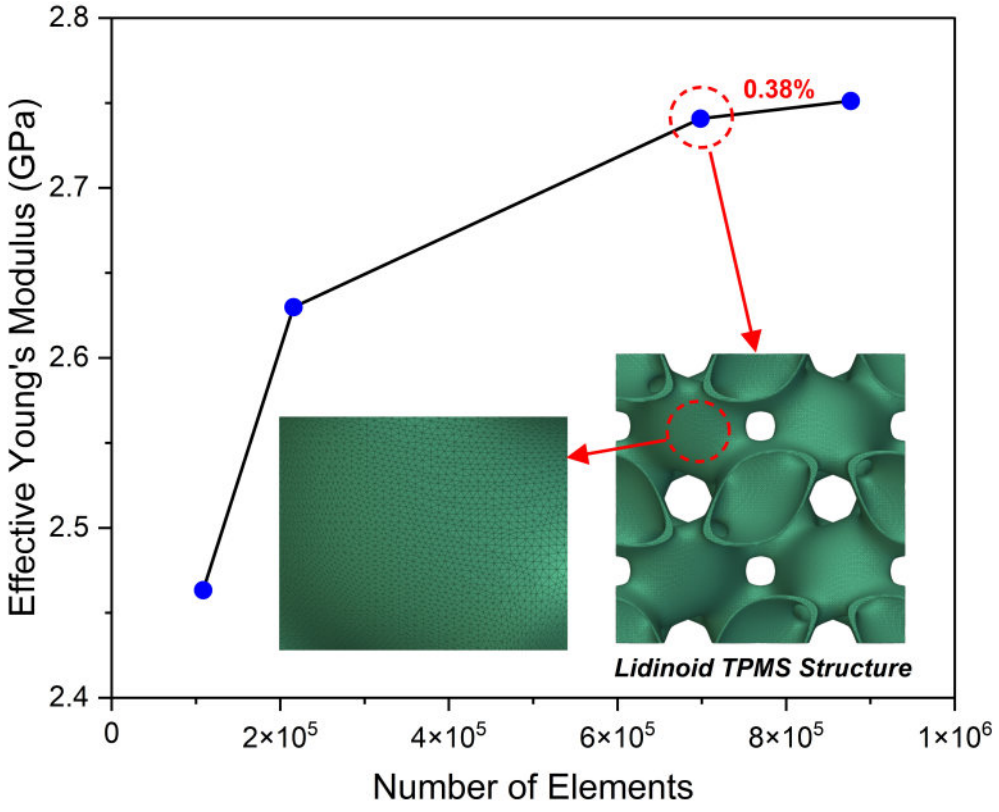


FIGURE 3.3: Mesh independence study for AH

### 3.2.3 Evaluating the Effective Young's Modulus of TPMS Structures

In this study, the effective Young's modulus of six different TPMS structures (Gyroid, Diamond, Lidinoid, Schwarz, Neovius, and SplitP) were analyzed through AH at five different relative density levels: 0.1, 0.2, 0.3, 0.4, and 0.5 %. The primary goal was to identify a scaffold configuration that closely mimics the mechanical behavior of the human lumbar vertebra, which typically exhibit a Young's modulus ranging between 10 and 15 GPa [98, 99], depending on anatomical location, age, and bone health. The results are visually represented through contours that display the spatial variation of effective Young's modulus within each unit cell as shown in Figure 3.4. The figure is divided into two categories, "Allowable

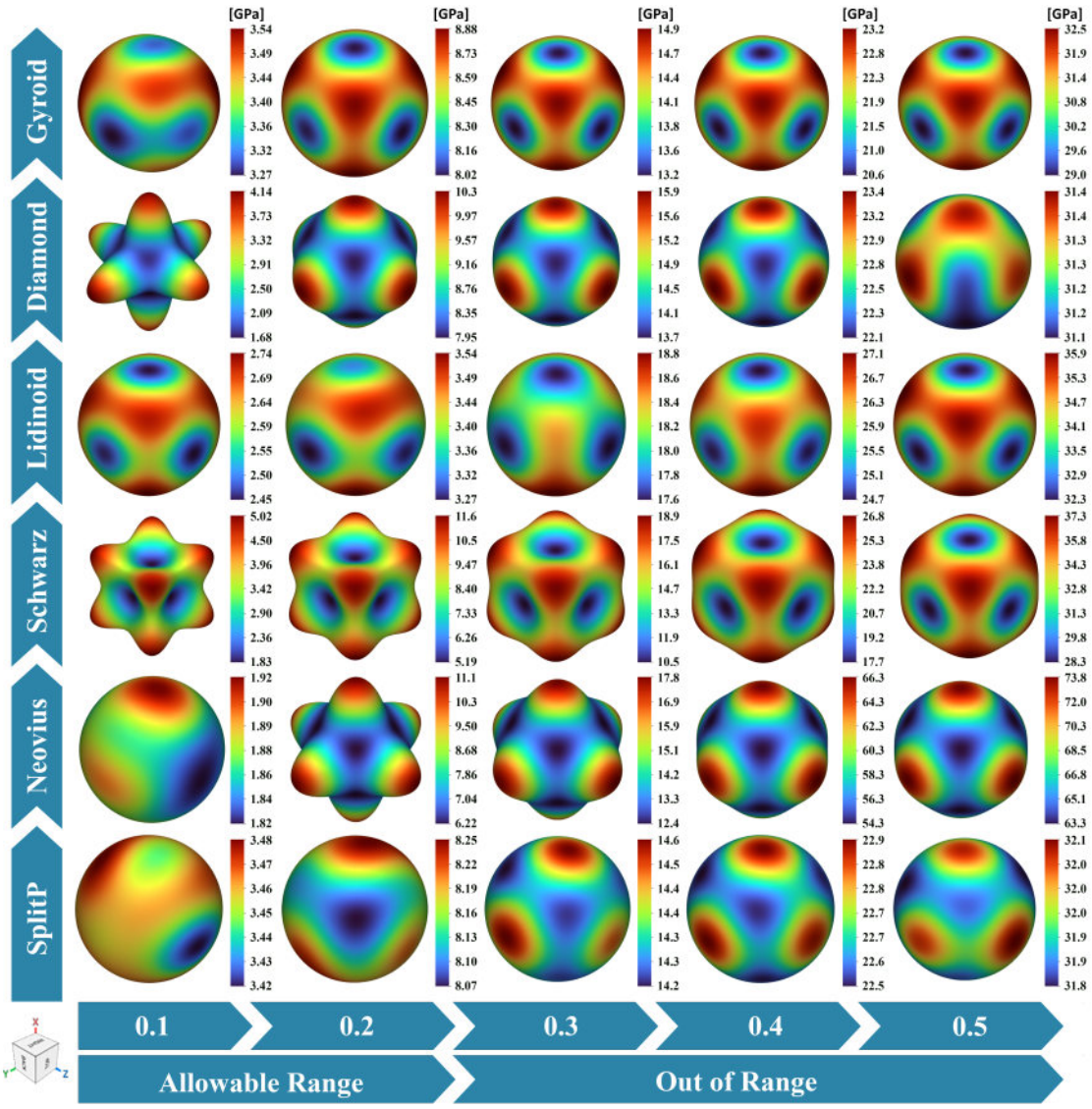


FIGURE 3.4: Effective Young's modulus (GPa) distribution of six TPMS structures (Gyroid, Diamond, Lidinoid, Schwarz, Neovius, and SplitP) across relative densities (0.1–0.5)

Range" and "Out of Range", based on whether the computed modulus falls within or beyond the acceptable range of the natural bone.

Among the simulated density levels, relative density 0.2 was identified as the most suitable configuration for mimicking the lumbar vertebral bone. The effective Young's modulus values for all six TPMS structures at this density range from approximately 3.27 to 11.6 GPa, placing them well within the physiological limits. The contour distributions at this density show a balance between structural complexity and mechanical functionality, with moderate stiffness values, while avoiding

the excessive red zones that indicate stress concentrations. For instance, the Gyroid and SplitP structures display relatively uniform stress fields, suggesting good mechanical distribution and stability, which is essential for load-bearing applications like spinal implants. Conversely, while the Schwarz and Neovius structures exhibit slightly higher stiffness values and localized peaks, they still fall within the acceptable range, making them viable candidates as well.

On the other hand, structures with higher relative densities (0.4 and 0.5) show significantly elevated stiffness values, with some exceeding 30 GPa, as indicated by their color bars and increasingly red-dominant contours. Such over-stiffness may lead to stress shielding, a detrimental effect where the implant absorbs most of the load, depriving the surrounding bone of necessary mechanical stimuli and potentially leading to bone resorption. Likewise, the lowest relative density (0.1) results in very low stiffness values, with some below 3 GPa, rendering them unsuitable for lumbar applications that demand a significant load-bearing capacity.

## 3.3 Geometric Modelling of L4-L5 Lumbar Segment

The 3D model of the L4-L5 lumbar segment was developed in SolidWorks 2024 using a parametric design approach based on anatomical references from morphometric studies [100, 101]. The key structural bodies of lumbar spine, including the vertebral bodies, pedicles, endplates, and intervertebral disc, were constructed using a combination of extruded sketches, lofted surfaces, and Boolean operations to ensure anatomical consistency. The drawing dimensions of L4-L5 vertebrae with its key components are illustrated in Figure 3.5. Minor refinements were applied to maintain proper articulation between components while adhering to biomechanically relevant proportions. The final model provides a representative geometry suitable for further computational analysis.

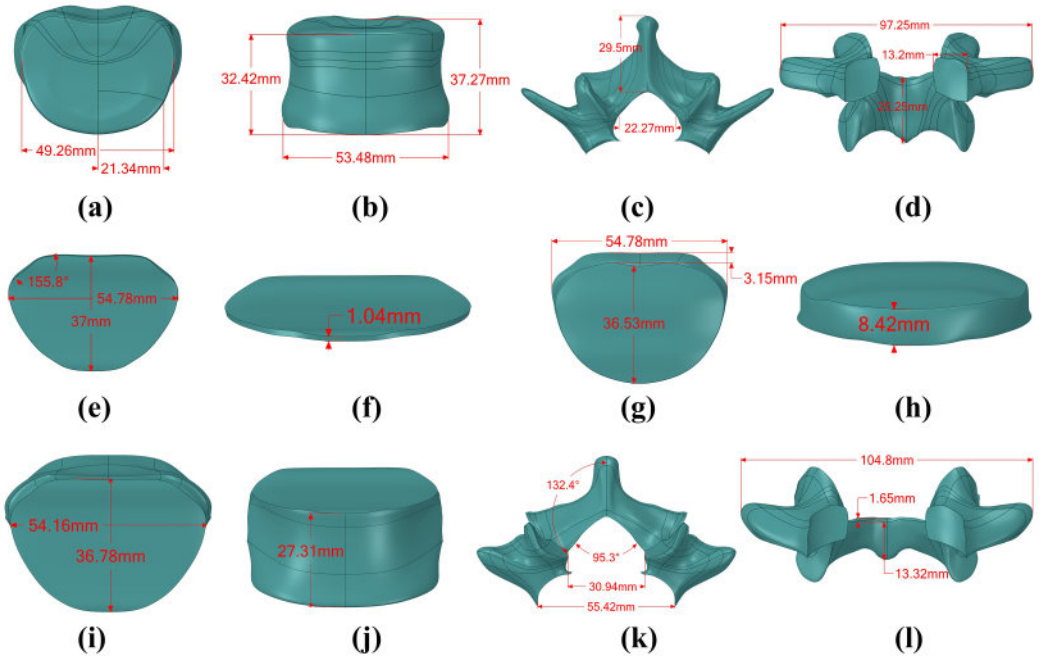


FIGURE 3.5: (a) L4 vertebral body (Top view) (b) L4 vertebral body (Front view) (c) L4 vertebral body support (Top view) (d) L4 vertebral body support (Front view) (e) Upper end plate (Top view) (f) Upper end plate (Front view) (g) IVD (Top view) (h) IVD (Front view) (i) L5 vertebral body (Top view) (j) L5 vertebral body (Front view) (k) L5 vertebral body support (Top view) (l) L5 vertebral body support (Front view)

### 3.3.1 Defining Regions of L4 Vertebral Body

After completing the CAD model of the L4-L5 segment in SolidWorks 2024, the geometry was imported into nTop (v5.20) and converted into an implicit body to enable advanced topology-based operations. The L4 vertebral body was then partitioned into distinct cortical and trabecular bone regions using a Boolean subtraction approach as shown in Figure 3.6. A uniform 0.5 mm inward-thickened shell was generated to represent the cortical layer, while the remaining interior volume was assigned as trabecular bone. The transition between regions was defined with a sharp interface to maintain anatomical fidelity. This implicit modeling workflow facilitated efficient region-specific material assignment for subsequent analysis.

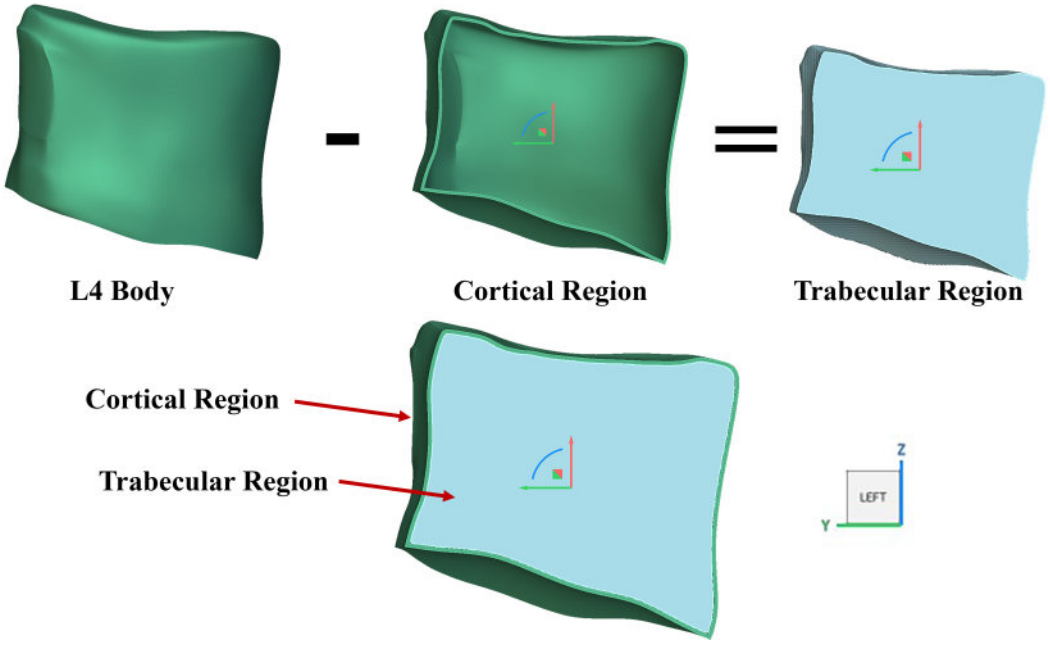


FIGURE 3.6: Splitting L4 vertebra into cortical and trabecular regions

### 3.3.2 Perforating Cortical Region of L4 Vertebral Body

To simulate the porous microstructure of cortical bone, a perforation pattern was applied to the L4 vertebral shell as shown in Figure 3.7. First, the implicit body was meshed to ensure uniform surface topology, with a maximum edge length tolerance of 0.1 mm. Next, 7,400 pseudo-randomly distributed points were generated on the cortical surface using spatial weighting and relaxation iterations (1,700 steps) to achieve an even distribution. At each point location, a cylindrical implicit body (diameter: 0.18 mm) was created normal to the surface. Finally, a Boolean subtraction operation was performed to perforate the cortical shell with these micro-scale holes, maintaining the porosity of 10%, replicating the natural porosity of bone ($< 30\%$ porosity).

### 3.3.3 Designing of Trabecular Region of L4 Vertebral Body

The trabecular bone architecture was developed through an implicit modeling approach. Beginning with the original geometry, a scaled-down duplicate (25% of original size) was created to enable precise control over microarchitectural features. A radial thickness distribution field was established using a ramp function,

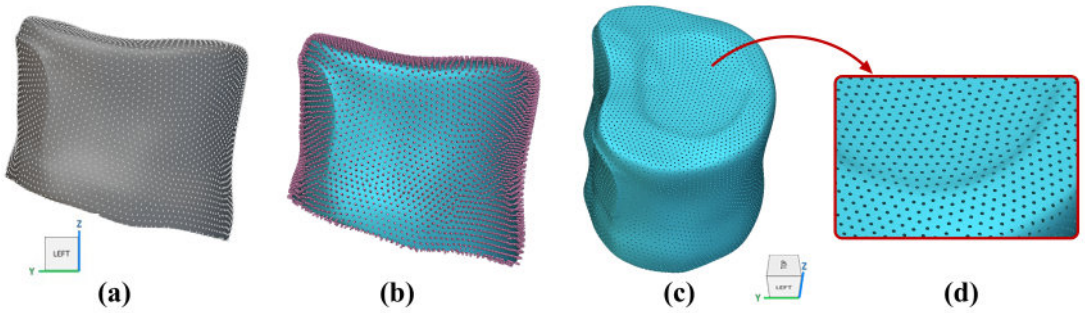


FIGURE 3.7: Cortical region with (a) Equally spaced points (b) Cylinders in place of points (c) Holes (d) Zoomed in view

with iterative refinements applied to achieve physiological accuracy. Through this process, a scaling factor of $y/0.7$ was identified as optimal for maintaining proper radial thickness gradients. Figure 3.8 illustrates the spatially varying pore size field applied to the trabecular region, demonstrating the radial density gradient from higher density (smaller pore size) near the cortical shell to increased pore size in the interior regions, matching physiological bone architecture.

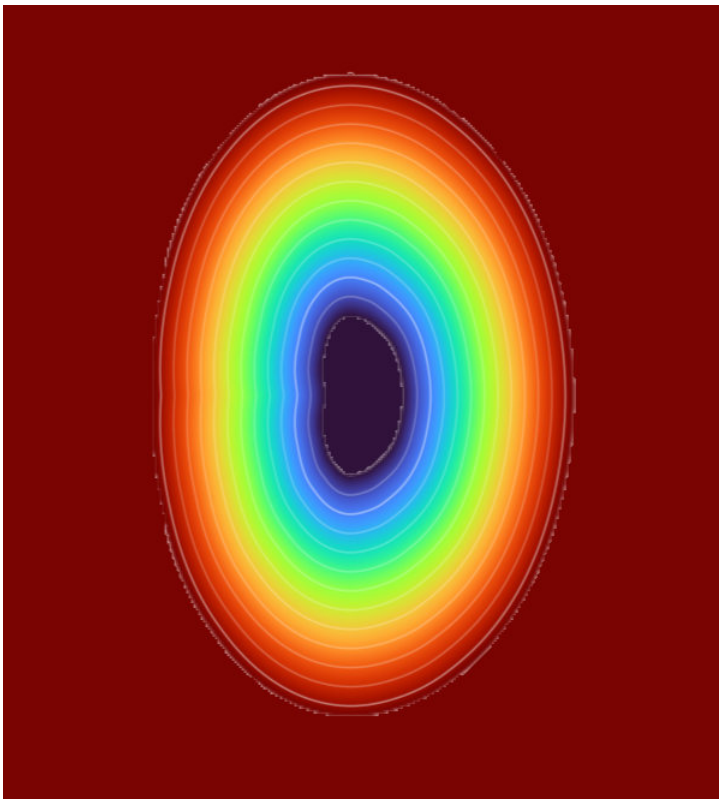

FIGURE 3.8: Pore size distribution field showing dense region near cortical bone (red, smaller pores) transitioning to porous trabecular zones (blue, larger pores), maintaining physiological bone architecture

For microarchitecture generation, six candidate TPMS structures were evaluated against biomechanical constraints. After rigorous iterations matching 80% porosity and maintaining pore sizes, shown in Table 3.3, within the natural bone range, only the Neovius and SplitP structures proved viable. Pore size analysis was performed using ImageJ by first importing the TPMS unit cell image and calibrating the spatial scale. Individual pores were isolated by converting images to 8-bit format and applying optimal thresholding. The Feret diameter (the longest distance between any two points along the pore boundary) was measured for each pore via particle analysis, providing a conservative estimate of maximum pore dimension. The remaining four TPMS configurations were eliminated as their geometric properties could not satisfy the minimum thickness requirements while maintaining the target porosity and pore size specifications.

TABLE 3.3: Shortlisted structures with their wall thickness and pore size

| **Structure** | **Starting wall thickness (Pore size)** | **Ending wall thickness (Pore size)** |
|---|---|---|
| SplitP | 0.38 mm (590 µm) | 0.505 mm (465 µm) |
| Neovius | 0.06 mm (840 µm) | 0.136 mm (465 µm) |

This selective approach ensured the trabecular architecture replicated both the mechanical properties and morphological characteristics of natural bone. The final design successfully captured the density gradient observed in physiological trabecular bone, with increased density near the cortical shell transitioning to greater porosity in the interior regions (trabecular bone) as shown in Figure 3.9.

Prior to FEA and CFD simulations, the selected SplitP and Neovius TPMS structures were exported from nTop as STL files. Due to the complex geometry of the lattice structures, an initially dense surface mesh was generated in nTop to avoid self-intersection errors inherent to low-resolution meshes. This resulted in large file sizes that were computationally prohibitive for analysis. To optimize the models, the STL files were processed in MeshLab, where mesh decimation was applied to strategically reduce the number of surface elements while preserving critical geometric features. This methodical approach preserved the structural integrity of the trabecular architecture while facilitating effective numerical simulation.

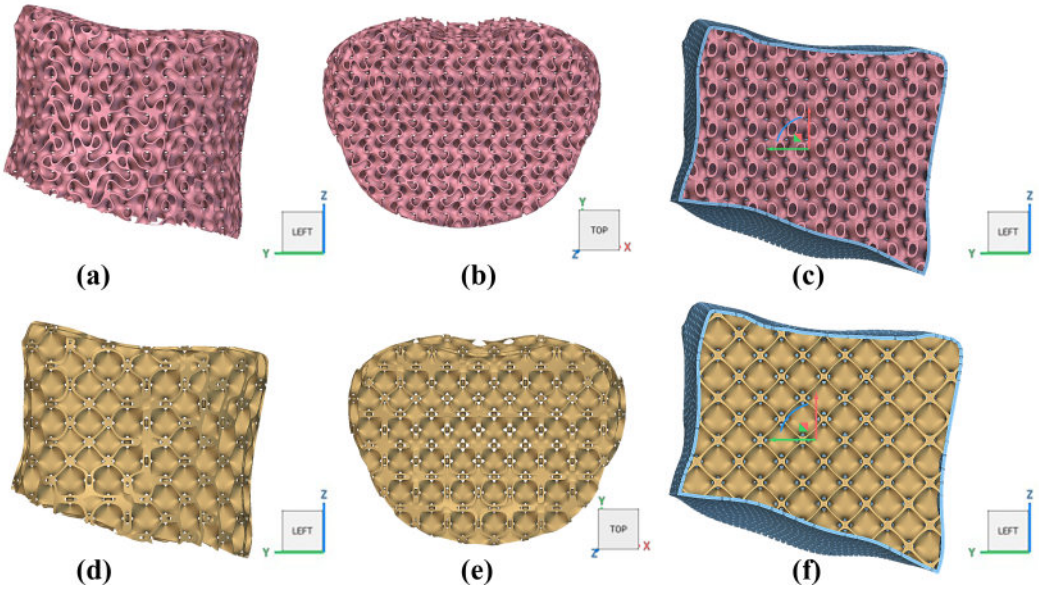


FIGURE 3.9: Trabecular bone with SplitP structure (a) Side view (b) Top view (c) Side view with cortical region, Trabecular bone with Neovius structure (a) Side view (b) Top view (c) Side view with cortical region

## 3.4 FEA Setup

### 3.4.1 Material Properties

The effective elastic modulus obtained from homogenization was assigned to the L4 vertebral body. The mechanical properties assigned for the FEA are summarized in Table 3.4.

TABLE 3.4: Material properties for FEA

| Materials | Elastic modulus (GPa) | Poisson's ratio |
|---|---|---|
| Vertebral body implant (SplitP) | 8.25 | 0.342 |
| Vertebral body implant (Neovius) | 11.1 | 0.342 |

### 3.4.2 Mesh Generation and Mesh Independence

For the FEA, mesh generation was initially performed using fTetWild software, which produced high-quality linear tetrahedral elements. Subsequently, Gmsh software was employed to convert the linear tetrahedral elements into quadratic

tetrahedral elements, enhancing the accuracy of the stress distribution results due to improved interpolation capabilities. The mesh generation is shown in Figure 3.10. A mesh independence study was conducted to validate the adequacy of

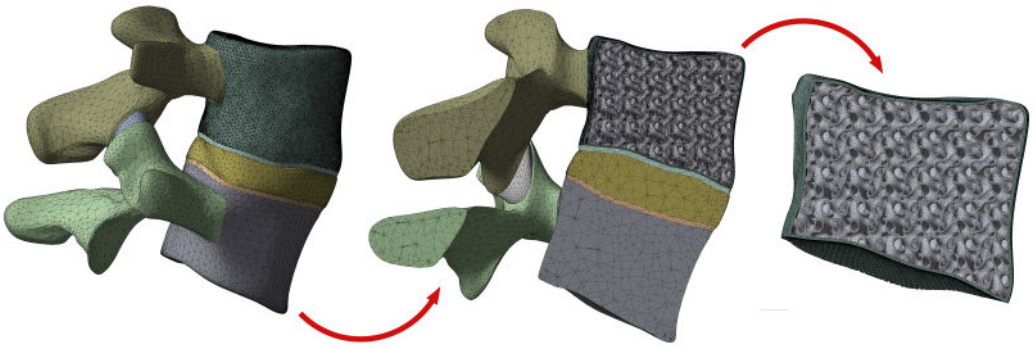

FIGURE 3.10: Mesh generation for FEA

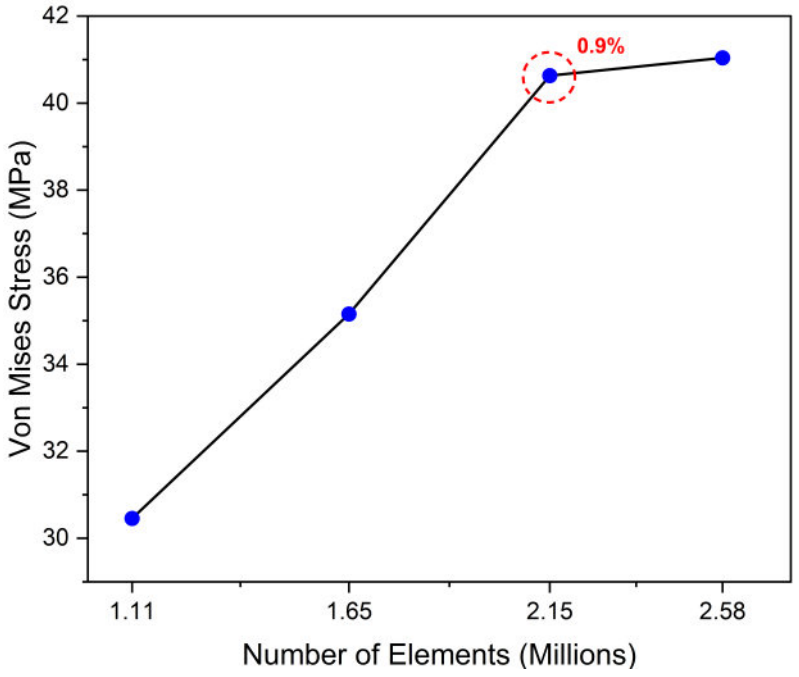


FIGURE 3.11: Mesh independence study for FEA

mesh density. Models with varying element counts, ranging from approximately 1.11 million to 2.58 million elements, were analyzed, with the von Mises stress serving as the convergence metric. As shown in the Figure 3.11, the stress values stabilized with a marginal difference of 0.9% between the final two mesh densities, indicating mesh convergence. Based on this, the mesh with approximately 2.15 million elements was selected for subsequent simulations to balance accuracy and computational efficiency.

### 3.4.3 Boundary Conditions

The study utilized Ansys Workbench 2025 to define boundary and loading conditions for the simulation of spinal motion. The L5 vertebral body was modeled as a fixed boundary, with its substructure constrained to prevent displacement and rotational degrees of freedom in all directions. To replicate physiological loading scenarios including flexion, extension, lateral bending, and torsion, a uniformly distributed 400-N force combined with a 10-Nm moment was applied to the superior surface of the L4 vertebra [102, 103]. The boundary conditions are shown in Figure 3.12.

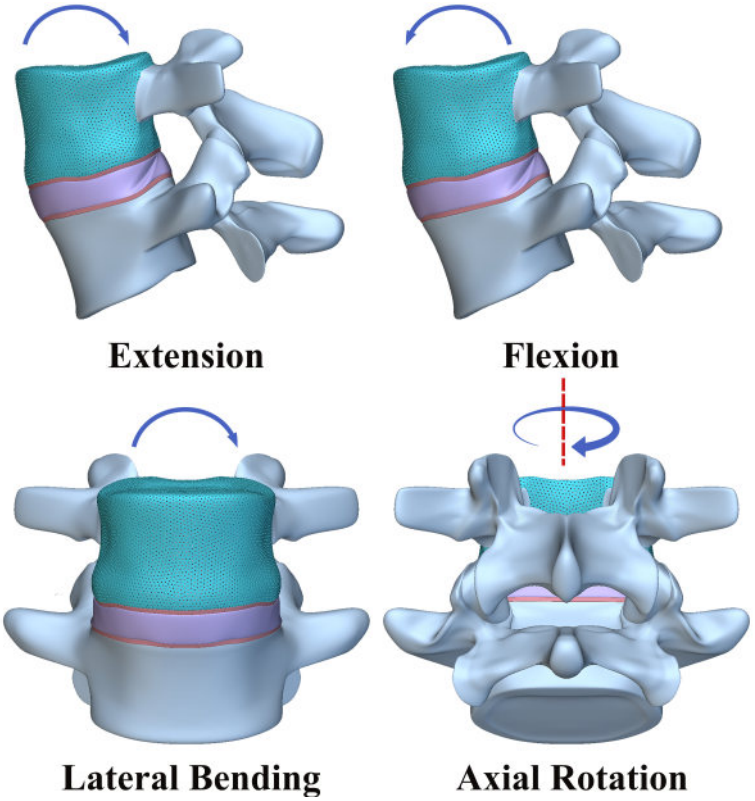


FIGURE 3.12: Boundary conditions on L4-L5 vertebrae

### 3.4.4 Validation Study

To validate the accuracy of the developed finite element model, the range of motion (ROM) of the L4–L5 vertebral segment under flexion loading was compared with published results by Shang et al. [104], who performed similar simulations using a

validated lumbar spine model. A 400 N compressive preload and 10 Nm moment were applied to the superior surface of L4, while the inferior surface of L5 was fully constrained, following the same boundary conditions. The ROM result from the

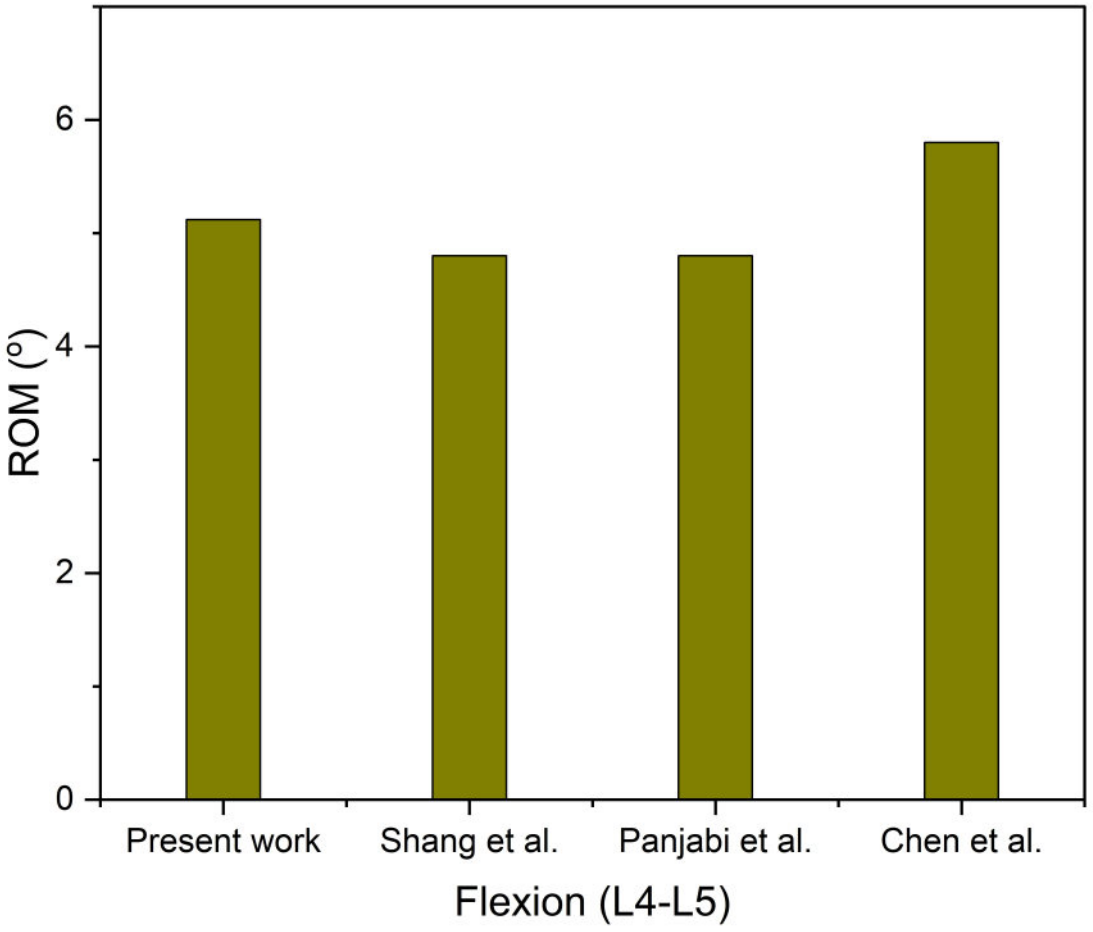


FIGURE 3.13: Validation study for FEA

current study for L4–L5 in flexion closely matched the values reported by Shang et al.[104] with minimal deviation, thereby supporting the validity of the model. Figure 3.13 includes both our result and the referenced data from the literature for direct comparison. This strong correlation demonstrates that the developed model can accurately capture physiological spinal motion under flexion, and can be reliably used for further biomechanical analysis of vertebral implants at the L4–L5 level.

## 3.5 CFD Setup

For an incompressible fluid with steady flow and constant density, the Navier-Stokes equation was applied as follows:

$$\rho\frac{\partial \mathbf{u}}{\partial t} - \mu\nabla^2\mathbf{u} + \rho(\mathbf{u}\cdot\nabla)\mathbf{u} + \nabla p = \mathbf{F} \tag{3.14}$$

$$\nabla\cdot\mathbf{u} = 0 \tag{3.15}$$

Here, $\rho$, $\mathbf{u}$, $\mu$, $\nabla$, $p$, and $\mathbf{F}$ denote the fluid density (kg/m$^3$), velocity (m/s), dynamic viscosity (kg/m·s), del operator, pressure (Pa), and external forces (such as gravity or centrifugal force), respectively. In this case, $\mathbf{F}$ is assumed to be zero [81, 105].

Blood was used as a fluid. The density of blood was 1050 kg/m$^3$ [106]. The viscosity of blood was 0.004 kg/m.s as it is assumed to be a Newtonian fluid [107]. The permeability $k_0$ of the models in the Newtonian case was determined using the classical Darcy's equation [108]:

$$k_0 = \frac{u\mu L}{\Delta p} \tag{3.16}$$

where $L$ is the length of the model (m) and $\Delta p$ is the pressure drop (Pa).

In the case, where blood is considered a non-Newtonian fluid, the viscosity of blood was calculated using the power law model [109]:

$$\mu = K\gamma^{n-1}\mu_{\min} < \mu < \mu_{\max} \tag{3.17}$$

where $K$ indicates the consistency index, $\gamma$ (s$^{-1}$) is the shear rate, and $n$ is the power law exponent. For Newtonian fluid, $n = 1$, for shear thickening fluid $n > 1$, and for shear thinning fluid $n < 1$. The values of $K$ and $n$ are 0.017 (kg-s$^{-1}$n-2/m) and 0.708, respectively. The $\mu_{\min}$ and $\mu_{\max}$ are the minimum and maximum viscosity cutoffs, with values of 0.001 and 0.1 kg/m-s, respectively. The power law model was adopted for its demonstrated effectiveness in capturing the rheological

properties of non-Newtonian fluids in TPMS structure analyses. This model provides particularly accurate characterization of shear-thinning behavior and shear-thickening behavior [109–111].

The permeability for non-Newtonian fluid can be calculated using the modified equation by Morais et al. [112]:

$$k = uK\left(\frac{L}{\Delta p}\right)^{\frac{1}{n}} \tag{3.18}$$

In a laminar flow system, the wall shear stress ($\tau_\omega$) is defined as the product of dynamic viscosity ($\mu$) and the normal velocity gradient at the wall [113]:

$$\tau_\omega = \mu\frac{\partial u}{\partial m} \tag{3.19}$$

where $m$ denotes the $x$, $y$, and $z$ direction.

The Reynolds number ($Re$) can be calculated using this formula [84]:

$$Re = \frac{\rho u L}{\mu_a} \tag{3.20}$$

where $\mu_a$ is the fluid viscosity.

When bone is fractured, it disrupts the highly vascularized tissue, tearing blood vessels across the fracture line. As a result, blood flows from the damaged vessels into the gap between the fractured bone ends [114–116]. This indicates that in the initial stage of scaffold implantation, blood flow diffuses into the scaffold's pores. Therefore, incorporating the properties of blood into the CFD analysis in scaffolds is likely to yield more realistic results. While modeling blood as a Newtonian fluid with constant viscosity simplifies the parametric study of its behavior [117, 118], it is important to note that components such as cells, proteins, lipoproteins, and ions contribute to blood's non-Newtonian behavior [119]. Therefore, simulations are performed for both blood treated as a Newtonian and non-Newtonian fluid.

### 3.5.1 Mesh Generation and Mesh Independence

To ensure robustness in handling errors or defects while maintaining simulation stability, especially critical for complex geometries like TPMS structures, a fault-tolerant meshing approach was adopted. The PolyHexCore mesh type was utilized, featuring polyhedral cells in the core region and hexahedral cells near the boundaries as illustrated in Figure 3.14. This hybrid method effectively captures the flow with high accuracy while optimizing computational efficiency, making it well-suited for complex geometries. A uniform meshing strategy was applied across all

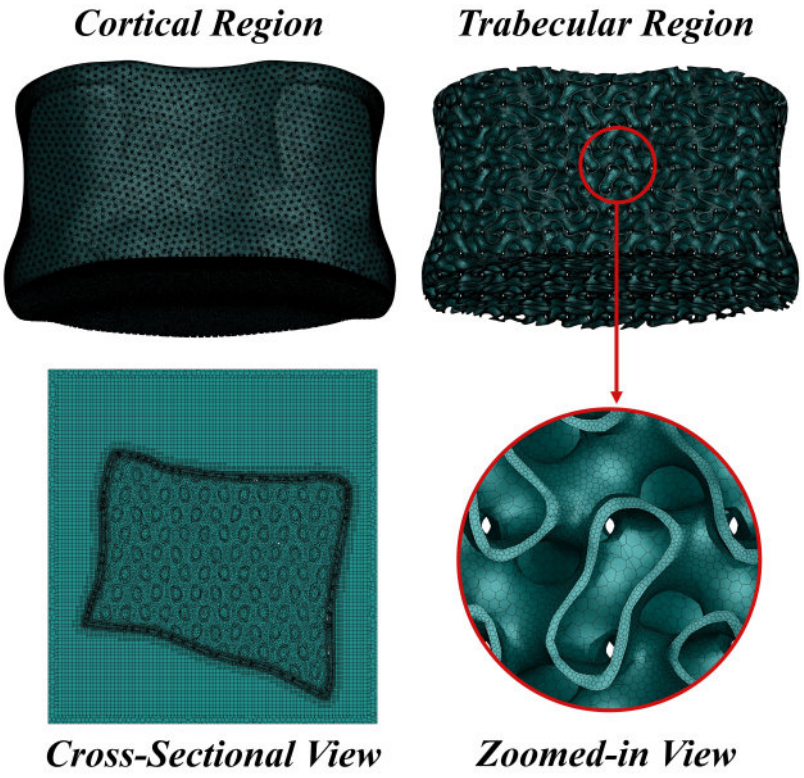


FIGURE 3.14: Mesh generation on cortical and trabecular region of L4 vertebra

cases, with mesh density adjustments made only during convergence testing. WSS was used as a key metric to evaluate mesh independence. After testing, a 12.49 million-cell mesh was selected as the optimal balance between accuracy and computational expense. The difference in WSS between this mesh and a finer 12.68 million-cell mesh was minimal (only 0.29%), confirming that the chosen resolution was sufficient for reliable results as presented in Figure 3.15.

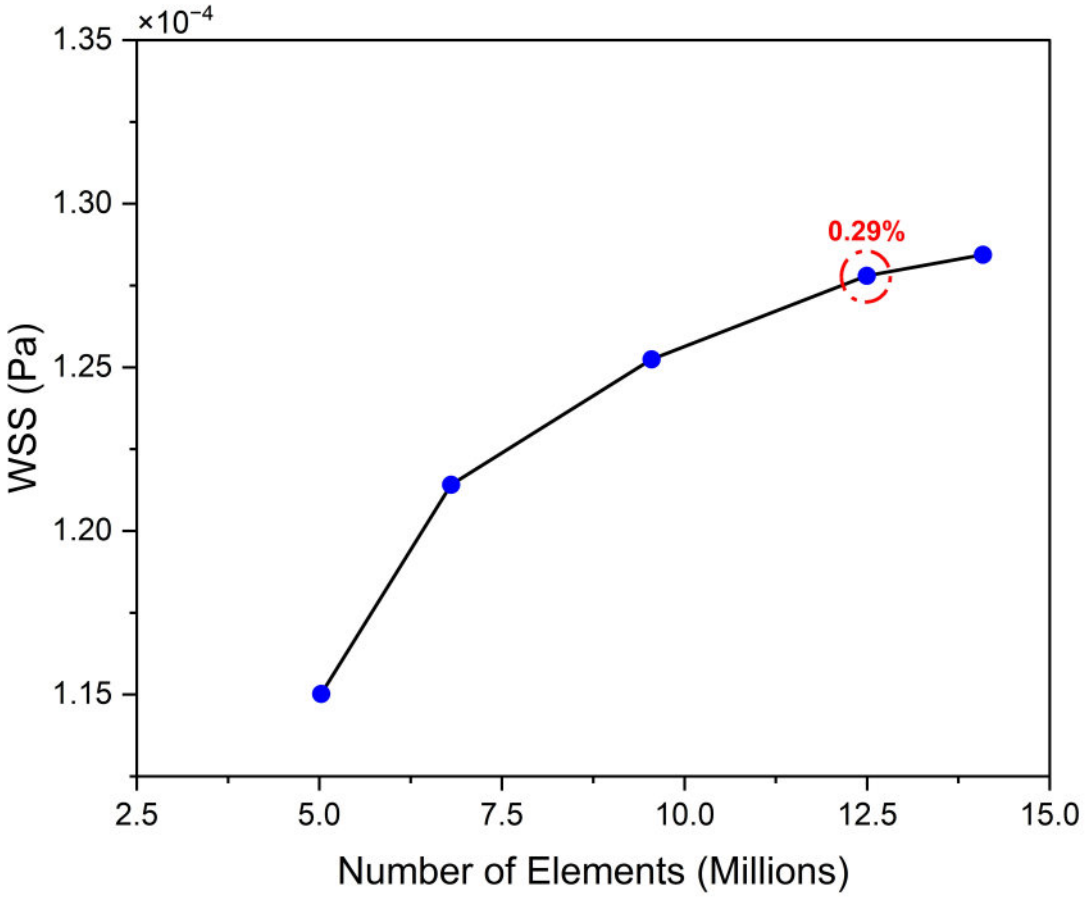


FIGURE 3.15: Mesh independence for CFD analysis

### 3.5.2 Boundary Conditions

Our CFD models incorporated four inlet velocities (0.5, 0.6, 0.7, and 0.8 mm/s) to encompass this physiological range reported in literature for blood flow in a human body. The simulations implemented no-slip conditions at scaffold walls and zero-gauge pressure at outlets [120, 121]. CFD simulation was conducted on two TPMS-based porous L4 bodies (Neovius and SplitP architectures), assuming rigid scaffold behavior (metallic scaffold-Ti6Al4V [122]) to justify neglecting fluid-structure interactions in these preliminary flow studies.

### 3.5.3 Numerical Schemes

This study utilized the Finite Volume Method (FVM) as the numerical framework to simulate blood flow through scaffold structures. The governing equations were

solved using a coupled scheme that simultaneously computes momentum and continuity equations, significantly improving convergence stability and computational efficiency, particularly crucial for modeling flow interactions within the complex geometries of TPMS scaffolds. For spatial discretization, gradient calculations employed the Green-Gauss Node-Based method, selected for its demonstrated accuracy in handling unstructured meshes. Pressure interpolation was performed using a second-order scheme to precisely resolve pressure variations throughout the flow domain. While higher-order schemes offer greater accuracy, momentum equations were discretized using a first-order upwind scheme to ensure solution robustness during initial iterations and in regions with steep gradients or complex flow patterns [81, 84]. This carefully balanced combination of numerical schemes was implemented to maintain computational efficiency while achieving solution accuracy, thereby ensuring reliable analysis of blood flow behavior within the porous L4 body.

### 3.5.4 Validation Study

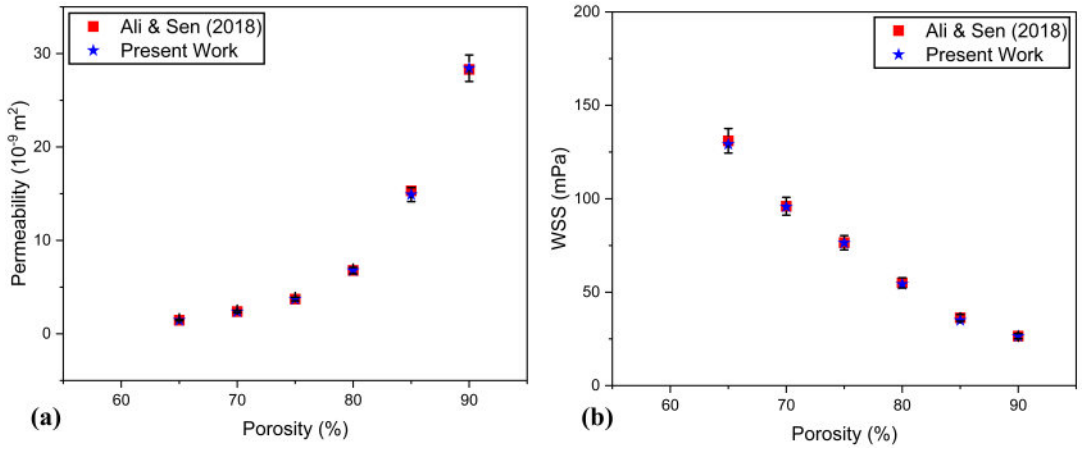


FIGURE 3.16: Validation study for CFD (a) Permeability (b) WSS

The CFD model was validated by replicating the gyroid TPMS geometry and flow conditions reported by Ali and Sen [123] under Newtonian fluid assumptions. The simulation was performed using the same boundary conditions and inlet velocity, and the results showed close agreement with the reference data, with a maximum deviation of 2.61% in permeability and 3.86% in WSS as shown in Figure 3.16.

Additionally, the methodology applied in this study is consistent with that employed in two of our previously published works [124, 125], further supporting the reliability and validity of the CFD setup and post-processing approach used for analyzing fluid flow in TPMS structures.

# Chapter 4

# Results and Discussion

## 4.1 Finite Element Analysis of L4 Vertebrae

### 4.1.1 Total Deformation on L4 Vertebrae

Under a combined axial load of 400 N and a 10 N·m moment, the results from our finite-element simulations reveal that the SplitP-based vertebral implant consistently exhibits higher displacement compared to the Neovius-based implant under all loading scenarios (flexion, extension, lateral bending, and axial rotation) as shown in Figure 4.1 and 4.2. The greatest displacement was observed during flexion, where the SplitP implant deformed by 0.047 mm, compared to the 0.03 mm deformation observed in the Neovius implant. These displacements are well below the clinically critical threshold of 0.10 mm, beyond which fibrous tissue may form instead of bone ingrowth [126]. Hence, either lattice restores vertebral height without exceeding the physiological envelope of motion.

The disparity in displacement between the two implants is primarily attributed to their distinct geometric designs. The SplitP implant, being composed of continuous, curved sheets, deforms more readily under load compared to the Neovius implant, which contains pillar-like junctions that provide higher resistance to bending. The flexibility of the SplitP implant thus facilitates superior load-sharing

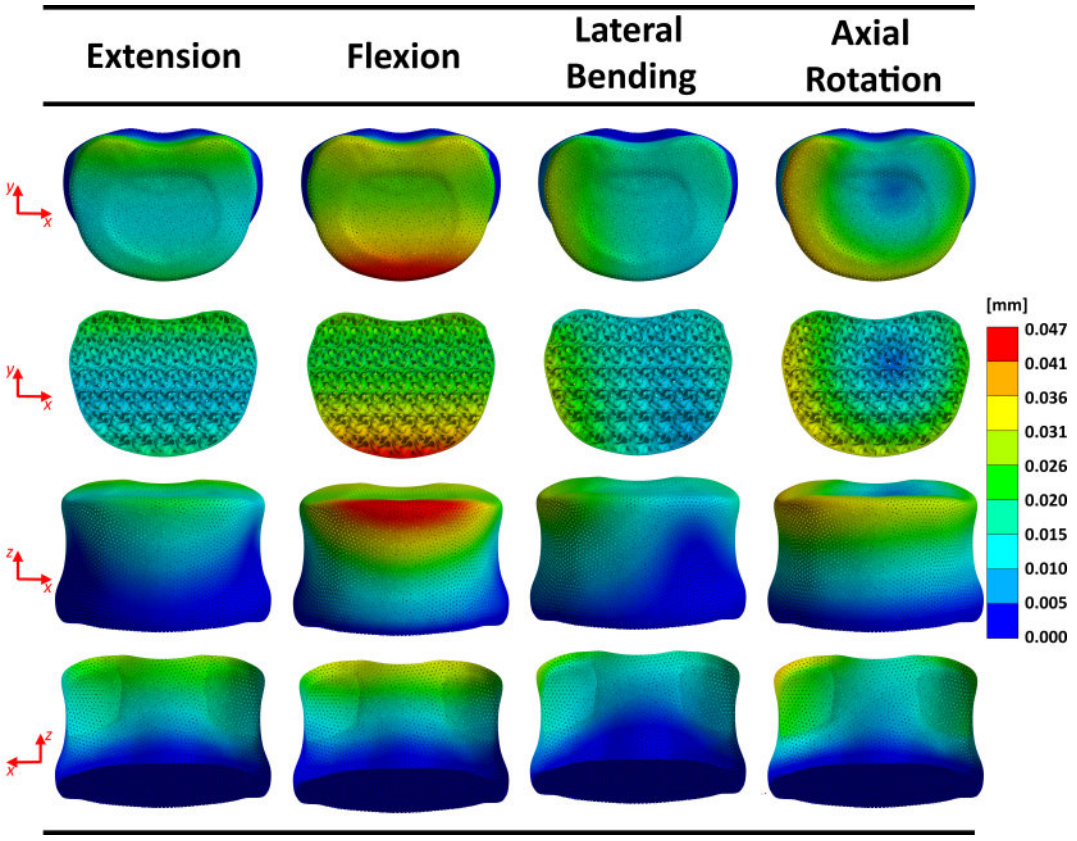


FIGURE 4.1: Total deformation in SplitP based implant under different loading conditions (Extension, Flexion, Lateral bending and Axial rotation)

with the surrounding trabecular bone, reducing the risk of stress shielding, a phenomenon known to cause bone resorption and weakening adjacent to rigid implants.

The stress shielding effect is a significant concern when designing vertebral implants, as implants that are too stiff tend to shield the surrounding bone from the mechanical forces it would normally experience. In this study, the Neovius implant, with its stiffer lattice structure, diverts more of the applied load away from the surrounding bone compared to the SplitP implant. This results in lower strain energy transferred to the bone, thus increasing the risk of stress shielding. Conversely, the SplitP implant, by being more flexible, maintains a more uniform load transfer and induces higher strain in the adjacent bone, which is critical for bone remodelling and maintaining bone density. The results align with the literature, where lower-modulus implants are shown to better preserve bone mass by maintaining physiological micro-strains necessary for bone health [127–129].

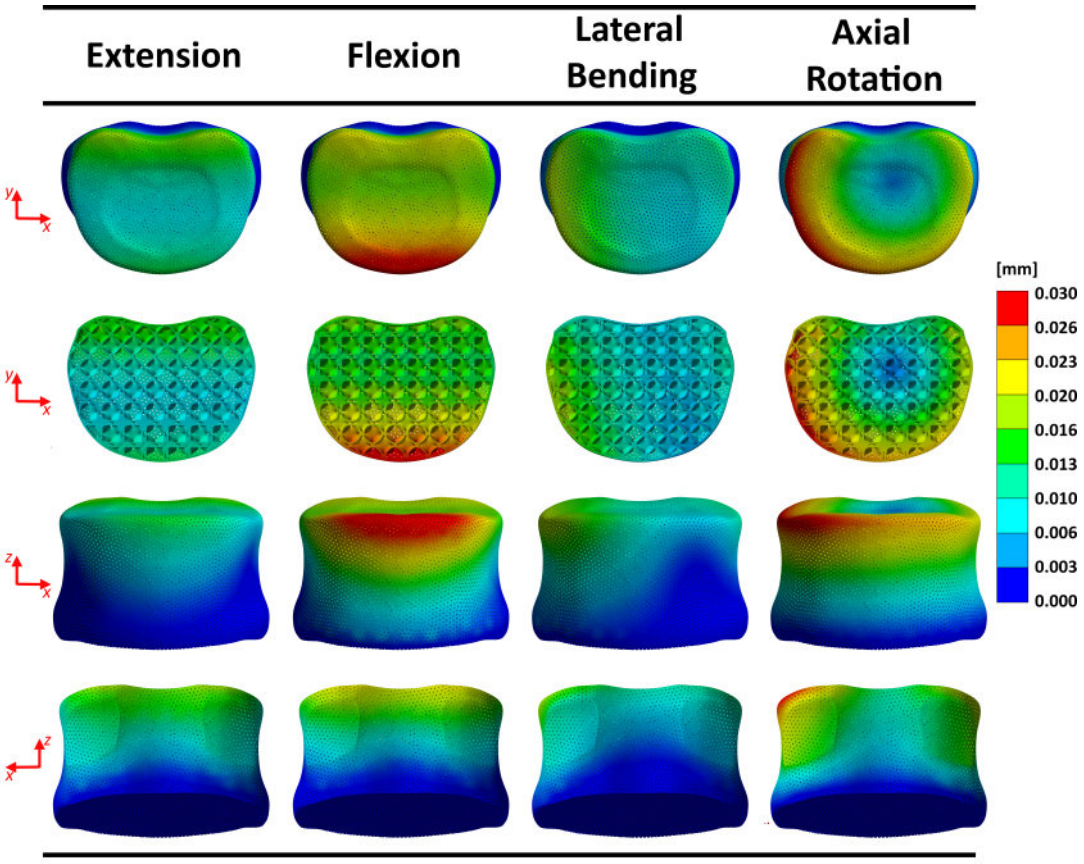


FIGURE 4.2: Total deformation in Neovius based implant under different loading conditions (Extension, Flexion, Lateral bending and Axial rotation)

In terms of biomechanical stability, both implants show adequate performance in resisting subsidence, with SplitP exhibiting a broader load path that reduces peak interface pressures as compared to Neovius. These findings are in line with literature studies on TPMS, where the broader load-bearing structure of TPMS-based designs was shown to mitigate the risk of implant migration or settling into osteoporotic bone [104]. Furthermore, successful osseointegration is a critical factor in the long-term success of spinal implants. The SplitP-based implant excels in this area, due to its higher compliance, which promotes mechanical stimulation of the surrounding bone, aiding in bone ingrowth. The Neovius-based implant, while offering superior initial stiffness, may face challenges in this regard unless surface modifications, such as texturing or coating with bioactive materials, are used to enhance osteointegration. At the end, this study demonstrates that both the SplitP-based vertebral implant and Neovius-based vertebral implant meet the mechanical requirements for successful VCF treatment. However, the SplitP-based

implant offers additional benefits in terms of load sharing, stress shielding prevention, and osseointegration potential, making it particularly suitable for patients where long-term bone health and remodelling are critical. On the other hand, the Neovius-based implant, with its higher initial rigidity, may be more appropriate for cases where immediate mechanical support is required to stabilize the vertebra in extremely osteoporotic bone.

### 4.1.2 Von Mises Stress on L4 Vertebrae

The von Mises stress is a critical parameter, particularly for understanding the yield behavior and overall mechanical performance of an implant. In this analysis, the von Mises stress was calculated for the SplitP-based vertebral implant and the Neovius-based vertebral implant under a 400 N axial compressive load and a 10 N·m moment. In Figure 4.3 and 4.4, it is clear that the SplitP-based vertebral implant experiences a maximum von Mises stress of 22 MPa, while the Neovius-based vertebral implant reaches a maximum von Mises stress of 20 MPa. These values are well within the yield strength of Ti-6Al-4V and the endurance limit, indicating that both implants are far from reaching their failure threshold under the applied loading conditions.

The relatively low von Mises stress in both implants is beneficial from a material safety perspective, suggesting that both implants will perform well under long-term, repeated loading cycles without risk of material failure. The SplitP implant's higher stress (22 MPa) compared to Neovius (20 MPa) reflects the differences in their structural design and load transfer characteristics.

The SplitP-based implant experiences a maximum von Mises stress of 22 MPa, which is slightly higher than the Neovius implant's maximum stress of 20 MPa. In Figure 4.3, it is clear that the stress distribution in the SplitP implant is more uniform across the surface, with only minor localized concentrations near areas of geometric transition. This uniform stress distribution occurs due to the continuous sheet-like geometry of the SplitP implant. The continuous and smooth surface of

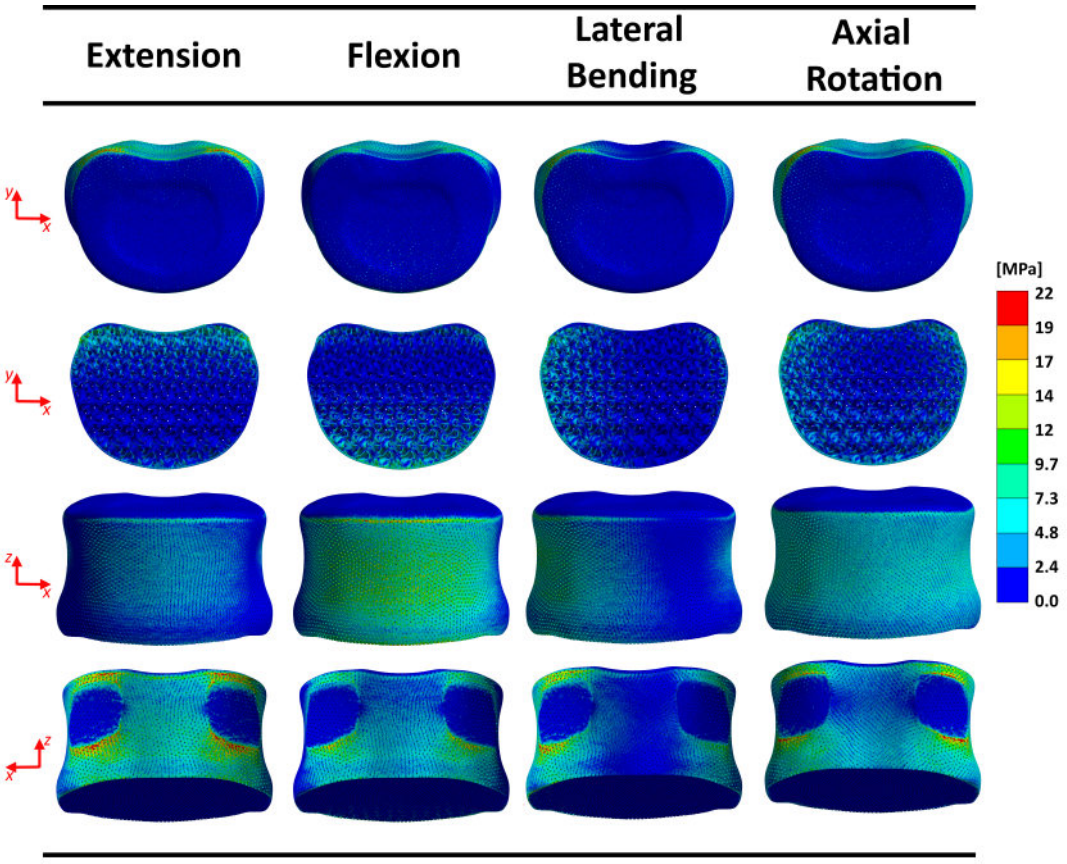


FIGURE 4.3: Von Mises Stress in SplitP based implant under different loading conditions (Extension, Flexion, Lateral bending and Axial rotation)

the SplitP implant, characteristic of its TPMS structure, allows forces to be distributed across a wider area. Because the material is uniformly loaded over the entire geometry, the stress is distributed more evenly, avoiding excessive concentration at any single point. The 22 MPa stress represents the maximum stress observed at regions with minor geometric irregularities or local surface curvatures, but it remains well below the material's failure limit.

On the other hand, the Neovius-based implant shows a maximum von Mises stress of 20 MPa as shown in Figure 4.4. Despite the slightly lower peak stress, the Neovius implant's stress distribution is not as uniform as that of SplitP. The Neovius design, characterized by a network of interconnecting pillars, exhibits higher stress concentrations at the points where the pillars intersect and form joints. These regions experience local stress concentration due to the rigid, pillar-like elements that do not allow for as much load distribution as in the SplitP design. This localized stress around the pillar junctions can create areas of stress

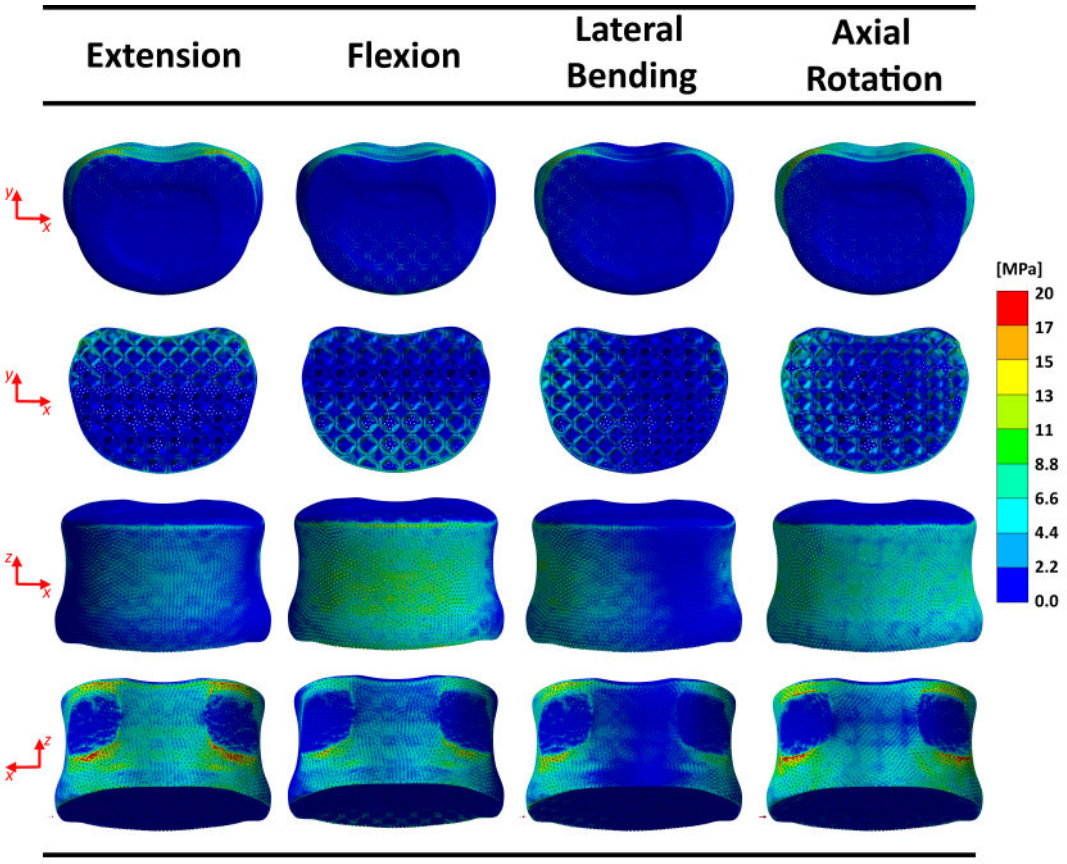


FIGURE 4.4: Von Mises Stress in Neovius based implant under different loading conditions (Extension, Flexion, Lateral bending and Axial rotation)

concentration, which could potentially lead to fatigue failure if subjected to long-term cyclic loading. However, the overall peak stress of 20 MPa in Neovius is still within safe limits and lower than the 22 MPa observed in SplitP.

Both implants exhibit low von Mises stress values, well within the material limits of Ti-6Al-4V, ensuring that neither implant will experience yielding under normal loading conditions. The higher stress in the SplitP implant (22 MPa vs. 20 MPa in Neovius) indicates that, while the SplitP implant has a slightly higher stress magnitude, it also benefits from a more evenly distributed stress profile. This even distribution reduces the risk of localized fatigue failure, which can be a concern in designs where stress is concentrated in small regions. The Neovius implant, despite having a lower peak stress, presents higher localized stress concentrations at the pillar junctions. Over time, if subjected to cyclic loading, these concentrations could contribute to material fatigue and crack initiation at those localized stress points.

## 4.2 Computational Fluid Dynamics of L4 Vertebrae

### 4.2.1 Newtonian Fluid Flow- Fluidic Characteristics

The CFD analysis for Newtonian fluid flow (constant viscosity fluid) was conducted on two TPMS scaffold designs, Neovius and SplitP, intended for use as vertebral body implants, specifically targeting the L4-L5 region. The analysis evaluated the fluidic performance by measuring pressure drop across the scaffolds at various inlet velocities (0.5, 0.6, 0.7, and 0.8 mm/s) and examining velocity distribution contours within the structures. These fluidic properties directly influence nutrient and oxygen transport, cell viability, differentiation, and ultimately the success of scaffold integration within bone tissue.

The results of the CFD simulations showed clear and consistent trends for pressure drop, increasing linearly with an increase in fluid velocity. For the Neovius scaffold, the pressure drops recorded at velocities of 0.5, 0.6, 0.7, and 0.8 mm/s were 0.02277 Pa, 0.02758 Pa, 0.03249 Pa, and 0.03749 Pa, respectively. Similarly, the SplitP scaffold displayed nearly identical values of 0.02276 Pa, 0.02757 Pa, 0.03247 Pa, and 0.03747 Pa at corresponding velocities. The negligible difference between the two scaffold types demonstrates their comparable pore geometries and internal architecture. These trends are consistent with Darcy's law, which predicts a linear relationship between fluid velocity and pressure drop within porous media under laminar flow conditions [121]. The pressure contours for SplitP and Neovius are shown in Figure 4.5 and 4.6.

Previous literature has reported that small and linearly proportional pressure gradients in bone scaffold structures indicate well-balanced pore architecture, optimal for physiological applications [130, 131]. A gradual increase in pressure drop with velocity is expected, as higher velocities exert increased viscous forces against the scaffold's internal surfaces, enhancing fluid resistance [81, 84]. Importantly, the minimal pressure drops recorded here suggest that both scaffold designs can effectively facilitate nutrient and oxygen transport under physiologically relevant

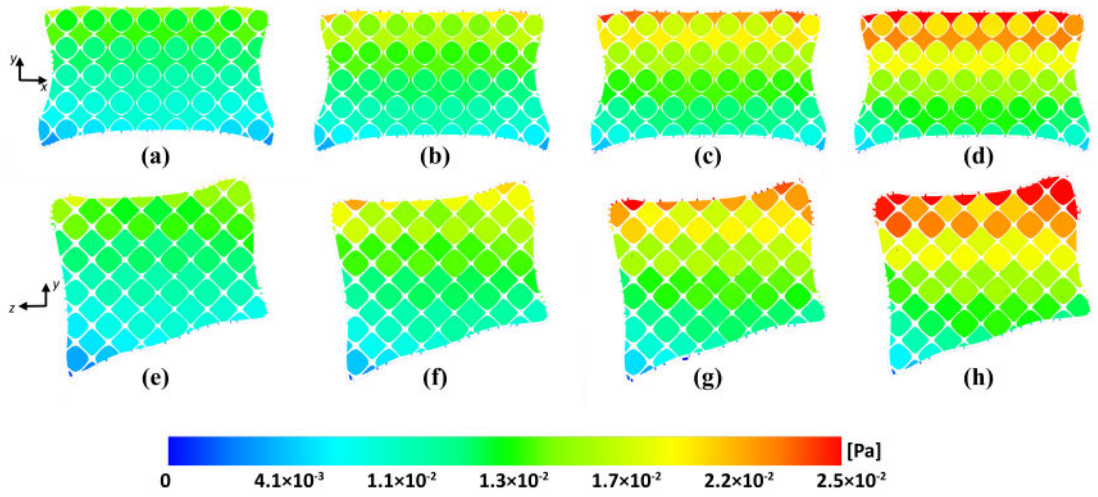


FIGURE 4.5: Pressure contours of Newtonian fluid flow for Neovius structure at different velocities at xy-axis (a) 0.5 mm/s (b) 0.6 mm/s (c) 0.7 mm/s (d) 0.8 mm/s, at yz-axis (e) 0.5 mm/s (f) 0.6 mm/s (g) 0.7 mm/s (h) 0.8 mm/s

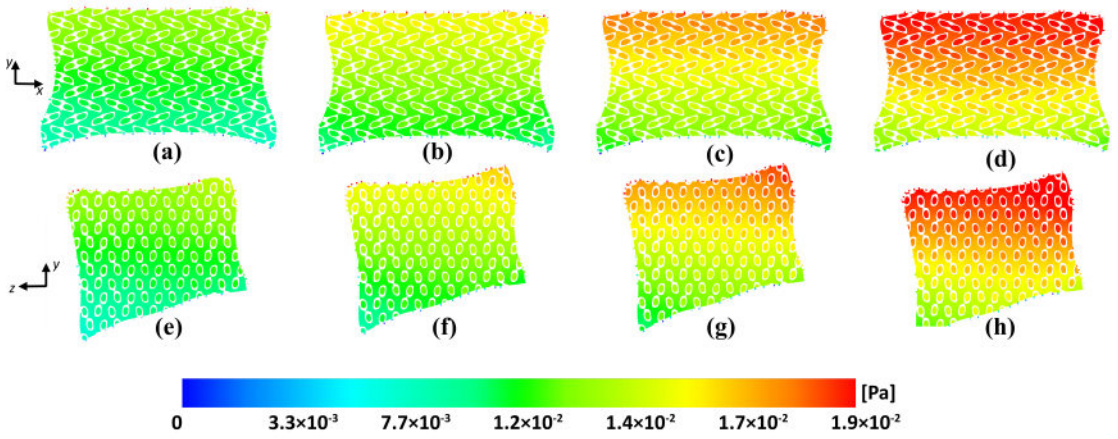


FIGURE 4.6: Pressure contours of Newtonian fluid flow for SplitP structure at different velocities at xy-axis (a) 0.5 mm/s (b) 0.6 mm/s (c) 0.7 mm/s (d) 0.8 mm/s, at yz-axis (e) 0.5 mm/s (f) 0.6 mm/s (g) 0.7 mm/s (h) 0.8 mm/s

flow conditions without creating excessively high-pressure environments that might damage seeded cells or hinder cellular infiltration. This capability is critical for vertebral implants, as efficient nutrient exchange is essential to maintain cellular viability and promote homogeneous tissue regeneration, particularly in VCFs, where biological conditions may already be compromised.

The velocity contours generated from the CFD simulations further elucidate the fluid dynamics within these scaffold structures. Analysis of velocity contours clearly revealed areas of maximal fluid velocity primarily located in the central regions of both Neovius and SplitP scaffolds as shown in Figure 4.7 and 4.8. At

lower velocities (0.5 mm/s), the fluid demonstrated relatively uniform distributions throughout both scaffold structures, with slightly increased central velocities indicated by localized red contour regions. With increasing velocities (0.6 mm/s to 0.8 mm/s), a progressive intensification of velocity was evident, predominantly in the central internal pores, as represented by the expansion of high-velocity regions (red zones) within the scaffold core. Notably, these velocity maxima within the scaffold core are advantageous for scaffold performance, as centrally enhanced velocities can aid nutrient diffusion into the scaffold's inner regions, where nutrient availability often becomes limited due to diffusion constraints.

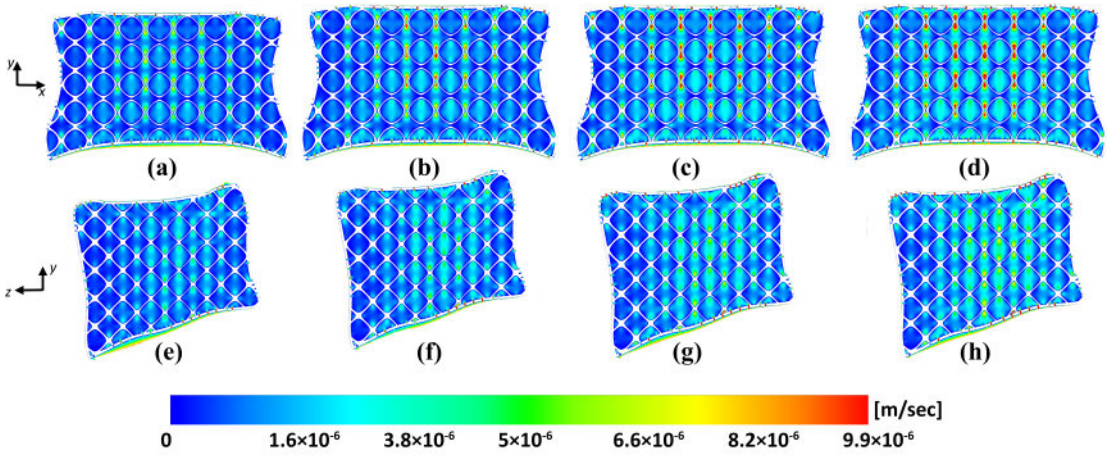


FIGURE 4.7: Velocity contours of Newtonian fluid flow for Neovius structure at different velocities at xy-axis (a) 0.5 mm/s (b) 0.6 mm/s (c) 0.7 mm/s (d) 0.8 mm/s, at yz-axis (e) 0.5 mm/s (f) 0.6 mm/s (g) 0.7 mm/s (h) 0.8 mm/s

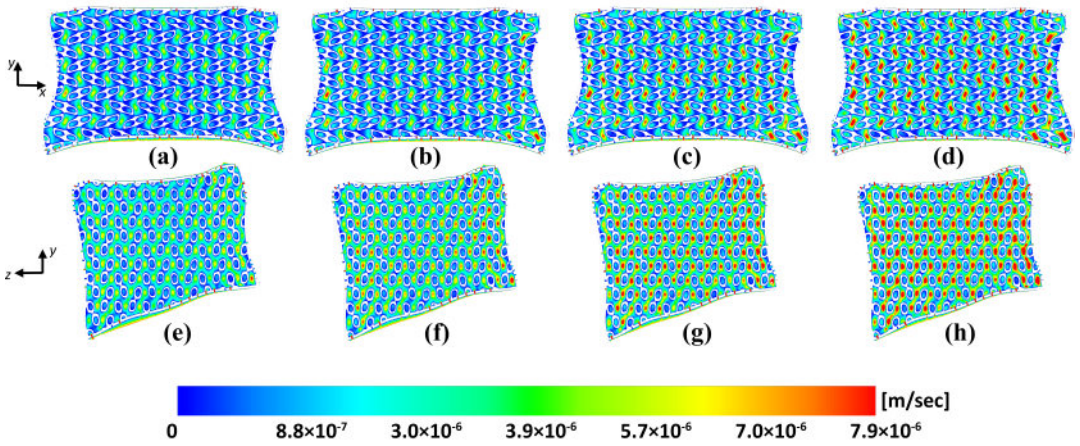


FIGURE 4.8: Velocity contours of Newtonian fluid flow for SplitP structure at different velocities at xy-axis (a) 0.5 mm/s (b) 0.6 mm/s (c) 0.7 mm/s (d) 0.8 mm/s, at yz-axis (e) 0.5 mm/s (f) 0.6 mm/s (g) 0.7 mm/s (h) 0.8 mm/s

Previous studies have highlighted that optimal scaffold architecture should support balanced velocity profiles, avoiding extensive stagnant zones or excessively turbulent regions to enhance nutrient transport and cell attachment [132, 133]. Our simulation results closely align with these desirable flow conditions. The absence of pronounced stagnant areas, combined with centralized velocity maxima, indicates effective and balanced nutrient transport capabilities within both scaffold types. Moreover, the progressive increase of velocity magnitudes and consistent central distribution pattern across increasing inlet velocities suggests robustness and reliability of the scaffolds' internal architecture, capable of accommodating varying physiological flow conditions.

The observed centralized velocity enhancement, consistent across all tested inlet velocities, suggests another critical biological implication: central scaffold regions, which are typically more challenging for nutrients to reach due to limited diffusion, are effectively targeted by higher fluid velocities. This ensures more homogeneous nutrient delivery, essential for uniform cell growth, differentiation, and bone regeneration throughout the scaffold structure, an especially crucial feature in vertebral implants, where mechanical and biological integrity across the scaffold is vital to maintaining spinal stability and promoting effective repair of vertebral compression fractures.

Furthermore, the remarkable similarity in fluidic performance between Neovius and SplitP structures across all tested velocities indicates that scaffold selection can be flexible, based on additional biomechanical or manufacturing considerations. Both structures demonstrate equivalent performance from a fluid dynamics perspective, providing comparable biological and mechanical stimuli to cells seeded within the scaffold. This flexibility is highly beneficial for practical clinical applications, as it permits scaffold selection based on factors like mechanical strength, ease of fabrication, or patient-specific anatomical considerations, without compromising on the essential fluid dynamic properties required for effective vertebral body regeneration.

### 4.2.2 Newtonian Fluid Flow - Permeability

Permeability is a critical parameter in scaffold design for tissue engineering applications, particularly for bone scaffolds intended to treat VCFs. It defines the scaffold's ability to facilitate the transport of nutrients, oxygen, and waste products, which directly impacts cellular viability, differentiation, and overall bone regeneration efficacy. In this study, permeability was measured for both Neovius and SplitP scaffolds under Newtonian fluid flow conditions at varying fluid velocities (0.5, 0.6, 0.7, and 0.8 mm/s). The results obtained were highly consistent across different flow velocities and demonstrated negligible variation between the two scaffold types, suggesting robust structural similarity and fluidic performance as shown in Table 4.1. The permeability values recorded for Neovius and SplitP

TABLE 4.1: Permeability of Neovius and SplitP structures across different velocities

| **Structure Type** | **Velocity (mm/sec)** | **Permeability ($m^2$)** |
|---|---|---|
| Neovius | 0.5 | $3.28712 \times 10^{-6}$ |
| | 0.6 | $3.25449 \times 10^{-6}$ |
| | 0.7 | $3.22175 \times 10^{-6}$ |
| | 0.8 | $3.18908 \times 10^{-6}$ |
| SplitP | 0.5 | $3.28865 \times 10^{-6}$ |
| | 0.6 | $3.25603 \times 10^{-6}$ |
| | 0.7 | $3.22329 \times 10^{-6}$ |
| | 0.8 | $3.19063 \times 10^{-6}$ |

scaffolds were approximately on the order of $10^{-6}\,m^2$, reflecting highly porous and well-interconnected internal architectures. The trend of these values aligns well with the reported permeability trends, as it is highly dependent on the porosity and pore size of the body [81, 84]. The observed negligible difference in permeability between SplitP and Neovius scaffolds suggests that both architectures similarly facilitate fluid transport. This similarity in permeability is logically attributable to their comparable internal pore structures, characterized by periodic, smooth, and well-connected channels. Literature reports further support that permeability is primarily governed by pore size, geometry, and interconnectivity, all of which are typically similar in TPMS-based scaffold designs [82, 134]. Hence, the minor

differences observed between the two scaffolds are within expected variability and are unlikely to impact their practical performance significantly.

The consistency of permeability values across different fluid velocities (0.5 mm/s to 0.8 mm/s) also indicates that the scaffolds maintain stable internal architectures, effectively handling physiological variations in fluid flow without significant structural or functional deviations. It is well-established in the literature that high and stable permeability within scaffolds directly correlates with improved cell viability and proliferation due to efficient nutrient and oxygen transport. For instance, several researchers demonstrated that optimal permeability levels significantly enhance osteoblast activity and proliferation within scaffolds [135, 136].

Importantly, the permeability results from this study suggest that both SplitP and Neovius scaffolds can support robust nutrient delivery throughout their internal regions, particularly critical in vertebral implants where uniform bone regeneration is essential for spinal integrity. Consistent permeability ensures balanced fluid flow and nutrient distribution across the scaffold, thus minimizing potential localized areas of cellular deprivation or poor bone regeneration. Such balanced transport capability significantly enhances the clinical effectiveness of scaffolds, ensuring rapid and homogeneous bone formation within the implant structure, crucial for effective repair and healing of vertebral compression fractures.

### 4.2.3 Newtonian Fluid Flow – WSS

WSS is a crucial biomechanical stimulus influencing cellular behavior within tissue-engineered scaffolds. In bone tissue engineering, particularly for load-bearing applications such as vertebral body regeneration, optimal levels of WSS play a vital role in regulating osteoblastic activity, extracellular matrix production, and overall bone tissue formation. Therefore, evaluating WSS across scaffold designs helps determine their capability to support bone healing in cases like VCFs.

Under Newtonian flow conditions, the Neovius scaffold exhibited WSS values ranging from 0.00012 Pa at 0.5 mm/s to 0.00045 Pa at 0.8 mm/s, while SplitP ranged

from 0.00021 Pa to 0.00036 Pa as shown in Table 4.2. This consistent increase with velocity reflects the linear behavior expected in laminar Newtonian flow, where WSS scales proportionally with fluid velocity, as reported in the literature [121]. The small difference between structures confirms their comparable surface topology and channel connectivity. The TPMS geometry plays a decisive role here.

TABLE 4.2: WSS values for Neovius and SplitP structures at different velocities

| **Structure Type** | **Velocity (mm/sec)** | **WSS (Pa)** |
|---|---|---|
| Neovius | 0.5 | 0.000127802 |
| | 0.6 | 0.000335596 |
| | 0.7 | 0.000393871 |
| | 0.8 | 0.000452839 |
| SplitP | 0.5 | 0.000219889 |
| | 0.6 | 0.000265465 |
| | 0.7 | 0.000311608 |
| | 0.8 | 0.000358321 |

Both Neovius and SplitP feature continuous, smooth surfaces that distribute flow evenly and prevent local WSS spikes. This contrasts with strut-based or irregular scaffolds where edge effects can generate non-uniform shear zones. In a vertebral scaffold context, such smooth distributions reduce the risk of non-homogeneous bone regeneration, especially in the critical core of the implant, which must ossify uniformly to restore spinal load transfer.

The consistency of WSS trends across all tested velocities also supports structural robustness. Even as inlet velocity increased to 0.8 mm/s, no abrupt WSS elevation was observed. This predictability is advantageous in clinical use, where physiological variations in spinal blood flow or dynamic loading may shift local perfusion rates.

### 4.2.4 Non-Newtonian Fluid Flow - Fluidic Characteristics

In bone tissue engineering applications such as vertebral body repair, the behavior of blood and nutrient flow through scaffold architectures is better approximated using non-Newtonian models. Unlike Newtonian fluids, non-Newtonian behavior,

particularly shear-thinning, closely resembles the rheology of plasma and blood, where viscosity decreases with increasing shear rate. Capturing this behavior is essential for predicting accurate pressure profiles and velocity distributions within scaffolds, especially for load-bearing applications like the L4–L5 vertebra, where consistent nutrient perfusion is crucial for cell survival and osteogenesis.

TABLE 4.3: Pressure drop values for Neovius and SplitP structures at different velocities

| **Structure Type** | **Velocity (mm/sec)** | **Pressure Drop (Pa)** |
|---|---|---|
| Neovius | 0.5 | 0.1243723 |
| | 0.6 | 0.1417903 |
| | 0.7 | 0.1584746 |
| | 0.8 | 0.1745749 |
| SplitP | 0.5 | 0.1243493 |
| | 0.6 | 0.1417647 |
| | 0.7 | 0.1584468 |
| | 0.8 | 0.1745451 |

The pressure drop values for both scaffold types increased consistently with inlet velocity, ranging from 0.124 Pa at 0.5 mm/s to 0.1745 Pa at 0.8 mm/s are shown in Table 4.3. The negligible differences in pressure drop between Neovius and SplitP confirm that both structures offer comparable hydraulic resistance to non-Newtonian flow. This is attributed to their nearly identical total porosity and surface curvature distribution, which governs bulk permeability and flow pathways.

Despite modeling shear-thinning behavior, the pressure increase remains nearly linear with velocity. This is because, at the relatively low velocities used in this study, the local shear rates are moderate, and the viscosity reduction due to shear thinning is proportional, maintaining an approximately linear pressure-flow relationship. This observation is consistent with prior studies on TPMS-based scaffold flow dynamics under power-law fluids [81, 121], where fluid resistance remained predictable within physiological ranges.

The pressure field contours shown in Figure 4.9 and 4.10 offer further insight into scaffold behavior. In both Neovius and SplitP, the highest pressure (red zones) is concentrated near the inlet, and pressure decreases smoothly along the direction

of flow toward the outlet. This reflects a stable and continuous pressure gradient, indicative of low turbulent effects and minimal viscous losses. Importantly,

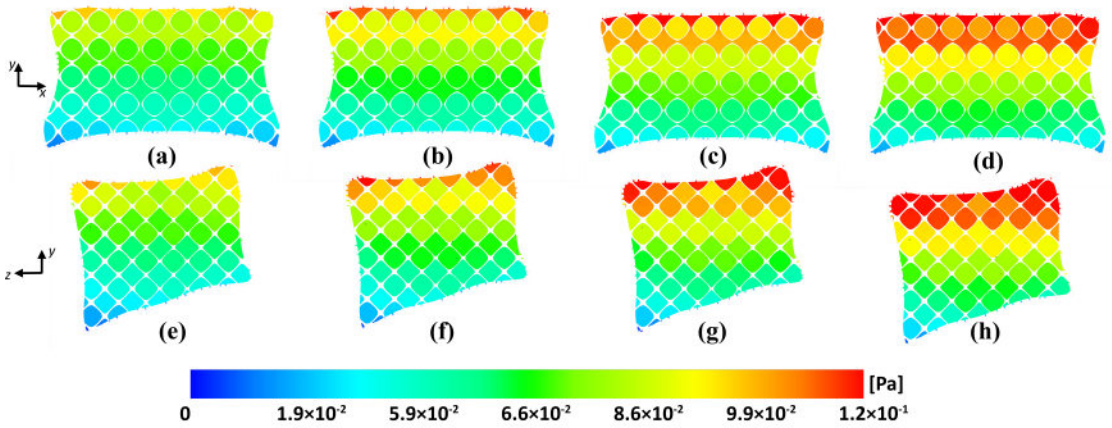


FIGURE 4.9: Pressure contours of Non-Newtonian fluid flow for Neovius structure at different velocities at xy-axis (a) 0.5 mm/s (b) 0.6 mm/s (c) 0.7 mm/s (d) 0.8 mm/s, at yz-axis (e) 0.5 mm/s (f) 0.6 mm/s (g) 0.7 mm/s (h) 0.8 mm/s

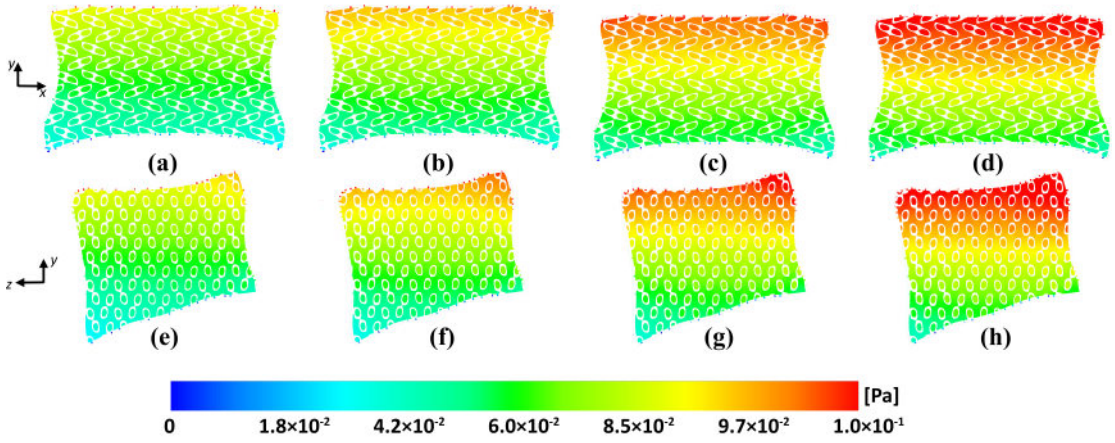


FIGURE 4.10: Pressure contours of Non-Newtonian fluid flow for SplitP structure at different velocities at xy-axis (a) 0.5 mm/s (b) 0.6 mm/s (c) 0.7 mm/s (d) 0.8 mm/s, at yz-axis (e) 0.5 mm/s (f) 0.6 mm/s (g) 0.7 mm/s (h) 0.8 mm/s

the pressure drop is spatially uniform, with no sharp gradients or localized spikes. This distribution ensures that the driving force for perfusion is spread evenly across the scaffold cross-section, preventing preferential flow paths or under-perfused regions. In clinical contexts such as the L4–L5 vertebra, this helps achieve balanced nutrient distribution, avoiding hypoxic core zones that are often responsible for incomplete ossification. Moreover, the absence of abrupt pressure changes near the pore junctions confirms that the TPMS geometry supports a favorable flow

regime with reduced energy dissipation. This is particularly advantageous when scaffolds rely on endogenous perfusion (i.e., no external pumping), where even small resistance can significantly impact flow penetration.

The velocity contours for Neovius and SplitP shown in Figure 4.11 and 4.12 reveal critical internal flow dynamics. High-velocity zones, indicated by red regions, were not located at the inlet but appeared centrally within the scaffold along the primary z-axis. This is a direct result of the internal geometry, where flow converges through continuous pore networks before expanding again, creating central acceleration zones. These features reflect the classical behavior of fluid in smoothly

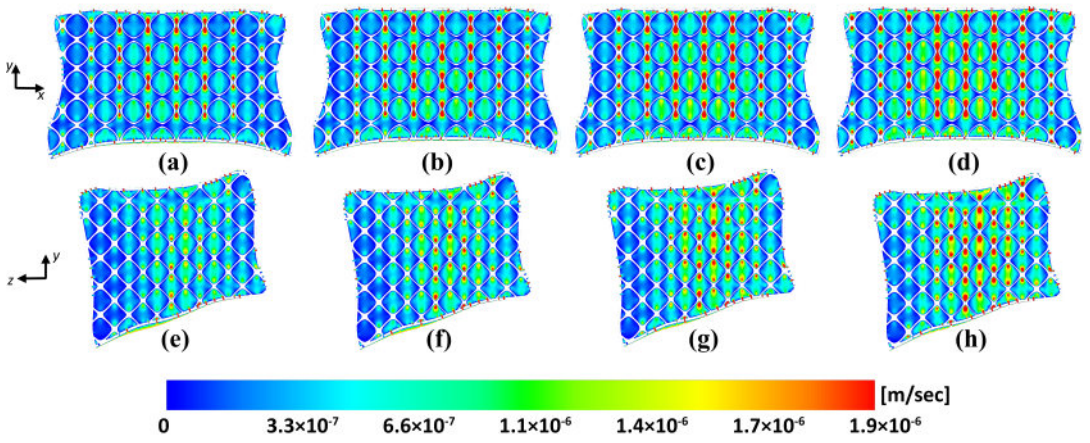


FIGURE 4.11: Velocity contours of Non-Newtonian fluid flow for Neovius structure at different velocities at xy-axis (a) 0.5 mm/s (b) 0.6 mm/s (c) 0.7 mm/s (d) 0.8 mm/s, at yz-axis (e) 0.5 mm/s (f) 0.6 mm/s (g) 0.7 mm/s (h) 0.8 mm/s

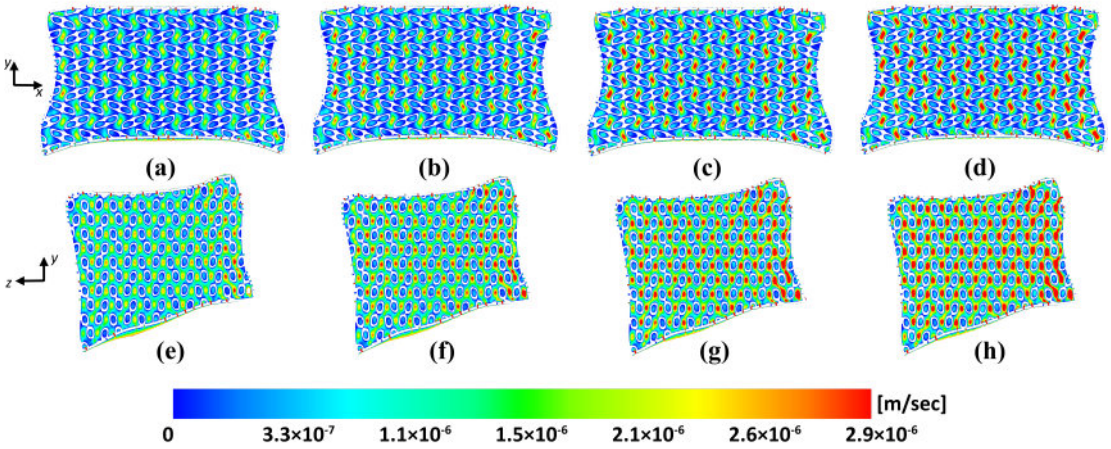


FIGURE 4.12: Velocity contours of Non-Newtonian fluid flow for SplitP structure at different velocities at xy-axis (a) 0.5 mm/s (b) 0.6 mm/s (c) 0.7 mm/s (d) 0.8 mm/s, at yz-axis (e) 0.5 mm/s (f) 0.6 mm/s (g) 0.7 mm/s (h) 0.8 mm/s

constricted porous domains. As the fluid passes through converging saddle-shaped channels, the cross-sectional area temporarily decreases, increasing local velocity according to the continuity equation. This mechanism explains why maximum flow velocity is seen in the scaffold core rather than the inlet. The TPMS surface also eliminates sudden expansions or contractions that would typically cause flow separation or recirculation. As a result, both Neovius and SplitP enable smooth laminar transport across the entire domain, supporting deep scaffold perfusion, a key requirement for uniform tissue regeneration in vertebral implants.

### 4.2.5 Non-Newtonian Fluid Flow – Permeability

Permeability plays a crucial role in scaffold design, as it directly impacts the flow of fluids through the scaffold, ensuring the delivery of nutrients and oxygen to cells and the removal of metabolic waste products. In the case of vertebral body implants, maintaining the right level of permeability is essential for promoting bone regeneration and osteoblast migration.

For the Neovius and SplitP scaffolds under non-Newtonian conditions, the permeability values were measured at different inlet velocities (0.5, 0.6, 0.7, and 0.8 mm/s). As shown in Table 4.4, both scaffolds demonstrated a slight reduction in permeability with increasing fluid velocity.

TABLE 4.4: Permeability values for Neovius and SplitP structures at different velocities

| **Structure Type** | **Velocity (mm/sec)** | **Permeability ($m^2$)** |
|---|---|---|
| Neovius | 0.5 | $1.54954 \times 10^{-6}$ |
| | 0.6 | $1.54520 \times 10^{-6}$ |
| | 0.7 | $1.54061 \times 10^{-6}$ |
| | 0.8 | $1.53579 \times 10^{-6}$ |
| SplitP | 0.5 | $1.54995 \times 10^{-6}$ |
| | 0.6 | $1.54560 \times 10^{-6}$ |
| | 0.7 | $1.54099 \times 10^{-6}$ |
| | 0.8 | $1.53616 \times 10^{-6}$ |

The observed decrease in permeability with increasing velocity is consistent with shear-thinning behavior of non-Newtonian fluids, where the viscosity of the fluid

decreases as the shear rate (velocity) increases. At higher velocities, the fluid becomes "thinner," which results in faster fluid movement through the scaffold's porous structure. However, the effective permeability (which is the rate at which fluid can pass through the structure) decreases slightly, as the shear-thinning behavior allows the fluid to pass more easily through larger pores but slightly reduces the total resistance for higher velocity flows.

The changes in permeability are very small, indicating that the overall fluid transport capability of both scaffold types remains largely unchanged despite varying fluid velocities. This consistency supports the stability of these scaffolds under fluctuating flow conditions, which is crucial for vertebral implants, where blood flow can vary depending on the patient and post-surgery conditions. These findings are in line with existing literature [135, 136], where TPMS-based scaffolds have shown consistent permeability values across various shear rates, ensuring that scaffolds support stable perfusion environments for osteoblast proliferation and bone regeneration.

The minor reductions in permeability with increasing velocity are clinically significant because they suggest that even under dynamic flow conditions (such as during physical activity or increased blood flow), the scaffolds will continue to maintain adequate fluid flow for cell survival and uniform tissue formation. For lumber vertebral body implants, this is essential for ensuring efficient nutrient delivery throughout the scaffold and promoting uniform bone tissue integration, especially in the L4–L5 region, where the vertebrae are critical for load-bearing.

### 4.2.6 Non-Newtonian Fluid Flow – WSS

WSS plays a pivotal role in bone tissue engineering by influencing osteoblast differentiation and the remodeling process within scaffolds. It is the key mechanical signal that governs cell behavior, such as adhesion, migration, and differentiation, which is especially relevant in vertebral scaffold applications where uniform bone regeneration is required for structural stability.

Under non-Newtonian flow conditions, the WSS increases with the velocity in both Neovius and SplitP scaffolds, demonstrating a clear correlation between higher inlet velocities and increased shear stress. As shown in Table 4.5, the Neovius scaffold exhibited WSS values ranging from:

TABLE 4.5: WSS values for Neovius and SplitP structures at different velocities

| **Structure Type** | **Velocity (mm/sec)** | **WSS (Pa)** |
|---|---|---|
| Neovius | 0.5 | 0.001546756 |
| | 0.6 | 0.001762523 |
| | 0.7 | 0.001968704 |
| | 0.8 | 0.002167144 |
| SplitP | 0.5 | 0.001257392 |
| | 0.6 | 0.001432859 |
| | 0.7 | 0.001600409 |
| | 0.8 | 0.00176161 |

This trend shows that both scaffolds exhibit an increase in WSS as fluid velocity rises, with Neovius consistently showing higher WSS values at each corresponding velocity. The difference in WSS between Neovius and SplitP is attributable to the subtle variations in surface curvature and pore connectivity between the two TPMS architectures, with Neovius having slightly more exposed surface area and greater channel interconnectivity, promoting higher fluid velocity and shear stress at the scaffold walls. At low to moderate shear rates, WSS stimulates bone-forming cells (osteoblasts) without inducing cell apoptosis, making both Neovius and SplitP suitable for promoting bone regeneration. The WSS values observed in both Neovius and SplitP scaffolds are highly favorable for promoting osteoblast differentiation and bone tissue formation in the L4–L5 vertebral body, where mechanical stimulation plays a critical role in the healing process. The difference in WSS values between the two scaffolds is minimal, suggesting that both designs will provide comparable mechanical cues in vivo, enhancing cell migration and osteogenesis. The results suggest that these scaffold types can enhance osteogenesis by providing mechanical cues for bone remodeling during the healing process of VCFs.

The centralized WSS maxima observed in the scaffolds ensure that even the deeper regions of the scaffold, which are typically less perfused, will receive sufficient shear-induced mechanical stimulation. This is critical in vertebral applications, where ensuring uniform tissue growth throughout the scaffold is necessary to restore mechanical integrity to the spine, particularly in regions such as the L4–L5 vertebra, which bear considerable mechanical loads.

# Chapter 5

# Conclusion and Future Recommendations

## 5.1 Conclusion

This study presents a design and evaluation of a biomimetic L4 vertebral body implant incorporating TPMS structures to restore structural safety and fluid transport performance in VCF treatment. Six TPMS configurations (Gyroid, Diamond, Schwarz, Lidinoid, Neovius, and SplitP) were analyzed through AH, from which Neovius and SplitP were selected at 80% porosity (relative density 0.2) for their ability to match the effective modulus of trabecular bone while preserving high permeability for osseointegration. These designs were subsequently assessed through FEA and CFD. Key findings include:

### 5.1.1 Structural Response Under Physiological Loading

Structural response under physiological loading confirmed that both Neovius and SplitP implants restored vertebral height and maintained physiological stress distribution. Deformations remained within safe biomechanical limits under flexion, extension, lateral bending, and axial rotation.

### 5.1.2 Stress Distribution

Von Mises stress distributions indicated that both structures provided adequate safety margins, with SplitP demonstrating more even stress distribution as compared to Neovius, thus reducing the risk of localized mechanical failure.

### 5.1.3 Newtonian Fluid Transport

Newtonian fluid transport characteristics revealed permeability ranges of $3.28865 \times 10^{-6}$ to $3.19063 \times 10^{-6}\,\mathrm{m}^2$ for SplitP and $3.28712 \times 10^{-6}$ to $3.18908 \times 10^{-6}\,\mathrm{m}^2$ for Neovius. Corresponding WSS values were 0.00022–0.00036 Pa for SplitP and 0.00013–0.00045 Pa for Neovius, confirming stable mass transport supportive of nutrient delivery and osteogenesis.

### 5.1.4 Non-Newtonian Fluid Transport

Non-Newtonian flow conditions reduced permeability to $1.54995 \times 10^{-6}$ to $1.53616 \times 10^{-6}\,\mathrm{m}^2$ for SplitP and $1.54954 \times 10^{-6}$ to $1.53579 \times 10^{-6}\,\mathrm{m}^2$ for Neovius, while increasing WSS to 0.0013–0.0018 Pa and 0.0015–0.0022 Pa, respectively. These values remain within the optimal physiological range for osteogenic stimulation.

The overall results suggest that a SplitP-based implant provides the best combined performance profile, balancing mechanical safety, stress distribution, and fluid transport favorable for bone ingrowth and regeneration.

## 5.2 Future Recommendations

There are numerous opportunities for advancements and future research to expand the clinical use of implants based on TPMS:

### 5.2.1 Functionally Graded Materials (FGMs)

Future work could explore the multi-material designs or FGMs to combine the advantages of both rigidity and flexibility for immediate mechanical stability and long-term biological compatibility.

### 5.2.2 Surface Coating Technologies

For Neovius implants that experience higher localized stresses, further investigation into surface modification techniques, such as bioactive coatings or osteointegrative coatings, could enhance their osseointegration potential and reduce fatigue risk. This could be combined with the use of osteoconductive materials to encourage faster bone healing.

### 5.2.3 Additive Manufacturing

The use of additive manufacturing can be utilized for customized implants based on patient-specific needs, especially with the advent of multi-material printing. This will enable further optimization of implant design in terms of porosity, geometry, and biocompatibility, tailored to the unique anatomical features of individual patients.

### 5.2.4 In Vivo Testing and Clinical Trials

While the FEA results demonstrate promising mechanical performance, in vivo testing and clinical trials are essential for further validating the long-term biological integration, fatigue behavior, and clinical outcomes of TPMS-based implants. This will provide invaluable data on how the implants perform under real-life, dynamic conditions, helping to refine design and material choices for future clinical applications.

# Bibliography


[1] F. Galbusera and T. Bassani, "The spine: a strong, stable, and flexible structure with biomimetics potential," *Biomimetics*, vol. 4, no. 3, p. 60, 2019.

[2] Y. Huang, Y. Dong, F. Liu, Y. Li, H. Wang, and J. Zhang, "Bilateral spondylolysis of lumbar vertebra secondary to long spinal fusion for idiopathic scoliosis: A case report and review of literature," *Orthopaedic Surgery*, vol. 16, no. 10, pp. 2569–2573, 2024.

[3] M. Shaikh, F. Kahwash, Z. Lu, M. Alkhreisat, A. Mohammad, and I. Shyha, "Revolutionising orthopaedic implants—a comprehensive review on metal 3d printing with materials, design strategies, manufacturing technologies, and post-process machining advancements," *The International Journal of Advanced Manufacturing Technology*, vol. 134, no. 3, pp. 1043–1076, 2024.

[4] T. L. Rheumatology, "The global epidemic of low back pain," 2023.

[5] GlobeNewswire, "Chronic lower back pain market size to reach USD 6.12 Bn by 2033." GlobeNewswire, July 2024. Accessed: April 17, 2025.

[6] M. I. Page, *Additive Manufacturing of an Intervertebral Disc Repair Patch to Treat Spinal Herniation*. PhD thesis, Colorado State University, 2021.

[7] International Association for the Study of Pain (IASP), "The global burden of low back pain." International Association for the Study of Pain (IASP), 2021. Accessed: March 12, 2025.

[8] M. L. Ferreira, K. De Luca, L. M. Haile, J. D. Steinmetz, G. T. Culbreth, M. Cross, J. A. Kopec, P. H. Ferreira, F. M. Blyth, R. Buchbinder, *et al.*,

"Global, regional, and national burden of low back pain, 1990–2020, its attributable risk factors, and projections to 2050: a systematic analysis of the global burden of disease study 2021," *The Lancet Rheumatology*, vol. 5, no. 6, pp. e316–e329, 2023.

[9] F. Zafar, Y. F. Qasim, M. U. Farooq, I. Shamael, I. U. Khan, D. H. Khan, and D. H. Khan, "The frequency of different risk factors for lower back pain in a tertiary care hospital," *Cureus*, vol. 10, no. 8, 2018.

[10] B. Sassack and J. D. Carrier, "Anatomy, back, lumbar spine," in *StatPearls*, StatPearls Publishing, 2023.

[11] Spine-health, "Lumbar spine anatomy and pain." Spine-health, 2020. Accessed: March 12, 2025.

[12] C.J.D. III, C. DiPompeo, and M. Varacallo, "Vertebral compression fractures," *StatPearls*, 2023. Accessed: March 13, 2025.

[13] C. C. Wong and M. J. McGirt, "Vertebral compression fractures: a review of current management and multimodal therapy," *Journal of multidisciplinary healthcare*, pp. 205–214, 2013.

[14] Physiopedia, "Lumbar compression fracture," 2025. Accessed: March 13, 2025.

[15] D. Alexandru and W. So, "Evaluation and management of vertebral compression fractures," *The permanente journal*, vol. 16, no. 4, p. 46, 2012.

[16] Spine Info, "Vertebral compression fracture: Definition," 2023. Accessed: May 2, 2025.

[17] A. Ameis, K. Randhawa, H. Yu, P. Cote, S. Haldeman, R. Chou, E. L. Hurwitz, M. Nordin, J. J. Wong, H. M. Shearer, *et al.*, "The global spine care initiative: a review of reviews and recommendations for the non-invasive management of acute osteoporotic vertebral compression fracture pain in low-and middle-income communities," *European Spine Journal*, vol. 27, pp. 861–869, 2018.

[18] A. D. Kaye, M. R. Jones, A. M. Kaye, J. G. Ripoll, V. Galan, B. D. Beakley, F. Calixto, J. L. Bolden, R. D. Urman, and L. Manchikanti, "Prescription opioid abuse in chronic pain: an updated review of opioid abuse predictors and strategies to curb opioid abuse: part 1," *Pain physician*, vol. 20, no. 2, p. S93, 2017.

[19] L. Manchikanti, A. M. Kaye, N. N. Knezevic, H. McAnally, A. M. Trescot, S. Blank, V. Pampati, S. Abdi, J. S. Grider, A. D. Kaye, *et al.*, "Responsible, safe, and effective prescription of opioids for chronic non-cancer pain: American society of interventional pain physicians (asipp) guidelines," *Pain physician*, vol. 20, no. 2, p. S3, 2017.

[20] I. K. Genev, M. K. Tobin, S. P. Zaidi, S. R. Khan, F. M. Amirouche, and A. I. Mehta, "Spinal compression fracture management: a review of current treatment strategies and possible future avenues," *Global spine journal*, vol. 7, no. 1, pp. 71–82, 2017.

[21] L. Xie, Z.-G. Zhao, S.-J. Zhang, and Y.-B. Hu, "Percutaneous vertebroplasty versus conservative treatment for osteoporotic vertebral compression fractures: An updated meta-analysis of prospective randomized controlled trials," *International Journal of Surgery*, vol. 47, pp. 25–32, 2017.

[22] O. Adamska, K. Modzelewski, A. Stolarczyk, and J. Kseniuk, "Is kummell's disease a misdiagnosed and/or an underreported complication of osteoporotic vertebral compression fractures? a pattern of the condition and available treatment modalities," *Journal of Clinical Medicine*, vol. 10, no. 12, p. 2584, 2021.

[23] D. Beall, M. P. Lorio, B. M. Yun, M. J. Runa, K. L. Ong, and C. B. Warner, "Review of vertebral augmentation: an updated meta-analysis of the effectiveness," *International Journal of Spine Surgery*, vol. 12, no. 3, pp. 295–321, 2018.

[24] Z. You, K. Wu, Y. Jiang, and J. Chen, "Effect of vertebral kyphoplasty versus vertebroplasty on pain and indicators of imaging parameters of the

injured vertebrae in patients with osteoporotic vertebral compression fractures: a meta-analysis," *Journal of orthopaedic surgery and research*, vol. 20, no. 1, p. 199, 2025.

[25] S. D'Oria, M. Dibenedetto, E. Squillante, C. Somma, C. J. Hannan, D. Giraldi, and V. Fanelli, "Traumatic compression fractures in thoracic-lumbar junction: vertebroplasty vs conservative management in a prospective controlled trial," *Journal of NeuroInterventional Surgery*, vol. 14, no. 2, pp. 202–206, 2022.

[26] G. B. Calais, G. D. Garcia, C. F. de Moura Júnior, J. D. M. Soares, L. M. F. Lona, M. M. Beppu, J. Hernandez-Montelongo, and J. B. M. Rocha Neto, "Therapeutic functions of medical implants from various material categories with integrated biomacromolecular systems," *Frontiers in bioengineering and biotechnology*, vol. 12, p. 1509397, 2025.

[27] G. Rafikova, S. Piatnitskaia, E. Shapovalova, S. Chugunov, V. Kireev, D. Ialiukhova, A. Bilyalov, V. Pavlov, and J. Kzhyshkowska, "Interaction of ceramic implant materials with immune system," *International Journal of Molecular Sciences*, vol. 24, no. 4, p. 4200, 2023.

[28] F. D. Al-Shalawi, M. A. Hanim, M. Ariffin, C. L. S. Kim, D. Brabazon, R. Calin, and M. O. Al-Osaimi, "Biodegradable synthetic polymer in orthopaedic application: A review," *Materials Today: Proceedings*, vol. 74, pp. 540–546, 2023.

[29] P. Nogueira, P. Lopes, L. Oliveira, J. L. Alves, J. P. Magrinho, A. M. d. Deus, M. F. Vaz, and M. B. Silva, "Evaluation of lattice structures for medical implants: A study on the mechanical properties of various unit cell types," *Metals*, vol. 14, no. 7, p. 780, 2024.

[30] A. Ahmad, L. Belluomo, M. Bici, and F. Campana, "Bird's eye view on lattice structures: Design issues and applications for best practices in mechanical design," *Metals*, vol. 13, no. 10, p. 1666, 2023.

[31] M. Peto, J. García-Ávila, C. A. Rodriguez, H. R. Siller, J. V. L. da Silva, and E. Ramírez-Cedillo, "Review on structural optimization techniques for additively manufactured implantable medical devices," *Frontiers in Mechanical Engineering*, vol. 10, p. 1353108, 2024.

[32] M. S. Azmi, M. H. Jalil, and M. H. Mazlan, "Titanium strut-based lattice structure via additive manufacturing for spinal cage: A review," in *International Conference on Movement, Health and Exercise*, pp. 293–321, Springer, 2024.

[33] C. Chatzigeorgiou, B. Piotrowski, Y. Chemisky, P. Laheurte, and F. Meraghni, "Numerical investigation of the effective mechanical properties and local stress distributions of tpms-based and strut-based lattices for biomedical applications," *Journal of the mechanical behavior of biomedical materials*, vol. 126, p. 105025, 2022.

[34] Y. Wakjira, A. Cioni, and H. G. Lemu, "Current status of the application of additive-manufactured tpms structure in bone tissue engineering," *Progress in Additive Manufacturing*, vol. 10, no. 2, pp. 1085–1102, 2025.

[35] B. Sokollu, O. Gulcan, and E. I. Konukseven, "Mechanical properties comparison of strut-based and triply periodic minimal surface lattice structures produced by electron beam melting," *Additive Manufacturing*, vol. 60, p. 103199, 2022.

[36] M. Rezapourian, I. Jasiuk, M. Saarna, and I. Hussainova, "Selective laser melted ti6al4v split-p tpms lattices for bone tissue engineering," *International Journal of Mechanical Sciences*, vol. 251, p. 108353, 2023.

[37] N. Van Viet, M. El-Rich, and W. Zaki, "Multidirectional mechanical properties of functionally graded triply periodic minimal surfaces for bone tissue engineering applications," *Composite Structures*, vol. 363, p. 119054, 2025.

[38] Atlantic Spine Center, "Vertebral compression fracture: Complications, symptoms, diagnosis, and treatment," 2025. Accessed: May 2, 2025.

[39] D. Alsoof, G. Anderson, C. L. McDonald, B. Basques, E. Kuris, and A. H. Daniels, "Diagnosis and management of vertebral compression fracture," *The American Journal of Medicine*, vol. 135, no. 7, pp. 815–821, 2022.

[40] S. Nian, Y. Zhao, C. Li, K. Zhu, N. Li, W. Li, and J. Chen, "Development and validation of a radiomics-based model for predicting osteoporosis in patients with lumbar compression fractures," *The Spine Journal*, vol. 24, no. 9, pp. 1625–1634, 2024.

[41] A. Eschler, P. Röpenack, P. K. Herlyn, J. Roesner, K. Pille, K. Büsing, B. Vollmar, T. Mittlmeier, and G. Gradl, "The standardized creation of a lumbar spine vertebral compression fracture in a sheep osteoporosis model induced by ovariectomy, corticosteroid therapy and calcium/phosphorus/vitamin d-deficient diet," *Injury*, vol. 46, pp. S17–S23, 2015.

[42] R. Eastell, S. L. Cedel, H. W. Wahner, B. L. Riggs, and L. J. Melton III, "Classification of vertebral fractures," *Journal of bone and mineral research*, vol. 6, no. 3, pp. 207–215, 1991.

[43] H.-W. Chen, W.-T. Wu, C.-M. Chang, T.-C. Yu, I.-H. Chen, and K.-T. Yeh, "Increased risk of osteoporotic vertebral compression fractures following epidural steroid injections in patients with lumbar degenerative disease: A retrospective cohort study," *Journal of Clinical Medicine*, vol. 13, no. 21, p. 6379, 2024.

[44] H. M. Do, H. T.-N. Doan, and S. N. Dinh, "Practical evaluation of risk factors in patients with osteoporosis-induced thoracic and lumbar vertebral compression fractures requiring surgery," *Surgery in Practice and Science*, vol. 19, p. 100260, 2024.

[45] D. Alsoof, G. Anderson, C. L. McDonald, B. Basques, E. Kuris, and A. H. Daniels, "Diagnosis and management of vertebral compression fracture," *The American Journal of Medicine*, vol. 135, no. 7, pp. 815–821, 2022.

[46] A.-R. Alimy, A. D. Anastasilakis, J. J. Carey, S. D'Oronzo, A. M. Naciu, J. Paccou, M. P. Yavropoulou, W. F. Lems, and T. Rolvien, "Conservative treatments in the management of acute painful vertebral compression fractures: a systematic review and network meta-analysis," *JAMA network open*, vol. 7, no. 9, pp. e2432041–e2432041, 2024.

[47] J. C. Petitt, A. Desai, A. Kashkoush, P. Ahorukomeye, T. O. Potter, A. Stout, and M. L. Kelly, "Failure of conservatively managed traumatic vertebral compression fractures: a systematic review," *World Neurosurgery*, vol. 165, pp. 81–88, 2022.

[48] C. L. Goldstein, N. B. Chutkan, T. J. Choma, and R. D. Orr, "Management of the elderly with vertebral compression fractures," *Neurosurgery*, vol. 77, pp. S33–S45, 2015.

[49] S. Kapetanakis, C. Chaniotakis, P. Zavridis, P. Kopsidas, S. Apostolakis, and N. Gkantsinikoudis, "Vertebroplasty and kyphoplasty in the management of osteoporotic vertebral compression fractures in elderly individuals: evaluation of the health-related quality of life," *European Journal of Translational Myology*, vol. 34, no. 3, p. 12274, 2024.

[50] M. J. McGirt, S. L. Parker, J.-P. Wolinsky, T. F. Witham, A. Bydon, and Z. L. Gokaslan, "Vertebroplasty and kyphoplasty for the treatment of vertebral compression fractures: an evidenced-based review of the literature," *The spine journal*, vol. 9, no. 6, pp. 501–508, 2009.

[51] R. Mattie, K. Laimi, S. Yu, and M. Saltychev, "Comparing percutaneous vertebroplasty and conservative therapy for treating osteoporotic compression fractures in the thoracic and lumbar spine: a systematic review and meta-analysis," *JBJS*, vol. 98, no. 12, pp. 1041–1051, 2016.

[52] L. Liang, X. Chen, W. Jiang, X. Li, J. Chen, L. Wu, and Y. Zhu, "Balloon kyphoplasty or percutaneous vertebroplasty for osteoporotic vertebral compression fracture? an updated systematic review and meta-analysis," *Annals of Saudi medicine*, vol. 36, no. 3, pp. 165–174, 2016.

[53] E. Chabert, E. Hugonnet, A. Kastler, L. Sakka, F. A. Rabbo, A. Zerroug, E. Coudeyre, B. Pereira, and G. Coll, "Vertebroplasty versus bracing in acute vertebral compression fractures: a prospective randomized trial," *Annals of physical and rehabilitation medicine*, vol. 66, no. 6, p. 101746, 2023.

[54] L. A. Nasto, E. Jannelli, V. Cipolloni, L. Piccone, A. Cattolico, A. Santagada, C. Pripp, A. S. Panni, and E. Pola, "Three generations of treatments for osteoporotic vertebral fractures: what is the evidence?," *Orthopedic Reviews*, vol. 14, no. 6, p. 38609, 2022.

[55] J. Parmar, A. Malik, G. Zemmedhun, and S. Javed, "Short-term clinical outcomes and safety of the spinejack implant system for the treatment of pathological vertebral compression fractures in cancer patients: A retrospective analysis," *Pain Practice*, vol. 25, no. 3, p. e70020, 2025.

[56] H. Xin, Q. Shi, X. Ning, Y. Chen, X. Jia, Z. Zhang, S. Zhu, Y. Li, F. Liu, and L. Kong, "Biomimetic mineralized fiber bundle-inspired scaffolding surface on polyetheretherketone implants promotes osseointegration," *Macromolecular Bioscience*, vol. 23, no. 4, p. 2200436, 2023.

[57] S. Tripathi, A. Raheem, M. Dash, P. Kumar, A. Elsebahy, H. Singh, G. Manivasagam, and H. S. Nanda, "Surface engineering of orthopedic implants for better clinical adoption," *Journal of Materials Chemistry B*, vol. 12, no. 44, pp. 11302–11335, 2024.

[58] G. Wang, Y. Cui, Y. Leng, S. Sun, B. Yuan, H. Liu, C. Peng, and D. Wu, "Engineered three-dimensional bioactive scaffold for enhanced bone regeneration through modulating transplanted adipose derived mesenchymal stem cell and stimulating angiogenesis," *Frontiers in Bioengineering and Biotechnology*, vol. 12, p. 1342590, 2024.

[59] D. Losic, "Advancing of titanium medical implants by surface engineering: recent progress and challenges," *Expert opinion on drug delivery*, vol. 18, no. 10, pp. 1355–1378, 2021.

[60] D. Rabbitt, V. M. Villapún, L. N. Carter, K. Man, M. Lowther, P. O'Kelly, A. J. Knowles, A. Mottura, Y. T. Tang, L. Luerti, *et al.*, "Rethinking biomedical titanium alloy design: A review of challenges from biological and manufacturing perspectives," *Advanced Healthcare Materials*, vol. 14, no. 4, p. 2403129, 2025.

[61] M. Sladkova-Faure, M. Pujari-Palmer, C. Öhman-Mägi, A. López, H. Wang Jr, H. Engqvist, and G. M. de Peppo, "A biomimetic engineered bone platform for advanced testing of prosthetic implants," *Scientific Reports*, vol. 10, no. 1, p. 22154, 2020.

[62] S. Jiang, M. Wang, and J. He, "A review of biomimetic scaffolds for bone regeneration: toward a cell-free strategy," *Bioengineering & Translational Medicine*, vol. 6, no. 2, p. e10206, 2021.

[63] D. B. Alemayehu, M. Todoh, and S.-J. Huang, "Advancing 3d dental implant finite element analysis: Incorporating biomimetic trabecular bone with varied pore sizes in voronoi lattices," *Journal of Functional Biomaterials*, vol. 15, no. 4, p. 94, 2024.

[64] X. Lv, S. Wang, Z. Xu, X. Liu, G. Liu, F. Cao, and Y. Ma, "Structural mechanical properties of 3d printing biomimetic bone replacement materials," *Biomimetics*, vol. 8, no. 2, p. 166, 2023.

[65] D. Kong, Q. Wang, J. Huang, Z. Zhang, X. Wang, Q. Han, and Y. Shi, "A biomimetic structural material with adjustable mechanical property for bone tissue engineering," *Advanced Functional Materials*, vol. 34, no. 8, p. 2305412, 2024.

[66] M. He, J.-L. Wang, S. Wang, X. Zhao, Y. Li, and W. Liu, "A novel of 3d-printing porous ti6al4v scaffold based on tpms for orthopedic implants: Design and biocompatibility testing," *Available at SSRN 4835348*.

[67] H. Montazerian, E. Davoodi, M. Asadi-Eydivand, J. Kadkhodapour, and M. Solati-Hashjin, "Porous scaffold internal architecture design based on

minimal surfaces: a compromise between permeability and elastic properties," *Materials & Design*, vol. 126, pp. 98–114, 2017.

[68] M. Afshar, A. P. Anaraki, H. Montazerian, and J. Kadkhodapour, "Additive manufacturing and mechanical characterization of graded porosity scaffolds designed based on triply periodic minimal surface architectures," *Journal of the mechanical behavior of biomedical materials*, vol. 62, pp. 481–494, 2016.

[69] M. Rezapourian, N. Kamboj, I. Jasiuk, and I. Hussainova, "Biomimetic design of implants for long bone critical-sized defects," *Journal of the Mechanical Behavior of Biomedical Materials*, vol. 134, p. 105370, 2022.

[70] J. Zhou, Y. Gui, Q. Xu, L. He, and Y. Long, "Investigation of permeability and biocompatibility of tpms structures printed by laser powder bed fusion using ti64-5cu alloy for orthopedic implants," *Materials Letters*, vol. 355, p. 135552, 2024.

[71] F. Günther, S. Pilz, F. Hirsch, M. Wagner, M. Kästner, A. Gebert, and M. Zimmermann, "Shape optimization of additively manufactured lattices based on triply periodic minimal surfaces," *Additive Manufacturing*, vol. 73, p. 103659, 2023.

[72] J. Kang, E. Dong, X. Li, Z. Guo, L. Shi, D. Li, and L. Wang, "Topological design and biomechanical evaluation for 3d printed multi-segment artificial vertebral implants," *Materials Science and Engineering: C*, vol. 127, p. 112250, 2021.

[73] L. Li, J. Shi, K. Zhang, L. Yang, F. Yu, L. Zhu, H. Liang, X. Wang, and Q. Jiang, "Early osteointegration evaluation of porous ti6al4v scaffolds designed based on triply periodic minimal surface models," *Journal of orthopaedic translation*, vol. 19, pp. 94–105, 2019.

[74] A. Paré, B. Charbonnier, P. Tournier, C. Vignes, J. Veziers, J. Lesoeur, B. Laure, H. Bertin, G. De Pinieux, G. Cherrier, *et al.*, "Tailored three-dimensionally printed triply periodic calcium phosphate implants: a preclinical study for craniofacial bone repair," *ACS biomaterials science & engineering*, vol. 6, no. 1, pp. 553–563, 2019.

[75] E. Lehder, I. Ashcroft, R. Wildman, L. Ruiz-Cantu, and I. Maskery, "A multiscale optimisation method for bone growth scaffolds based on triply periodic minimal surfaces," *Biomechanics and modeling in mechanobiology*, vol. 20, pp. 2085–2096, 2021.

[76] X. Guo, X. Zheng, Y. Yang, X. Yang, and Y. Yi, "Mechanical behavior of tpms-based scaffolds: a comparison between minimal surfaces and their lattice structures," *SN Applied Sciences*, vol. 1, no. 10, p. 1145, 2019.

[77] O. Al-Ketan, R. Rowshan, and R. K. A. Al-Rub, "Topology-mechanical property relationship of 3d printed strut, skeletal, and sheet based periodic metallic cellular materials," *Additive Manufacturing*, vol. 19, pp. 167–183, 2018.

[78] M. Shen, W. Qin, B. Xing, W. Zhao, S. Gao, Y. Sun, T. Jiao, and Z. Zhao, "Mechanical properties of 3d printed ceramic cellular materials with triply periodic minimal surface architectures," *Journal of the European Ceramic Society*, vol. 41, no. 2, pp. 1481–1489, 2021.

[79] M. Araya, M. Jaskari, T. Rautio, T. Guillén, and A. Järvenpää, "Assessing the compressive and tensile properties of tpms-gyroid and stochastic ti64 lattice structures: a study on laser powder bed fusion manufacturing for biomedical implants," *Journal of Science: Advanced Materials and Devices*, vol. 9, no. 1, p. 100663, 2024.

[80] R. Pugliese and S. Graziosi, "Biomimetic scaffolds using triply periodic minimal surface-based porous structures for biomedical applications," *SLAS technology*, vol. 28, no. 3, pp. 165–182, 2023.

[81] M. N. Shahid, M. M. Khan, M. U. Shahid, and S. Rasheed, "Fluidic properties of diamond and splitp structures with varying porosity levels in tissue engineering applications: A computational fluid dynamics analysis," *Engineering Proceedings*, vol. 75, no. 1, p. 39, 2024.

[82] M. Dias, P. R. Fernandes, J. M. Guedes, and S. J. Hollister, "Permeability analysis of scaffolds for bone tissue engineering," *Journal of biomechanics*, vol. 45, no. 6, pp. 938–944, 2012.

[83] F. P. Melchels, A. M. Barradas, C. A. Van Blitterswijk, J. De Boer, J. Feijen, and D. W. Grijpma, "Effects of the architecture of tissue engineering scaffolds on cell seeding and culturing," *Acta biomaterialia*, vol. 6, no. 11, pp. 4208–4217, 2010.

[84] M. N. Shahid, M. U. Shahid, S. Rasheed, M. Irfan, and M. A. Obeidi, "Computational investigation of the fluidic properties of triply periodic minimal surface (tpms) structures in tissue engineering," *Designs*, vol. 8, no. 4, p. 69, 2024.

[85] J. Feng, J. Fu, X. Yao, and Y. He, "Triply periodic minimal surface (tpms) porous structures: from multi-scale design, precise additive manufacturing to multidisciplinary applications," *International Journal of Extreme Manufacturing*, vol. 4, no. 2, p. 022001, 2022.

[86] F. Bobbert and A. Zadpoor, "Effects of bone substitute architecture and surface properties on cell response, angiogenesis, and structure of new bone," *Journal of Materials Chemistry B*, vol. 5, no. 31, pp. 6175–6192, 2017.

[87] K. Gupta and K. Meena, "Artificial bone scaffolds and bone joints by additive manufacturing: A review," *Bioprinting*, vol. 31, p. e00268, 2023.

[88] R. Verma, J. Kumar, N. K. Singh, S. K. Rai, K. K. Saxena, and J. Xu, "Design and analysis of biomedical scaffolds using tpms-based porous structures inspired from additive manufacturing," *Coatings*, vol. 12, no. 6, p. 839, 2022.

[89] J. Lv, Z. Jia, J. Li, Y. Wang, J. Yang, P. Xiu, K. Zhang, H. Cai, and Z. Liu, "Electron beam melting fabrication of porous ti6al4v scaffolds: cytocompatibility and osteogenesis," *Advanced Engineering Materials*, vol. 17, no. 9, pp. 1391–1398, 2015.

[90] F. A. Shah, O. Omar, F. Suska, A. Snis, A. Matic, L. Emanuelsson, B. Norlindh, J. Lausmaa, P. Thomsen, and A. Palmquist, "Long-term osseointegration of 3d printed cocr constructs with an interconnected open-pore architecture prepared by electron beam melting," *Acta biomaterialia*, vol. 36, pp. 296–309, 2016.

[91] S. A. Yavari, M. Croes, B. Akhavan, F. Jahanmard, C. Eigenhuis, S. Dadbakhsh, H. Vogely, M. Bilek, A. Fluit, C. Boel, *et al.*, "Layer by layer coating for bio-functionalization of additively manufactured meta-biomaterials," *Additive Manufacturing*, vol. 32, p. 100991, 2020.

[92] J. Qi, Y. Gong, H. Chen, J. He, Z. Qiao, Y. Chen, H. Shao, W. Li, G. Chen, M. Wang, *et al.*, "Design and 3d printing of interbody fusion cage based on tpms porous structure," *Applied Sciences*, vol. 11, no. 23, p. 11149, 2021.

[93] S. Arabnejad and D. Pasini, "Mechanical properties of lattice materials via asymptotic homogenization and comparison with alternative homogenization methods," *International Journal of Mechanical Sciences*, vol. 77, pp. 249–262, 2013.

[94] Z. Fang, C. Yan, W. Sun, A. Shokoufandeh, and W. Regli, "Homogenization of heterogeneous tissue scaffold: A comparison of mechanics, asymptotic homogenization, and finite element approach," *Applied Bionics and Biomechanics*, vol. 2, no. 1, pp. 17–29, 2005.

[95] B. Hassani and E. Hinton, "A review of homogenization and topology optimization i—homogenization theory for media with periodic structure," *Computers & Structures*, vol. 69, no. 6, pp. 707–717, 1998.

[96] S. J. Hollister and N. Kikuchi, "A comparison of homogenization and standard mechanics analyses for periodic porous composites," *Computational mechanics*, vol. 10, no. 2, pp. 73–95, 1992.

[97] T. T.-A.-V. G. 5), "Annealed." https://www.matweb.com/search/DataSheet.aspx?MatGUID=a0655d261898456b958e5f825ae85390&ckck=1, 2025. Accessed: May 13, 2025.

[98] J. Y. Rho, R. B. Ashman, and C. H. Turner, "Young's modulus of trabecular and cortical bone material: ultrasonic and microtensile measurements," *Journal of biomechanics*, vol. 26, no. 2, pp. 111–119, 1993.

[99] N. Bonnheim, *Fundamental Mechanisms of Load Transfer in the Human Vertebral Body Following Lumbar Total Disc Arthroplasty*. University of California, Berkeley, 2020.

[100] M. Bonczar, J. Koszewski, W. Czarnota, M. Dziedzic, P. Ostrowski, K. Możdżeń, A. Murawska, P. Hajdyła, A. Walocha, E. Walocha, *et al.*, "The morphology of the lumbar vertebrae: a systematic review with meta-analysis of 1481 individuals with implications for spine surgery," *Surgical and Radiologic Anatomy*, vol. 47, no. 1, p. 22, 2024.

[101] P. Cantogrel, S. Schuller, F. Lefebvre, Y. P. Charles, and J.-P. Steib, "Lower lumbar vertebra size and anatomic variation: an anatomo-radiologic study," *Orthopaedics & Traumatology: Surgery & Research*, vol. 105, no. 6, pp. 1137–1141, 2019.

[102] D. U. Erbulut, I. Zafarparandeh, C. R. Hassan, I. Lazoglu, and A. F. Ozer, "Determination of the biomechanical effect of an interspinous process device on implanted and adjacent lumbar spinal segments using a hybrid testing protocol: a finite-element study," *Journal of Neurosurgery: Spine*, vol. 23, no. 2, pp. 200–208, 2015.

[103] K. Kim, W. M. Park, Y. H. Kim, and S. Lee, "Stress analysis in a pedicle screw fixation system with flexible rods in the lumbar spine," *Proceedings of*

*the Institution of Mechanical Engineers, Part H: Journal of Engineering in Medicine*, vol. 224, no. 3, pp. 477–485, 2010.

[104] P. Shang, B. Ma, G. Hou, Y. Zhang, L. Cui, W. Song, and Y. Liu, "A novel artificial vertebral implant with gyroid porous structures for reducing the subsidence and mechanical failure rate after vertebral body replacement," *Journal of Orthopaedic Surgery and Research*, vol. 18, no. 1, p. 828, 2023.

[105] X. Xue, M. K. Patel, M. Kersaudy-Kerhoas, M. P. Desmulliez, C. Bailey, and D. Topham, "Analysis of fluid separation in microfluidic t-channels," *Applied Mathematical Modelling*, vol. 36, no. 2, pp. 743–755, 2012.

[106] S. Wang, L. Lee, and J. Lee, "A linear relation between the compressibility and density of blood," *The Journal of the Acoustical Society of America*, vol. 109, no. 1, pp. 390–396, 2001.

[107] E. K. Shang, D. P. Nathan, R. M. Fairman, J. E. Bavaria, R. C. Gorman, J. H. Gorman III, and B. M. Jackson, "Use of computational fluid dynamics studies in predicting aneurysmal degeneration of acute type b aortic dissections," *Journal of vascular surgery*, vol. 62, no. 2, pp. 279–284, 2015.

[108] S. Gómez, M. D. Vlad, J. López, and E. Fernández, "Design and properties of 3d scaffolds for bone tissue engineering," *Acta biomaterialia*, vol. 42, pp. 341–350, 2016.

[109] B. M. Johnston, P. R. Johnston, S. Corney, and D. Kilpatrick, "Non-newtonian blood flow in human right coronary arteries: steady state simulations," *Journal of biomechanics*, vol. 37, no. 5, pp. 709–720, 2004.

[110] M. A. Hussain, S. Kar, and R. R. Puniyani, "Relationship between power law coefficients and major blood constituents affecting the whole blood viscosity," *Journal of Biosciences*, vol. 24, no. 3, pp. 329–337, 1999.

[111] S. S. Shibeshi and W. E. Collins, "The rheology of blood flow in a branched arterial system," *Applied rheology*, vol. 15, no. 6, pp. 398–405, 2005.

[112] A. F. Morais, H. Seybold, H. J. Herrmann, and J. S. Andrade Jr, "Non-newtonian fluid flow through three-dimensional disordered porous media," *Physical review letters*, vol. 103, no. 19, p. 194502, 2009.

[113] D. Egger, M. Fischer, A. Clementi, V. Ribitsch, J. Hansmann, and C. Kasper, "Development and characterization of a parallelizable perfusion bioreactor for 3d cell culture," *Bioengineering*, vol. 4, no. 2, p. 51, 2017.

[114] L. Echeverri, M. Herrero, J. Lopez, and G. Oleaga, "Early stages of bone fracture healing: formation of a fibrin–collagen scaffold in the fracture hematoma," *Bulletin of mathematical biology*, vol. 77, no. 1, pp. 156–183, 2015.

[115] A. Schindeler, M. M. McDonald, P. Bokko, and D. G. Little, "Bone remodeling during fracture repair: The cellular picture," in *Seminars in cell & developmental biology*, vol. 19, pp. 459–466, Elsevier, 2008.

[116] R. Marsell and T. A. Einhorn, "The biology of fracture healing," *Injury*, vol. 42, no. 6, pp. 551–555, 2011.

[117] J. Vimmr, A. Jonášová, and O. Bublík, "Numerical analysis of non-newtonian blood flow and wall shear stress in realistic single, double and triple aorto-coronary bypasses," *International journal for numerical methods in biomedical engineering*, vol. 29, no. 10, pp. 1057–1081, 2013.

[118] M. Nouri, F. Jalali, G. Karimi, and K. Zarrabi, "Image-based computational simulation of sub-endothelial ldl accumulation in a human right coronary artery," *Computers in biology and medicine*, vol. 62, pp. 206–221, 2015.

[119] D. Mandal, N. Manna, and S. Chakrabarti, "Numerical study of blood flow through different double bell-shaped stenosed coronary artery during the progression of the disease, atherosclerosis," *International Journal of Numerical Methods for Heat & Fluid Flow*, vol. 20, no. 6, pp. 670–698, 2010.

[120] M. G. Bixel, A. P. Kusumbe, S. K. Ramasamy, K. K. Sivaraj, S. Butz, D. Vestweber, and R. H. Adams, "Flow dynamics and hspc homing in bone marrow microvessels," *Cell reports*, vol. 18, no. 7, pp. 1804–1816, 2017.

[121] D. Ali and S. Sen, "Permeability and fluid flow-induced wall shear stress of bone tissue scaffolds: Computational fluid dynamic analysis using newtonian and non-newtonian blood flow models," *Computers in biology and medicine*, vol. 99, pp. 201–208, 2018.

[122] C. Yan, L. Hao, A. Hussein, and P. Young, "Ti–6al–4v triply periodic minimal surface structures for bone implants fabricated via selective laser melting," *Journal of the mechanical behavior of biomedical materials*, vol. 51, pp. 61–73, 2015.

[123] D. Ali and S. Sen, "Permeability and fluid flow-induced wall shear stress of bone tissue scaffolds: Computational fluid dynamic analysis using newtonian and non-newtonian blood flow models," *Computers in biology and medicine*, vol. 99, pp. 201–208, 2018.

[124] M. N. Shahid, M. U. Shahid, S. Rasheed, M. Irfan, and M. A. Obeidi, "Computational investigation of the fluidic properties of triply periodic minimal surface (tpms) structures in tissue engineering," *Designs*, vol. 8, no. 4, p. 69, 2024.

[125] M. N. Shahid, M. M. Khan, M. U. Shahid, and S. Rasheed, "Fluidic properties of diamond and splitp structures with varying porosity levels in tissue engineering applications: A computational fluid dynamics analysis," *Engineering Proceedings*, vol. 75, no. 1, p. 39, 2024.

[126] N. Kohli, J. C. Stoddart, and R. J. van Arkel, "The limit of tolerable micromotion for implant osseointegration: a systematic review," *Scientific Reports*, vol. 11, no. 1, p. 10797, 2021.

[127] N. B. Abdullah, D. Miyazaki, E. Yamamoto, K. Ueki, and M. Nakai, "Effect of low modulus titanium plate fixation on rabbit femur bone healing," *Journal of Materials Research*, vol. 37, no. 16, pp. 2536–2545, 2022.

[128] Y. Mori, M. Kamimura, K. Ito, M. Koguchi, H. Tanaka, H. Kurishima, T. Koyama, N. Mori, N. Masahashi, and T. Aizawa, "A review of the impacts

of implant stiffness on fracture healing," *Applied Sciences*, vol. 14, no. 6, p. 2259, 2024.

[129] R. Verma, J. Kumar, N. K. Singh, S. K. Rai, K. K. Saxena, and J. Xu, "Design and analysis of biomedical scaffolds using tpms-based porous structures inspired from additive manufacturing," *Coatings*, vol. 12, no. 6, p. 839, 2022.

[130] S. Van Bael, Y. C. Chai, S. Truscello, M. Moesen, G. Kerckhofs, H. Van Oosterwyck, J.-P. Kruth, and J. Schrooten, "The effect of pore geometry on the in vitro biological behavior of human periosteum-derived cells seeded on selective laser-melted ti6al4v bone scaffolds," *Acta biomaterialia*, vol. 8, no. 7, pp. 2824–2834, 2012.

[131] S. Truscello, G. Kerckhofs, S. Van Bael, G. Pyka, J. Schrooten, and H. Van Oosterwyck, "Prediction of permeability of regular scaffolds for skeletal tissue engineering: a combined computational and experimental study," *Acta biomaterialia*, vol. 8, no. 4, pp. 1648–1658, 2012.

[132] A. A. Zadpoor, "Bone tissue regeneration: the role of scaffold geometry," *Biomaterials science*, vol. 3, no. 2, pp. 231–245, 2015.

[133] A. M. Omar, M. H. Hassan, E. Daskalakis, G. Ates, C. J. Bright, Z. Xu, E. J. Powell, W. Mirihanage, and P. J. Bartolo, "Geometry-based computational fluid dynamic model for predicting the biological behavior of bone tissue engineering scaffolds," *Journal of Functional Biomaterials*, vol. 13, no. 3, p. 104, 2022.

[134] A. T. Prakoso, H. Basri, D. Adanta, I. Yani, M. I. Ammarullah, I. Akbar, F. A. Ghazali, A. Syahrom, and T. Kamarul, "The effect of tortuosity on permeability of porous scaffold," *Biomedicines*, vol. 11, no. 2, p. 427, 2023.

[135] Y. Zhang, S.-y. He, P. Wang, J. Gu, Q. Jiang, M. Liu, and C. Wen, "Impacts of permeability and effective diffusivity of porous scaffolds on bone ingrowth: In silico and in vivo analyses," *Biomaterials Advances*, vol. 161, p. 213901, 2024.

[136] J. Fan, X. Jia, Y. Huang, B. M. Fu, and Y. Fan, "Greater scaffold permeability promotes growth of osteoblastic cells in a perfused bioreactor," *Journal of tissue engineering and regenerative medicine*, vol. 9, no. 12, pp. E210–E218, 2015.